

# REPORT DOCUMENTATION PAGE

Form Approved  
OMB No. 0704-0188

Time required for the collection of information is estimated to average 1 hour per response, including the time for reviewing instructions, searching existing data sources, gathering and maintaining the data needed, and completing and reviewing the collection of information. Send comments regarding this burden estimate or any other aspect of this collection of information, including suggestions for reducing this burden, to Washington Headquarters Services, Directorate for Information Operations and Analysis, 1215 Jefferson Davis Highway, Suite 1204, Arlington, VA 22202-4302, and to the Office of Management and Budget, Paperwork Reduction Project (0704-0188), Washington, DC 20503.

1. AGENCY USE ONLY (Leave blank)	2. REPORT DATE	3. REPORT TYPE AND DATES COVERED	
	3/15/96	Final Report: 3/1/93 - 3/1/96	
4. TITLE AND SUBTITLE Investigation of the Physics of Screech in Supersonic Jets and Turbulent Boundary Layers at High Reynolds Number and Control of Separation Through Oscillatory Blowing			5. FUNDING NUMBERS
			AFOSR F49620-93-1-0154
6. AUTHOR(S)			
Hassan Nagib		Ahmed Naguib Israel Wygnanski	
Candace Wark		Michael Hites	
7. PERFORMING ORGANIZATION NAME(S) AND ADDRESS(ES)			8. PERFORMING ORGANIZATION REPORT NUMBER
Fluid Dynamics Research Center Illinois Institute of Technology 10 W. 32nd Street Chicago, IL 60616			AFOSR-TR-96 0272
9. SPONSORING/MONITORING AGENCY NAME(S) AND ADDRESS(ES)			
AFOSR/NA 110 Duncan Ave. Suite B115 Bolling AFB, DC 20332-0001			
11. SUPPLEMENTARY NOTES			
12a. DISTRIBUTION/AVAILABILITY STATEMENT			
Approved for public release			
13. ABSTRACT (Maximum 200 words)			
<p>Using a flapped NACA 0015 airfoil, measurements of static pressure and lift, with and without oscillatory forcing from the leading edge and flap, demonstrated effective separation control and lift enhancement over the range <math>0.1 &lt; M &lt; 0.4</math>. Measurements showed that the lift increment was sensitive to the dimensionless forcing frequency. Additionally, a suction pressure coefficient of nearly -5.0 was produced on a previously stalled airfoil at <math>M=0.4</math>, indicating a region of supercritical flow on the airfoil, and suggesting that oscillatory blowing is a viable separation-control technique under compressible flow conditions.</p> <p>Using both the NDF test-section floor boundary layer and a suspended axisymmetric body, a range of momentum thickness Reynolds numbers of <math>7000 &lt; Re &lt; 50000</math> was investigated with a hot-wire anemometer. Streamwise mean and rms velocity and spectra in these boundary layers showed good agreement with established scaling observations. An increasing separation of scales and the appearance of a second low-frequency spectral peak were observed indicating a clear discrimination between inner and outer scales at high Reynolds number. Although some dependence on both axial and momentum thickness Reynolds number was observed, there appeared to be a <i>linear relationship</i> between friction velocity and free-stream velocity over this wide range of Reynolds numbers.</p>			
14. SUBJECT TERMS			15. NUMBER OF PAGES
High Lift Airfoil Control Supersonic Jet Screech High Reynolds Number Turbulent Boundary Layer			12
16. PRICE CODE			
17. SECURITY CLASSIFICATION OF REPORT		18. SECURITY CLASSIFICATION OF THIS PAGE	19. SECURITY CLASSIFICATION OF ABSTRACT
Unclassified		Unclassified	Unclassified
20. LIMITATION OF ABSTRACT			
UL			

## SUMMARY

### HIGH REYNOLDS NUMBER TURBULENT BOUNDARY LAYER MEASUREMENTS IN THE NDF

As an alternative to solving the Navier-Stokes equations via analytical or numerical techniques, nearly all experimental turbulent boundary layer research is based on the "scaling" of the quantities measured in the boundary layer, in particular the self-preserving, canonical, zero-pressure-gradient boundary layer. One drawback to this fundamental approach in the study of wall-bounded turbulent flows is the need to investigate the scaling of turbulent quantities over a "wide" Reynolds-number range in order to state whether an observation is Reynolds-number independent (or dependent).

When studying this scaling issue, a question which often arises is which of the two competing scales in the boundary layer, that is, inner and outer scales, renders a given turbulent quantity independent of Reynolds number variations? Successful scaling of a turbulent quantity with either inner variables (often referred to as wall variables) or outer variables (integral scales) implies that the dynamics of the turbulent motion giving rise to the turbulent quantity is controlled by the wall layer or the outer region of the boundary layer, respectively.

Boundary layer measurements thus far have not indicated that the turbulent boundary layer is truly self-preserving. This has resulted in speculation about the validity of well-accepted scaling laws such as the "log-law" velocity profile in the near wall region. Both George and Gad-el-Hak have pointed out some of the inconsistent features of Millikan's well accepted scaling laws. In particular, it has been observed experimentally that the shape factor  $H = \delta^* / \theta$  does not appear to approach a value of one for large Reynolds number, nor do the ratios of  $\delta^* / \delta$ ,  $\theta / \delta$ , and  $u_\tau / U_\infty$  approach zero in the limit of high Reynolds number. All of these were predicted by Millikan's theory, but in practice, none have been observed.

A complete understanding of the scaling of turbulent quantities and the interaction between scales has not yet been achieved. However, by utilizing the long test section and high free-stream velocity available in the National Diagnostic Facility, a Reynolds number range of

$7000 < Re_\theta < 50000$  was examined in order to help resolve some of the persistent questions regarding boundary layer scaling.

Flow quality in the NDF was evaluated and showed that the mean free-stream velocity uniformity was within 0.2% over the core of the flow, the temperature uniformity was within 1.0%, and turbulence intensity was about 0.05% and as low as 0.03% if a 1 Hz filter was applied to the signal before data acquisition. Additionally, the boundary layer on the test-section floor of the NDF displayed excellent two dimensionality and good agreement with well established boundary layer measurements when the adjustable ceiling was set for zero pressure gradient.

The preliminary boundary layer measurements on the NDF floor revealed several important trends. As previously expected, an important role may be played both  $Re_\theta$  and  $Re_x$  in characterizing the state of a wall layer. These high Reynolds number boundary layers revealed a lengthening of the overlap region of scales which suggests that the lack of these scales in low Reynolds number simulations may limit the validity of the low Reynolds number results regarding the significant dynamics of the turbulent boundary layer. An interesting bimodal distribution of energy, reflecting the separation of inner and outer scales, was revealed clearly for the first time in boundary layers by the higher Reynolds number spectra.

Measurements on an axially suspended cylinder in the NDF also confirmed that the overlap region of scales increased substantially with increasing Reynolds number, again suggesting an increased importance of inner- and outer-scale interactions. Also, the bimodal energy distribution was present in the spectra of the cylinder data as low as  $y^+ = 50$ . This, too, demonstrated the importance of inner- and outer-scale interactions since a second, low-frequency peak might not have been expected at a location so close to the wall at the edge of the buffer layer. The cylinder measurements did not, however, show the same dependence on  $Re_x$  as the floor data.

Remarkably, the friction velocity calculated from the cylinder data, Naguib's 1992 data, and some of NDF floor data appear to fall on the same line when plotted against free-stream velocity. This demonstrates a linear relationship between friction velocity,  $u_r$ , and  $U_\infty$  that has not been reported previously over such a wide range of Reynolds numbers. The only data that do not

coincide with this linear relationship are those from the furthest downstream locations on the NDF floor; however, these data follow a second, nearly parallel line. These linear relations suggest that there may be a stronger correlation between inner and outer scales than previous thought.

The ratio  $u_\tau/U_\infty$  was examined for the NDF floor and cylinder boundary layer with respect to Reynolds number,  $Re_\theta$ . Considerable scatter can be seen in the NDF floor data, and it was not clear whether the wall skin friction was continuously decreasing or approaching an asymptotic constant. In contrast, the cylinder data demonstrated a more clearly defined linear trend. It is difficult to speculate which data represent the actual decay, but the result has strong implications in George's theory since he predicts that  $u_\tau/U_\infty$  approaches an asymptotic constant while convention is still that  $u_\tau/U_\infty$  approaches zero.

## SUMMARY

### SEPARATION CONTROL EXPERIMENTS IN THE NDF

Previous experiments with a NACA 0015 airfoil at Tel-Aviv University had shown a remarkable ability to delay separation and enhance lift using oscillatory blowing through slots at the leading edge and the flap shoulder in free-stream Mach numbers up to about 0.2. However, for the oscillatory blowing technique to be truly beneficial, its effectiveness must be proven for velocities closer to actual flight conditions. Concerns that the technique would lose its ability to successfully control separation at higher Mach numbers have recently surfaced, and this skepticism is being driven by the drastic differences in the mechanism of airfoil separation between subsonic and supersonic flow. To address this issue, the airfoil from Tel-Aviv University was adapted to the NDF so that the low Mach number experiments could be verified and extended into the compressible flow regime.

One of the primary changes in airfoil separation that occurs at the onset of compressibility ( $M \approx 0.3$ ) is in regard to the mechanism of stall. For lower, incompressible Mach numbers, the stall behavior is initiated by trailing-edge stall where the stalled region progresses upstream until the separated region covers almost the entire chord of the airfoil. In contrast for higher compressible Mach numbers ( $M > 0.3$ ), leading-edge stall appears to be the precursor to complete stall. The latter, leading-edge stall, occurs abruptly as the airfoil is pitched passed a critical angle of attack, while the former, trailing edge stall, evolves gradually as the angle of attack is increased.

The existing 1.52 m x 1.22 m cross-section test section of the NDF was modified to accommodate the NACA 0015 airfoil previously used at Tel-Aviv University for separation control experiments. These modifications were necessary to reduce the height of the wind tunnel test section to 0.61 m in order to accommodate the airfoil and increase the maximum free-stream velocity of the wind tunnel to  $M=0.45$ . This smaller test section is one-half the original cross section and is one-twelfth the length of the original test section.

Measurement of the pressure distribution around the airfoil clearly showed the effects of oscillatory blowing on a stalled airfoil. By examining the pressure coefficient,  $C_p$ , of an initially stalled airfoil, it was seen that the application of oscillatory blowing from the leading edge resulted

in the re-establishment of the high suction peak, good pressure recovery along the airfoil, and a trailing edge pressure that more closely matched the Kutta condition. The end result of these changes in the pressure distributions was that the lift coefficient was increased as much as 80% over the stalled airfoil lift coefficient.

At the highest Mach number,  $M=0.41$ , the pressure data indicated a partial re-attachment of the flow due to the oscillatory blowing and a 50% increase in lift over the baseline stalled airfoil. Additionally, the  $-C_{p_{max}}$  of nearly 5.0 after the application of forcing indicated that the flow was supercritical over part of the airfoil, whereas it was not before the application of oscillatory blowing. This demonstrates that the oscillatory blowing technique has the potential to control separation even under supersonic flow conditions.

Experiments were performed to separate the compressibility effects from the  $C_\mu$  effects. The first experiment measured the lift increment,  $\Delta C/C$ , as a function of both Mach number and the corresponding dimensionless forcing frequency,  $F^+$ . This indicated that there was sensitivity to the forcing frequency at the higher Mach numbers, which was similar in both magnitude and  $F^+$  to results previously published by Seifert and Wygnanski for the lower Mach numbers.

The effect of hysteresis was investigated and showed that the improvement in lift was independent of the manner in which the forcing was applied.

These measurements have given a possible explanation for earlier conclusions and concerns about the apparent lack of effectiveness of separation-control schemes in the compressible regime ( $M>0.3$ ). It is encouraging that lift enhancement was observed over the entire range  $0.1 < M < 0.4$ , even with the small amount of unsteady blowing applied in these experiments. Additionally, the observation that supercritical flow was achieved due to the application of the oscillatory blowing shows that the technique can be extended successfully to even higher Mach numbers. The fact that hysteresis does not appear to influence the effectiveness of oscillatory forcing shows promise that the technique can be used to maneuver high-speed aircraft.

## TABLE OF CONTENTS

### CHAPTER I

#### HIGH REYNOLDS NUMBER TURBULENT BOUNDARY LAYER MEASUREMENTS IN THE NDF

1.1 Introduction.....	1
1.2 Background .....	1
1.3 Scaling in the So-Called Logarithmic Region .....	4
1.4 Objectives of Boundary Layer Experiments .....	6
1.5 The National Diagnostic Facility .....	7
1.6 NDF Flow Quality.....	9
1.7 NDF Floor Turbulent Boundary Layer Experimental Apparatus.....	11
1.8 Results from the NDF Floor Turbulent Boundary Layer .....	12
1.9 Results from the NASA Cylinder Turbulent Boundary Layer.....	16
1.10 Conclusions and Recommendations.....	18
1.11 References .....	21

### CHAPTER II

#### SEPARATION CONTROL EXPERIMENTS IN THE NDF

2.1 Introduction.....	23
2.2 Background .....	23
2.3 Objectives of NDF/TAU Airfoil Experiments .....	26
2.4 Modifications to the NDF Test Section .....	26
2.5 NDF Performance with Airfoil in Test Section.....	27
2.6 Experimental Apparatus.....	27
2.7 Results of NDF/TAU Airfoil Experiments.....	29
2.8 Conclusions and Recommendations.....	33
2.9 References.....	35

## SECTION I

### HIGH REYNOLDS NUMBER TURBULENT BOUNDARY LAYER MEASUREMENTS IN THE NDF

#### 1.1 Introduction

As an alternative to solving the Navier-Stokes equations via analytical or numerical techniques, nearly all experimental turbulent boundary layer research is based on the "scaling" of the quantities measured in the boundary layer, in particular the self-preserving, canonical, zero-pressure-gradient boundary layer. One drawback to this fundamental approach in the study of wall-bounded turbulent flows is the need to investigate the scaling of turbulent quantities over a "wide" Reynolds-number range in order to state whether an observation is truly Reynolds-number independent (or dependent).

When studying this scaling issue, a question which often arises is which of the two competing scales in the boundary layer, that is, inner and outer scales, renders a given turbulent quantity independent of Reynolds number variations? Successful scaling of a turbulent quantity with either inner variables (often referred to as wall variables) or outer variables (integral scales) implies that the dynamics of the turbulent motion giving rise to the turbulent quantity is controlled by the wall layer or the outer region of the boundary layer respectively.

A complete understanding of the scaling of turbulent quantities and the interaction between scales has not yet been achieved. However, by utilizing the long test section and high free-stream velocity available in the National Diagnostic Facility, a Reynolds number range of  $7000 < Re_0 < 50000$  was examined in order to help resolve some of the persistent questions regarding boundary layer scaling.

#### 1.2 Background

The coexistence of large and small scales and their interaction throughout the boundary layer leads into the discussion of structures: coherent, identifiable regions of

fluid within the boundary layer that influence the transport properties of the boundary layer. The study of turbulent structures has been facilitated by a combination of techniques, particularly space-time correlation measurements (Favre, 1957), flow visualization (Corino and Brodkey, 1967), and direct numerical simulation of low Reynolds number flow (Spalart, 1988).

Low speed streaks are one of the most predominant features of the viscous region of the boundary layer and can be seen easily in experiments as the accumulation of a fluid marker in the flow, for example hydrogen bubbles in a flow of water. The streaks are reported to be about 1000 viscous units long and are believed to be the precursor to the “bursting” event which consists of the formation of a streak, subsequent lift-up from the viscous layer, oscillation, and finally breakup. It is the bursting event that is believed to be one of the methods of interaction between the inner and an outer layer and one of the major producers of turbulent energy. Although there has been a good deal of data compiled about the streaky structures, the role of the streaks on the dynamics of the turbulent boundary layer is still unclear.

The explanation for the formation of streaks has ranged from simple variation of fluid velocity in the viscous layer causing vortex stretching, to hairpin vortices dragging their tails through the viscous layer, to big eddies with different velocity convecting through the outer region creating instabilities in the viscous layer, to a feedback effect of oscillations in the mean flow. These explanations predict that practically any region of the boundary layer can produce something that influences the formation of streaks. This large variation in ideas seems to be characteristic turbulence research and creates uncertainty about classifying turbulent motions as either inner- or outer-layer events.

The outer layer is also a source of controversy. The premise of the outer layer is that there exist large scales of the order of the boundary layer thickness that influence the dynamics of the area farthest from the wall as well as the log region and perhaps the viscous region. It has been hypothesized that the largest eddies are passive in nature and

do not contribute to the production of Reynolds stress. According to this explanation, it is the turbulence originating in the wall region that produces the Reynolds stress, and it is the bursting process that eventually leads to the formation of the large scale structures.

Some researchers, such as Sreenivasan (1989), postulate that the effect of the wall is transmitted only by the friction velocity to the outer region. This means that the velocity (or velocity deficit) in the outer region is dependent on both inner and outer variables, namely,

$$(U_\infty - U(y))/u_\tau = f(y/\delta, u_\tau/U_\infty) \quad (1.1)$$

Sreenivasan states that experiments have shown that the dependence on the velocity ratio,  $u_\tau/U_\infty$ , is very weak and reduces the defect law to a function of outer variables

$$(U_\infty - U(y))/u_\tau = f_o(y/\delta), \quad (1.2)$$

a relationship now questioned by George et al. (1994) and others.

Additionally, the question of the local scale interaction versus large scale momentum transfer is further complicated when viewed with the results of flow visualization studies. It has been observed that turbulent “bursts” from the buffer layer travel into the log-layer, and in some low Reynolds number experiments, all the way into the outer layer. These observations, along with the lack of comprehensive data at higher Reynolds numbers, leads to questions about how to explain the dynamics of the turbulent boundary layer.

The reasons for the formation, the degree of interaction between the previously mentioned structures, and the relative importance of each of the structures is still a mystery. Most arguments used to explain the bursts eventually end up reverting to a chicken-versus-egg scenario. In other words, if the bursting process caused the large scales, then what causes the bursts? Furthermore, if the bursts control the outer structure, then should the outer structure be considered dynamically inactive? If we assume that the hairpin or double roller is the dominant feature of the outer region, then how are they formed since they

extend throughout the boundary layer? This confusion suggests that it must be the interaction of inner and outer layers that drives and sustains turbulence.

### 1.3 Scaling in the So-Called Logarithmic Region

Two concepts that are used in analysis of turbulent flows are self-preserving (local invariance) and similarity solutions. The latter is based on simplifying the N-S equations under the assumption of  $Re \rightarrow \infty$  so that a similarity solution based on one length scale and one velocity scale can be found. The former is usually thought of in an experimental sense as a flow that has both a similarity solution and is Reynolds number independent. In a self preserving flow, the turbulence is assumed to be controlled by instantaneous local environment and is thus not influenced by large scale motion such as the expansion of a wake or growth of the boundary layer.

In order for a boundary layer to be self preserving, in particular the canonical zero pressure gradient boundary layer, the dimensionless statistical quantities measured within the boundary layer must be independent of streamwise location in the boundary layer. The choice of the reference scale used for the nondimesionalization is based on the regions of the boundary layer itself. Very near the wall the appropriate velocity and length scales are the friction velocity,  $u_\tau$ , and the viscous length scale,  $\nu/u_\tau$ . While very far from the wall, the appropriate scales are the free-stream velocity,  $U_\infty$ , and an integral length scale, usually the boundary layer thickness,  $\delta$ , or the momentum thickness,  $\theta$ . Experiments have shown that if the boundary layer statistics are non-dimensionalized by these scales in their applicable regions, the near-wall statistics apparently are Reynolds number independent near the wall, and likewise, the outer-region statistics are Reynolds number independent far from the wall. It is for this reason that it is common practice to present turbulence statistical quantities by plotting the variables in each of these regions so that the statistics appear independent of Reynolds number when using inner variables near the wall and outer variables far from the wall. Unfortunately, the similarity solution of the boundary layer

equations in the inner and outer regions ignore the fact that the Reynolds number can vary substantially for many different experiments.

Boundary layer measurements thus far have not indicated that the turbulent boundary layer is truly self-preserving. This has resulted in speculation about the validity of well-accepted scaling laws such as the “log-law” velocity profile in the near wall region. Apparently, the chain of researchers questioning the log-law has proceeded from Barenblatt (1979) to Long and Chen (1981) to Sreenivasan (1989) to Gad-el-Hak and Bandyopadhyay (1994) and George et al. (1994). Both George and Gad-el-Hak have pointed out some of the inconsistent features of Millikan’s (1939) well accepted scaling laws. In particular, it has been observed experimentally that the shape factor  $H = \delta^* / \theta$  does not appear to approach a value of one for large Reynolds number, nor do the ratios of  $\delta^* / \delta$ ,  $\theta / \delta$ , and  $u_\tau / U_\infty$  approach zero in the limit of high Reynolds number. All of these were predicted by Millikan’s theory, but in practice, none have been observed. Additionally, since the skin friction coefficient can be computed by

$$C_f \equiv \frac{\tau_w}{\frac{1}{2} \rho U_\infty^2} = 2 \frac{u_\tau^2}{U_\infty^2} \quad (1.3)$$

then Millikan’s argument that  $u_\tau / U_\infty \rightarrow 0$  as  $Re \rightarrow \infty$  would mean that the skin friction would approach zero even if the Reynolds number were made large simply by moving further downstream. As George points out, this does not appear to make physical sense. A better approach to scaling the boundary layer statistics may be one in which the Reynolds number dependence is not ignored, particularly in the overlap region.

George et al. have attempted to explain this inconsistency in the use of inner- and outer-variable scaling for the turbulent boundary layer. They present an alternative by introducing a similarity solution that includes a Reynolds number parameter based on both inner and outer scales:  $\varepsilon = (u_\tau \delta / \nu)^{-1}$ . This leads to inner and outer solutions to boundary layer equations which demonstrate Reynolds number dependence in the form:

$$\frac{U}{u_\tau} = f\left(\frac{yu_\tau}{\nu}, \varepsilon\right) \quad (1.4)$$

$$\frac{U - U_\infty}{U_\infty} = F\left(\frac{y}{\delta}, \varepsilon\right) \quad (1.5)$$

which become the conventional scaling laws in the limit of  $\varepsilon \rightarrow \infty$ . As a consequence of this new theory, the proper scaling for the overlap region where the two solutions must match becomes

$$\frac{U}{u_\tau} = C_i \left( \frac{yu_\tau}{\nu} \right)^\gamma \quad (1.6)$$

$$\frac{U}{U_\infty} = C_o \left( \frac{y}{\delta} \right)^\gamma \quad (1.7)$$

where the parameters  $C_i$ ,  $C_o$ , and  $\gamma$  are all Reynolds number dependent and can be determined analytically. Furthermore, these scaling rules in the overlap regions provide a Reynolds number dependent relation between the velocity scales (friction law) as

$$\frac{u_\tau}{U_\infty} = \frac{C_o}{C_i} \varepsilon^{-\gamma}. \quad (1.8)$$

George has also proposed that the benefits of using the boundary layer thickness,  $\delta$ , the momentum thickness,  $\theta$ , or the displacement thickness,  $\delta^*$ , are all equal since his theory predicts that each of these quantities are directly related to each other and that relation becomes a constant factor in the asymptotic limit of high Reynolds number. It is therefore not critical which of these is chosen for outer scaling of statistics, since many past experiments have shown similar results for any and all of these outer scales.

#### 1.4 Objectives of Boundary Layer Experiments

Using both the NDF floor boundary layer and the 30 foot, 18 inch diameter NASA cylinder model suspended axially within the test section of the National Diagnostic Facility (NDF), a wide Reynolds number range of  $7000 < \text{Re}_0 < 50000$  was available to extend the

current wall-bounded turbulent boundary layer inner- and outer-scaling research. A preliminary investigation of the effects of variation of streamwise Reynolds number ( $Re_x$ ) and momentum-thickness Reynolds numbers ( $Re_\theta$ ) was possible in both of these boundary layers. This allowed for the measurement of streamwise mean and fluctuating velocity and streamwise power spectra to support/refute some of the current ideas in inner- and outer-scaling of mean, fluctuating, and spectral quantities in the turbulent boundary layer.

### 1.5 The National Diagnostic Facility

The National Diagnostic Facility (NDF) at the IIT Fluid Dynamics Research Center (FDRC) is a closed-return, low-disturbance subsonic wind tunnel designed to study high Reynolds number ( $Re$ ) flows. Figure 1.1 shows pictorially how the NDF fits into the current state of wind tunnel research. Because of the unique combination of the long test section and large free-stream velocity range, the NDF helps to fill a gap between typical subsonic university research tunnels and large-scale industrial and government laboratory development tunnels. Although none of these aforementioned facilities have the capabilities to completely simulate flight or other high-speed applications, the NDF provides an ideal, low-turbulence environment to extend the current base of *fundamental* turbulence research.

The drawing of the NDF in Figure 1.2 shows key features of the wind tunnel. Proceeding in the clockwise (downstream) direction around Figure 1.2, the primary components of this wind tunnel are now described. A 2000 hp, 1200 RPM constant-speed electric motor (4160 VAC) and a variable-speed electromagnetic clutch are connected by a propeller shaft to a 16-blade variable-pitch vane-axial fan. To maintain constant flow temperature, the turning vanes in turns one and three are hollow and partitioned into several chambers running the length of the vane. Chilled water is pumped from a 1100 ton-hr ice storage system through these vane chambers. In turn two, the high pressure side (inside) of each turning vane is lined with acoustically absorbent material to decrease the effect of fan noise on the test section and models. Just downstream of turn two in the settling

chamber are the turbulence manipulators: a 15.2 cm thick honeycomb section with 6.4 mm cells followed at a distance of 30.5 cm by six 8.66 cell/cm, low solidity ( $\sigma=0.30$ ) screens with a uniform spacing of 23 mm. The cross-section of the complete settling chamber is 305 cm x 381 cm. Finally, a 6.25:1, 5th-order polynomial contraction accelerates the flow into the test section.

The NDF has several features which make it particularly suitable for high  $Re$  fundamental research. The most significant of which is the large, low-disturbance test section (where "low-disturbance" refers to a condition of nearly uniform mean flow with low levels of velocity, temperature, and pressure fluctuations). The facility has a 1.22 m x 1.52 m test section, (10.4 m) long, capable of reaching a projected maximum free-stream velocity of 120 m/s. The test section module shown in Figure 1.3 is typical of four 2.57 m long modules with two hinged doors on the north side of each module and two hinged windows on the south side of each module. (See Figure 1.1 for north-south orientation). Although all of the doors and windows are interchangeable, this is the normal test section configuration so that experimental apparatus can be mounted to the aluminum doors on the inner section of the wind tunnel and the experiment can be viewed through the windows from the outer section.

A 17-panel motorized adjustable ceiling is used to adjust the streamwise pressure gradient in the test section. The first seven ceiling panels downstream of the contraction are 50.8 cm long while the last 10 panels are 63.5 cm, and all of the panels are joined together with 6.4 mm hinge pins. The top, downstream edge of each panel is connected to a pair of stepper-motor controlled ball jack screws which move each panel up and down. Each of the ball jack screw assemblies has a set of linear bearings that are attached to a rail on either side of the test section. This allows the assembly to move back and forth in the streamwise direction to accommodate the motion of the panels. The panels have a total travel of  $\pm 15$  cm and a fine step increment of just over 1  $\mu\text{m}$  per step for accurate positioning and a wide range of pressure gradients.

The low-rpm, variable speed fan with adjustable blade pitch achieves a wide range of operating velocities and can be adjusted precisely with exceptional repeatability in selecting the same velocity from experiment to experiment. Typically, the flow velocity can be adjusted to within 0.1 m/s of the desired value, and can be held to within  $\pm 0.1$  m/s over several hours of data acquisition.

The temperature of the flow is maintained by a chilled water system which provides cooling through heat exchangers inside the turning vanes in turns one and three. The free-stream cooling in turns one and three typically can maintain steady-state temperature to within 0.2 °F (0.1 °C) at all tested free-stream velocities, and can be held to within  $\pm 0.2$  °F ( $\pm 0.1$  °C) over several hours of data acquisition.

## 1.6 NDF Flow Quality

The following discussion is based on measurements by Nagib et al. (1994) and Nagib and Hites (1994) which quantified the mean velocity uniformity, temperature uniformity, turbulence intensity levels, and free-stream fluctuating pressure levels within the NDF test section.

Mean velocity contours were obtained at streamwise locations  $x=20$  cm and  $x=790$  cm in the test section and showed that the core of the test-section flow was within 0.2% of the mean velocity for all free-stream velocities tested. Two of the results from Nagib et. al. (1994) are replotted here in Figure 1.4 for a free-stream velocity of 20 m/s at 25 cm and 890 cm downstream from the contraction exit. These figures show the percentage deviation from the mean free-stream velocity,  $100x\Delta U/U_\infty$ , over the entire 1.22 m x 1.52 m test section and demonstrate the exceptional uniformity of the test-section flow. Comparison of the top and bottom plots Figure 1.4 shows the growth of the wall boundary layers with downstream position as evidenced by the dark area near the walls.

Temperature contours were measured at a downstream position of  $x=20$  cm and a free-stream velocity of 30 m/s. The temperature gradients were observed to be larger than

the velocity gradients, but apparently did not influence the mean velocity field. The temperature deviation across the test section was less than 1.0% of the temperature in the core of the flow and it appeared that the outer side of the test section was slightly warmer than the inner.

The streamwise velocity fluctuations in the test section were measured with a pair of single-component hot-wires located at the same streamwise position but separated by 61 cm to insure that the turbulence measured by each was uncorrelated. Figure 1.5 shows the disturbance levels as a function of free-stream velocity obtained at a location 79 cm downstream of the contraction exit. In Figure 1.5 (top) the rms fluctuations of the unfiltered velocity time series were separated into effects of the short-term mean velocity fluctuations and the true turbulence intensity using a two-point optimal filter. It can be seen that the total velocity "disturbance intensity" was less than 0.08% at all tested free-stream velocities, that is up to 50 m/s. Furthermore, the contribution due to the uncorrelated portion of the two time series, i.e. the turbulence, ranged from 0.03 to 0.05% and increased with increasing free-stream velocity. In comparison, it was previously found that the turbulence intensity was less than 1.5% downstream of the honeycomb and less than 0.3% downstream of the six screens.

It is important to note that the turbulence intensities reported for the NDF were obtained without any filtering of the hot-wire signal. This is in contrast to typical disturbance measurements often quoted in the literature without such claims. Figure 1.5 (bottom) demonstrates the effect of filtering the hot-wire signal when performing turbulence intensity measurements. In this figure, the free-stream velocity was held constant for four different fan speeds by changing the fan pitch for each fan speed. It demonstrates that the turbulence intensity remains relatively independent of the fan speed for a given free-stream velocity, but more importantly, the horizontal lines drawn at 0.028% and 0.032% turbulence intensity indicate the effect of filtering. These two values of the free-stream disturbance level were record by high-pass filtering the hot-wire signals

at 0.1 and 1.0 Hz, respectively. This demonstrates the dramatic change that can result from arbitrarily filtering the hot-wire signal and also that a significant fraction of the free-stream turbulence level results from very low frequency disturbances.

The power spectra of the turbulence at different free-stream velocities were calculated to determine the change in spectral energy distribution with varying free-stream velocity. The spectra revealed a broad-banded increase in turbulent energy for increasing free-stream velocity and demonstrated that most of the contributions to the turbulence intensity were from larger scales ( $f < 200\text{Hz}$ ).

Free-stream static pressure was measured at a single position in the test section of the NDF to document the pressure fluctuations generated by several types of disturbances, particularly those associated with acoustic noise generated by the fan. Power spectra of the fluctuating pressure time series demonstrated the existence of low frequency standing waves which ranged in sound pressure level from approximately 70 dB at 16 m/s to 90 dB at 55 m/s. The spectra also revealed the blade passing frequency of the fan and several of its harmonics. The amplitude of the fundamental blade passing frequency ranged from about 70 dB at 22 m/s to 94 dB at 55 m/s. Finally, the total sound pressure level varied from 91 dB at 16 m/s to 111 dB at 55 m/s and was generally less than 0.5% of the free-stream dynamic pressure, indicating a relatively quiet flow within the test section.

These results demonstrate that the turbulence manipulators, i.e. the honeycomb and screens, are effective in producing both an exceptionally uniform mean free-stream and dramatically low turbulence levels. Furthermore, all of these results are consistent with the initial design expectations of the NDF.

### **1.7 NDF Floor Turbulent Boundary Layer Experimental Apparatus**

The turbulent boundary layer on the floor of the NDF test section was examined to evaluate its effectiveness for high  $Re$  research. This surface was chosen because of its impressive length (10.4 m) and its similarity to the traditional flat plate. The floor of the

NDF was fabricated using twelve 86 cm x 152 cm composite aluminum panels with polished stainless steel skins. Each panel was individually leveled and bolted in place to produce a nearly seamless flat-plate surface. Preliminary observations of the floor boundary layer showed that the boundary layer was already about one inch thick at the exit of the contraction and was fully turbulent for free-stream velocities greater than about 20 m/s. It was also observed that typical boundary layer trips such as sandpaper or cylindrical rods had little effect on the boundary layer, and consequently the boundary layer was not tripped for any of the preliminary experiments.

A single-component hot-wire was used to measure the streamwise velocity component in the turbulent boundary layer which exists on the floor of the NDF test section. The hot-wire used was tungsten with diameter 0.0001" (2.5  $\mu\text{m}$ ) and a length to diameter ratio of 200. A Dantec Type 55M10 constant temperature anemometer was used in all measurements. The signal was filtered with an Ithaco 4302 variable cut-off 24 dB/octave analog filter and amplified using a variable-gain Stanford Research Systems SR560 low noise amplifier. All data were acquired using a National Instruments AT-MIO-16F-5 A/D board driven by Labview in a Gateway 2000 4DX2-66V PC. For determining velocity power spectra, 819200 point time-series were acquired with a dimensionless sampling interval of  $\Delta t^+=2$ . The velocity spectra were produced by ensemble averaging 400 FFT records of 2048 points/record on a Silicon Graphic Challenge CMN-A011 deskside server.

### 1.8 Results from the NDF Floor Turbulent Boundary Layer

The mean velocity profiles were measured for six different  $\text{Re}_\theta$ 's ranging from 9500 to 49000 to obtain the boundary layer parameters shown in Table 1.1. Table 1.1 also lists boundary layer data from Naguib (1992) for two lower  $\text{Re}_\theta$ 's taken in the Mark V. Morkovin wind tunnel. These are shown for the purpose of comparison to the NDF data.

It is important to note that the two data sets from Naguib (1992) and the two lowest Reynolds numbers for the present measurements are obtained using comparable development distances of the boundary layer and will be referenced as cases with  $x_1$  fetch. The other four cases have a fetch  $x_2$  nearly three times as large. While Naguib's (1992) measurements were obtained on a flat plate with a carefully designed leading edge suspended in the test section, the excellent two-dimensionality on the floor of the NDF, encouraged the comparison between the two sets of measurements.

Table 1.1. NDF Test-Section Floor Boundary Layer Parameters

$x$ (m)	$U_\infty$ (m/s)	$Re_\theta$	$u_\tau$ (m/s)	$\theta$ (cm)	$\delta$ (cm)	$l^+$
3.3*	10.7	4550	0.40	0.66	5.8	13
3.3*	15.7	6240	0.57	0.62	5.4	19
3.1 ( $x_1$ )	20.7	9590	0.73	0.70	5.9	24
3.1	30.3	13800	1.05	0.69	6.1	35
8.2 ( $x_2$ )	21.1	21300	0.68	1.52	12.6	22
8.2	31.6	29900	0.99	1.42	12.1	33
8.2	45.7	41800	1.40	1.37	12.1	46
8.2	57.8	48900	1.74	1.28	11.0	57

\*Data from Naguib (1992)

In the present measurements (see Table 1.1), we have yet to utilize special sensors to maintain the values of  $l^+$  lower than the critical value near 20. However, it is not expected that the somewhat longer sensor length will have an effect on the measurements reported here except for the high range of frequency in the velocity spectra. Therefore, it is not the intention to draw any conclusions regarding these ranges of scales.

The mean velocity profiles for all eight conditions summarized in Table 1.1 are displayed in Figures 1.6 using inner and outer scaling. In addition to the much wider logarithmic range at high Reynolds numbers, it is very significant to note the effect of changing the boundary-layer development fetch,  $x_1$  vs.  $x_2$ , on the wake component for

the inner scaling and on the additive constant to the outer-scaled mean velocity profile in the log layer.

Similar effects of the fetch or  $Re_x$  are reflected in the inner- and outer-scaled turbulence intensity profiles in Figure 1.7. The plateau value of 2.5 times the friction velocity, which can be expected from asymptotic estimates, is only achieved with the larger fetch. Many previous wind-tunnel measurements, including those at IIT, have displayed lower values of the plateau as shown here for the smaller development fetch and have been a source of some puzzlement. It is important to observe the much larger log layer for higher Reynolds numbers. By increasing the Reynolds number by approximately one order of magnitude, the log layer outer extension is increased from around 300 or 400 to over 2,000.

Figures 1.8, 1.9, 1.10 present the streamwise velocity spectra, for all eight Reynolds numbers at the same height based on inner variables scaling. While Figure 1.8 was obtained within the buffer layer, Figures 1.9 and 1.10 reflect the change as distance was increased from the wall within the log layer. In each of the figures, the same data are presented twice. The first presentation uses a logarithmic scale for the spectral function. The second graph presents the spectral function multiplied by the frequency using a linear scale.

Figures 1.11, 1.12 and 1.13 present a comparable array of spectra except at constant heights based on scaling with the momentum thickness. In these figures, the measurements were recorded at three different positions in each boundary layer. The smallest of these was less than one-tenth of the momentum thickness and the largest was equal to the height of the momentum thickness. At least two important results are revealed from these spectra. The first deals with the range of energy scales in the so-called overlap region. These are the turbulent fluctuations which scale both with inner and outer variables, based on dimensional arguments. These scales should have a minus one slope in the

logarithmic plot of the spectra of each of the figures and a zero slope in the linear plots (since the spectral function is multiplied by  $f$ ).

It is clear from the figures that this range of dynamically important scales is quite limited at the lower Reynolds numbers, but that it increases significantly, as in the case of the extent of the log layer, in the newly acquired high Reynolds number measurements. The other interesting result deals with a bimodal shape of some of the spectra shown in the linear plots. This is particularly evident at  $y^+ = 50$  in Figure 1.9, and at  $y/\theta = 0.078$  in Figure 1.11 as the Reynolds number is increased. We conjecture that these two peaks reflect the inner and outer scales of the boundary layer. Since the area under these curves represents the energy contained in the respective range of scales, it is significant to note the relative changes with Reynolds number.

These results and their analysis are only preliminary at this stage. However, we are very excited about the vast potential provided by the NDF to rapidly and effectively clarify many of the issues, regarding the dynamics and scaling of turbulent boundary layers, which had remained elusive for several decades. The preliminary conclusions based on the NDF floor boundary layer may be summarized as follows:

- The boundary layer on the test-section floor of the NDF displays excellent two dimensionality and good agreement with well established boundary layer measurements when the adjustable ceiling is set for zero pressure gradient.
- The range of  $Re_\theta$  provided by this boundary layer allows us to expand our capabilities significantly and has the potential of achieving values comparable to flight conditions.
- The preliminary measurements already reveal several important trends, among them are:
  - As previously suspected, an important role may be played by the length of a turbulent boundary layer development fetch; i.e., both  $Re_\theta$  and  $Re_x$  are important in characterizing the state of a wall layer.

- High Reynolds-number boundary layers reveal the importance of the overlap region of scales and suggest that the lack of these scales in low Reynolds number simulations may limit the validity of their results regarding the significant dynamics.
- An interesting bimodal distribution of energy, reflecting the separation of inner and outer scales, is revealed clearly for the first time in boundary layers by the higher Reynolds number spectra. This growth of the separation in scales is clearly evidenced in Figure 1.14 (top).

### 1.9 Results from the NASA Cylinder Turbulent Boundary Layer

The data obtained using the NDF floor provided some interesting results; however, the apparent dependence on  $Re_x$  was not satisfactorily explained. In the scaled mean and rms velocity profiles presented earlier in Figures 1.6 and 1.7, the dependence on  $Re_x$  seemed to change abruptly so that profiles at fetch  $x_1$  collapsed to one curve and at fetch  $x_2$  collapsed to another. To further examine this, Figure 1.14 (bottom) shows the friction velocity,  $u_\tau$ , as a function of free-stream velocity,  $U_\infty$ , for four difference downstream locations on the NDF floor. The same type of discontinuous behavior as the scaled mean and rms velocity of Figures 1.6 and 1.7 can be observed with the calculation of the friction velocity in Figure 1.14. This is somewhat surprising, since one might expect a continuous variation in the ratio  $u_\tau/U_\infty$  with the Reynolds number.

As a comparison to the NDF floor data and to help explain this unique  $Re_x$  dependency, an 18-inch diameter, 30-foot long cylinder was mounted axially within the NDF test section so that the NDF floor measurements could be repeated on a suspended surface. A drawing of the cylinder in the NDF test section is shown in Figure 1.15 and additional details of the design and installation of the model are available in Mazanec (1996). The mean velocity uniformity as measured with at Pitot probe at about 3 cm from

the cylinder surface and 7 m downstream is shown in Figure 1.16 and demonstrates a two-dimensional axisymmetric boundary layer. The data acquisition equipment used in the cylinder experiments is identical to that described in the previous sections for the NDF floor boundary layer.

In Table 1.2 are the boundary layer parameters for the cylinder experiments, and Figures 1.17 and 1.18 show the streamwise mean and rms velocity scaled on inner and outer variables over the range  $7450 < Re_\theta < 22500$  for two different streamwise locations. These figures compare well with, and in fact collapse better than, the NDF floor velocity data. Examination of the velocity spectra from the cylinder in Figure 1.19 also reveal the same distinct low frequency peak at  $y^+=50$  as the NDF floor data. Not only is the second peak clearly evident in both sets of spectra, but the all of the data suggest that the outer-region influence persists even down to the edge of the buffer layer at  $y^+=50$ . Figures 1.20 and 1.21 for  $y^+=100$  and  $y/\theta=1.13$  also compare well with their counterparts from the NDF floor.

Table 1.2. Cylinder Boundary Layer Parameters

x (m)	$U_\infty$ (m/s)	$Re_\theta$	$u_\tau$ (m/s)	$\theta$ (cm)	$\delta^*$ (cm)	$l^+$
3.7 ( $x_1$ )	19.8	8590	0.74	0.65	0.86	13
3.7	28.0	11400	1.02	0.61	0.80	19
5.8 ( $x_2$ )	12.1	7450	0.46	0.91	1.19	22
5.8	29.6	17400	1.04	0.87	1.13	33
5.8	37.6	22500	1.29	0.86	1.12	57

In contrast to the NDF floor boundary layer, the friction velocity data for the cylinder does not follow the same discontinuous behavior. Figure 1.22 (top) shows the same data for the NDF floor from Figure 1.14 along with similar data for the cylinder and also data from Naguib (1992). Remarkably, the data from the cylinder, Naguib, and the first two NDF floor locations appear to fall on the same line. The only data that do not coincide with the line are those from the furthest downstream locations on the NDF floor.

Figure 1.22 (bottom) presents another perspective of this by showing the dependence of the ratio  $u_\tau/U_\infty$  on Reynolds number,  $Re_\theta$ . Considerable scatter can be seen in NDF floor data, and it is not clear where the wall skin friction is continuously decreasing or approaching an asymptotic constant. In contrast, the cylinder data in Figure 1.22 (bottom) demonstrate a more clearly defined linear trend. It is difficult to speculate which data represent the actual decay, but the result has strong implications in George's theory since he predicts that  $u_\tau/U_\infty$  approaches an asymptotic constant while convention is still that  $u_\tau/U_\infty$  approaches zero.

### 1.10 Conclusions and Recommendations

Although both the NDF floor and the cylinder boundary layers have been shown to have good two-dimensionality and the mean and fluctuating quantities seem to follow conventional scale patterns, further analysis of the data is required to make any conclusions about the scaling of the high Reynolds number turbulent boundary layer. It is not clear whether the floor and the cylinder data are showing two distinct trends with regard to the friction velocity or if the floor data are so highly scattered that they appear to deviate from those of the cylinder.

The cylinder measurements also confirm many of the conclusions stated earlier in reference to the NDF floor data. Namely, the overlap region of scales increases substantially with increasing Reynolds number suggesting an increasing importance of inner- and outer-scale interactions. Also, the bimodal energy distribution is present in the spectra of both the NDF floor and cylinder data at  $y^+=50$ . This, too, demonstrates the importance of inner- and outer-scale interactions since a second, low-frequency peak might not have been expected at a location so close to the wall at the edge of the buffer layer.

In regard to these results and the anticipated measurements in the NDF, one difficulty in determining the precise inner-scaling of the boundary layer mean and rms quantities has been with the determination of the friction velocity,  $u_\tau$ . Up to this point (at

IIT),  $u_\tau$  has generally been evaluated based on the Clauser fit which *assumes* the existence of a logarithmic region in the wall layer where the mean velocity profile collapses with  $u_\tau$ . Alternatives to the Clauser fit include direct measurement of the wall skin friction using a shear stress balance or obtaining the velocity profile within a few viscous lengths from the wall and assuming that  $y^+ = u^+$ . The latter which would become cumbersome, if not impossible for the high  $Re_\theta$  experiments in the NDF since the viscous length scale approaches 7  $\mu\text{m}$  at high  $Re_\theta$ . To alleviate this ambiguity, future wall shear stress measurements will be made directly using both optical and capacitive flush-mounted shear stress sensors. These measurement techniques are being developed at IIT with the assistance of Micro-Electro-Mechanical Sensor (MEMS) groups at M.I.T. and Case Western who will be providing the sensors.

Another previously prohibitive detail of the high Reynolds number NDF experiments was the spatial resolution of the hot-wire probes. Gad-el-Hak (1994) suggests that the length of the probe be no longer than 5 viscous lengths; however, Wark and Naguib (1992) have found that a maximum of 20 viscous lengths provides adequate spatial resolution. The difficulty with these smaller length probes is that the diameter must be decreased proportionally to maintain an L/D of at least 200 to minimize the conductive heat loss to the probe supports. To give some representative numbers at  $Re_\theta \approx 40000$  in the NDF, the viscous length scale is predicted to be on the order of 7  $\mu\text{m}$  assuming a friction velocity is about 2.1 m/s. To satisfy the constraint of  $l^+ = 20$  viscous lengths for the probe, the maximum probe length is 140  $\mu\text{m}$  with a diameter of 0.7  $\mu\text{m}$ . Currently, single-component and shear-wire probes have been produced here that are 0.5  $\mu\text{m}$  in diameter and about 150  $\mu\text{m}$  long which satisfy these restrictions.

Implementation of these sensors as diagnostic tools over the wide range of Reynolds numbers proposed will provide invaluable experimental data. Furthermore, with the determination of the appropriate scaling of the double peak in the streamwise spectra

and a resolution of the  $Re_x/Re_\theta$  scaling issue, future analysis of new data will include digital filtering of the velocity, shear stress, and pressure in order to separate the effects of the inner- and outer-layer dynamics.

### 1.11 References

Barenblatt, G.I., Similarity, Self-Similarity, and Intermediate Hypothesis, Plenum Press, New York, 1979.

Corino, E.R. and Brodkey, R.S., "Avisual Investigation of the Wall Region in Turbulent Flows," J. Fluid Mech., Vol. 37, p.1, 1969.

Favre, A.J., Gaviglio, J.J, and Dumas, R., "Space-Time Double Correlations and Spectra in a Turbulent Boundary Layer," J. Fluid Mech., Vol. 2, p. 313, 1957.

Gad-el-hak, M. and Bandyopadhyay, P.R., "Reynolds Number Effects in Wall-Bounded Turbulent Flows," Appl. Mech. Rev., Vol. 47, No. 8, p. 307, 1994.

George, Castillo, and Knecht, "The Zero Pressure-Gradient Turbulent Boundary Layer", Manuscript draft in preparation, 1994.

Long, R.R. and Chen, T-C, "Experimental Evidence for the Existence of the 'Mesolayer' in Turbulent Systems," J. Fluid Mech., Vol. 105, p. 19, 1981.

Mazanec, M.J., "Design of Research Equipment for Use in the National Diagnostic Facility," M.S. Thesis, Illinois Institute of Technology, May 1996.

Millikan, C.B., "A Critical Discussion of Turbulent Flows in Channels and Circular Tubes," Proc. 5th Int. Cong. Appl. Mech., Wiley, New York, p. 386, 1939.

Nagib, H.M., and Hites, M.H., "High Reynolds Number Boundary-Layer Measurements in the NDF," AIAA 95-0786, 33rd Aerospace Sci. Mtg., Reno, NV, 1995.

Nagib, H., Hites, M., Won, J., and Gravante, S., "Flow Quality Documentation of the National Diagnostic Facility," AIAA 94-2499, 18th AIAA Aerospace Ground Testing Conference, 1994.

Naguib, A.M., "Inner- and Outer-Layer Effects on the Dynamics of a Turbulent Boundary Layer," Ph. D. Thesis, Illinois Institute of Technology, 1992.

Naguib, A.M., and Wark, C.E., "An Investigation of Wall-Layer Dynamics Using a Combined Temporal Filtering Correlation Technique", J. Fluid Mech., vol 243, p. 541, 1992.

Spalart, P.R., "Direct Simulation of a Turbulent Boundary Layer up to  $Re_\theta=1410$ ," J. Fluid Mech., Vol 187, p. 61, 1988.

Sreenivasan, K.R., "The Turbulent Boundary Layer," Lecture Notes in Engineering 46, Frontiers in Experimental Fluid Mechanics, Springer-Verlag, p. 159, 1989.

## CHAPTER II

### OSCILLATORY BLOWING EXPERIMENTS IN THE NDF

#### 2.1 Introduction

Previous experiments with a NACA 0015 airfoil at Tel-Aviv University (Seifert et al., 1994 and Wygnanski and Seifert, 1994) had shown a remarkable ability to delay separation and enhance lift using oscillatory blowing through the airfoil at the leading edge and the flap shoulder at free-stream Mach numbers up to about 0.2. However, for the oscillatory blowing technique to be truly beneficial, its effectiveness must be proven for velocities closer to actual flight conditions. Concerns that the technique would lose its ability to successfully control separation at high Mach numbers have recently surfaced. This skepticism is driven by the drastic differences in the mechanism of airfoil separation between subsonic and supersonic flow. To address this issue, the airfoil from Tel-Aviv University was adapted to the NDF so that the low Mach number experiments could be verified and extended into the compressible flow regime.

#### 2.2 Background

Previous measurements by Wygnanski and Seifert (1994) and Seifert et al. (1994) using pulsed blowing of air through spanwise slots along the leading edge, shoulder, and flap hinge of a NACA 0015 airfoil have demonstrated exceptional improvements in separation control. By applying oscillatory blowing with various amplitudes and frequencies, Wygnanski and Seifert demonstrated a substantial improvement in the lift coefficient ( $C_l$ ) for a flapped airfoil when the forcing was applied from the flap. The increased lift was attributed to the localized application of pulsed blowing at the flap hinge reattaching the separated flow at the flap.

For an airfoil at a flap angle of  $\delta=0^\circ$ , Wygnanski and Seifert observed that not only could the application of oscillatory blowing prolong the onset of stall for higher angles of attack ( $AOA$ ), but the instantaneous application of small amplitude oscillatory blowing

while the airfoil was stalled could often reattach the flow and thus generate an instantaneous increase in lift. Additionally, they found that lower frequency oscillations could force the reattachment of the flow more efficiently than higher frequencies. Furthermore, the optimum frequency required to maintain the reattachment may not necessarily be the same as the frequency required to initially reattach the flow.

A complete explanation for the effectiveness of small amounts of oscillatory blowing in preventing separation does not exist. It has been observed that relatively large quantities of steady blowing ( $c_\mu=0.1$ ) near the point of separation can reattach the flow and increase lift, but the steady blowing also causes a thickening of both the boundary layer and the wake behind the airfoil which leads to increased drag. In contrast, the oscillatory blowing takes advantage of inherent instabilities in the near-wall shear layer which causes the selective amplification of the input oscillation frequency. These amplified disturbances convect downstream along the airfoil as coherent large structures which serve to mix the boundary layer flow and delay separation. In contrast to steady blowing, the apparent efficiency of the mixing provides substantial increases in lift, and smaller increases in drag due to less fluid injection into the system. Moreover, Seifert et al. clearly demonstrate that there are preferential oscillation frequencies which produce the highest gains in lift and maximum angle of attack before stall.

It is well known that significant changes in lift and in the value of the *AOA* at the onset of stall occur due to compressibility. Since the experiments by Wygnanski and Seifert were limited to  $M<0.2$ , these compressibility effects did not influence their results. It is the assumption that these results can be extrapolated to qualitatively state the effectiveness of oscillatory blowing for  $M>0.3$  that has been resisted by some researchers.

Previous researchers have shown skepticism concerning the effectiveness of oscillatory blowing, or any boundary layer control mechanism for that matter, to prevent separation and enhance lift on airfoils in compressible flow. For incompressible flow regimes, Carr (1995) concurs with others in regards to the effectiveness of steady blowing

to prevent boundary layer separation and the formation of the dynamic stall vortex; however, he presents data that shows why the effectiveness of blowing techniques is questionable for compressible free-stream Mach numbers.

One of the primary changes in airfoil separation that occurs at the onset of compressibility ( $M \approx 0.3$ ) is in regard to the mechanism of stall. For lower, incompressible Mach numbers, the stall behavior is initiated by trailing-edge stall where the stalled region progresses upstream until the separated region covers almost the entire chord of the airfoil. In contrast for higher compressible Mach numbers ( $M > 0.3$ ), leading-edge stall appears to be the precursor to complete stall. The latter, leading-edge stall, occurs abruptly as the airfoil is pitched passed a critical angle of attack, while the former, trailing edge stall, evolves gradually as the angle of attack is increased.

Carr (1995) explains that the difference in stall mechanism between incompressible and compressible flow regimes is probably Mach number dependent, rather than Reynolds number dependent. Data presented by Gault (1957) shows that by increasing Reynolds number, the probability of trailing-edge stall over an airfoil increases. This is contrary to observations in other experiments, including those in the NDF; however, these other experiments were performed in atmospheric wind tunnels where Reynolds number and Mach number both increased with free-stream velocity, so their effects could not readily be separated. According to Carr, it is most likely the Mach number that dictates the stall characteristics of the airfoil. As reported by McCroskey, et al. (1981), locally supersonic flow exists near the leading edge of pitching airfoils even for free-stream Mach numbers as low as  $M=0.3$ . The existence of locally supersonic flow on the airfoil results in shock/boundary layer interaction which is believed to be the cause of the distinct changes observed in the stall mechanism as Mach number is increased into the compressible regime.

### **2.3 Objectives of NDF/TAU Airfoil Experiments**

With the previous discussion in mind, the objective of the proposed work in the NDF was to determine the effectiveness of the oscillatory blowing in the compressible regime and answer some of the criticism concerning the boundary layer control of transonic separation. To meet this objective, it was proposed that the same airfoil and the same (or similar) equipment from TAU be used in the NDF to investigate the performance of the airfoil with and without forcing in the range  $0.1 < M < 0.4$ . With these experiments, the conclusions reached with the  $M < 0.2$  static lift experiments of Wygnanski and Seifert could be verified and then duplicated in the NDF up to  $M = 0.4$ . This new research was directed in part by I. Wygnanski jointly of the University of Arizona and Tel-Aviv University and A. Seifert of Tel-Aviv University (TAU).

### **2.4 Modifications to the NDF Test Section**

The existing 1.52 m x 1.22 m cross-section test section of the NDF was modified to accommodate the NACA 0015 airfoil previously used at Tel-Aviv University for separation control experiments. These modifications were necessary to reduce the height of the wind tunnel test section to 0.61 m in order to accommodate the airfoil and increase the maximum free-stream velocity of the wind tunnel to  $M = 0.45$ . This smaller test section is one-half the original cross section and is one-twelfth the length of the original test section and was designed specifically for the NACA 0015 airfoil from Tel-Aviv University.

The design for the high-speed test section is shown in Figure 2.1 along with the airfoil model to show scale. The high-speed test section was created by inserting a secondary contraction into the first test section module, cutting the free-stream cross-section in half. The length of the high-speed test section in Figure 2.1 is 0.86 m (1 floor panel). Following the high-speed test section is a diffuser which expands the flow back to the original test section cross-section of 1.52 m x 0.61 m over the length of 6.9 m. (See Mazanec, 1996, for complete details on the high-speed test section design).

## 2.5 NDF Performance with Airfoil in Test Section

The performance of the wind tunnel was also examined with the airfoil installed in the one-panel high-speed test section as shown in Figure 2.1. The free-stream velocity over the full range of fan RPM was measured at a constant fan blade pitch of 27° with and without the airfoil installed, and the results are shown in Figure 2.2 (bottom). It was observed that the presence of the airfoil resulted in a large enough pressure loss due to blockage and drag that the absolute top speed in the high speed test section was reduced 11% from 160 m/s to 142 m/s. Figure 2.2 (top) shows the performance characteristics of the empty high-speed test section over the entire range of fan RPM and blade pitch.

## 2.6 Experimental Apparatus

Besides the extensive changes to the NDF test section, this experiment also required the design of a specialized support system to mount the Tel-Aviv NACA 0015 airfoil securely within the contracted NDF test section but still allow for adjustments of AOA while the flow was at maximum velocity. The airfoil was mounted vertically in the test section as seen photographically in Figure 2.3. The airfoil was mounted by an assembly (Figure 2.4) which consisted of a pair of disks that were flush with the inner surface of the test section and 7075T651 aluminum spindles which would allow angle of attack adjustments. The disks also had a series of holes to adjust the flap angle from +/-30° in 10° increments. The spindles were hollow and provided both the connection of the airfoil to the support and also the means by which the pulsated compressed air would enter the plenum chamber within the airfoil. The factor of safety of the spindles under an  $M=0.8$  flow (the original design expectation) was estimated at 4.6 by standard beam analysis. Table 2.1 summarizes a few representative loads measured during the course of the experiments. At the maximum velocity, the largest recorded lift was about 940 lb. which indicates that the overall factor of safety of the current airfoil support is about 12. Complete details of the airfoil design are available in Peterson (1995).

Table 2.1. Observed Airfoil Loads.

$C_l$	$U_\infty$ (m/s)	Lift (N)	Lift (lb <sub>f</sub> )
0.45	0.13	115	25.9
1.43	0.17	641	144
0.99	0.41	2480	557
1.17	0.41	2860	642
1.51	0.39	3810	857
1.69	0.39	4180	940

Figure 2.5 shows a schematic representation of the experimental apparatus. The NACA 0015 airfoil had a single row 36 static pressure taps around the perimeter of the airfoil located at the center of span. The taps were spaced closely near the leading edge up to about 5% chord, after which the distance between taps was approximately  $x/C=0.05-0.1$ . There was also a single tap located at the trailing edge. Each of the static pressure taps was connected with 0.063" vinyl tubing to a 48 port J9 Scanivalve. In addition, a Pitot probe was used to measure free-stream velocity and provide a reference for each of the airfoil static pressure taps. The Scanivalve control was operated remotely by computer and each of the pressure taps was sampled sequentially using a Validyne DP-103 pressure transducer calibrated to 1990 Pa/V. Oscillatory blowing was supplied via a compressed air source with a stagnation pressure of approximately 10 atmospheres. The amplitude of the blowing was modulated manually by a hand valve and the frequency of the blowing was controlled by computer with a variable frequency drive and 3 HP motor which drove a variable speed "daisy-wheel" valve. This valve was designed and supplied by Tel-Aviv University and consisted of two stationary disks with a rotating disk sandwiched between them. Each of the disks had five radial slots cut into them so that in the plan view, they each had a flower-like appearance. By rotating the center disks, the radial slots would either be aligned so that flow could pass through, or the slots would obscure each other so that flow was restricted. During the experiments the oscillations were verified by

observing the output of a small microphone connected by tubing to the airfoil plenum chamber.

## 2.7 Results of NDF/TAU Airfoil Experiments

A series of tests were completed on the NACA 0015 airfoil equipped with an adjustable 25% chord flap and several spanwise linear slots at 0%, 10%, and 75% chord through which oscillatory wall-jets were introduced. Figure 2.6 (top) shows the location and direction of the blowing relative to the airfoil cross-section. Additionally, Figure 2.6 (bottom) shows the velocity profile of the leading edge jet as measured by a total pressure tube and the location of the hot-wire used for the calibration of the mean and oscillatory blowing.

The mean and oscillatory components of the slot blowing were measured by hot-wire at the exit of the leading edge slot and calibrated to the pressure of the compressed air supplied to the daisy-wheel valve. Figures 2.7 and 2.8 show the results of these calibrations. It can be observed in these two figures that the oscillatory component of the forcing saturates between 2.0 and 2.5 kg/cm<sup>2</sup>, depending on the frequency of oscillation. This was an unfortunate limitation which prevented experiments using high amplitude forcing. In addition, it was also observed that resonance of the blowing system caused preferential frequencies to be dominant, so a continuous sweep of frequency of oscillation was not possible. Because of these limitations, the experiments were limited to oscillation frequencies of 270, 490 and 840 Hz.

With these calibrations, the baseline forces and pressure distribution were measured for the NACA 0015 airfoil over the range  $0.1 < M < 0.4$  for several different forcing amplitudes and frequencies. Figure 2.9 (top) shows the unforced (baseline) lift coefficient for the 0° and 10° flap. Referring to this figure, stall will be defined at the angle where  $C_l$  begins to decrease.

Under the direction of Dr. L. Carr (NASA-Ames), the airfoil was tufted and observed with and without oscillatory blowing through the leading edge slot at 490 Hz with

$C_\mu \approx (0.01; 0.01)\%$  and a flap angle of  $\delta = 0^\circ$ . Figure 2.9 (bottom) shows the effect of unsteady blowing on the stall angle. It was observed that the greatest enhancement to lift and stall angle occurred for low free-stream velocities ( $M < 0.3$ ), but there was still a noticeable effect even up to  $M = 0.41$ . These preliminary tests demonstrate that there was an observable effect of the oscillatory blowing, although at the time of measurement, it was unclear whether the leveling off of the  $AOA$  increment ( $\Delta AOA/AOA_{baseline}$ ) for  $M > 0.3$  was due to compressibility or the forcing technique itself.

With 840 Hz forcing applied at an amplitude of  $C_\mu = (0.02; 0.02)\%$ , Figure 2.10 shows the enhancement in lift coefficient due to the oscillatory blowing for three successive Mach numbers. In Figure 2.10a, b, and c, the forcing was applied from the leading edge with the flap at  $0^\circ$ , while in Figure 2.10d, the forcing was applied at the flap with a flap angle of  $10^\circ$ . In the case of the  $0^\circ$  flap airfoil, the effect of the forcing on lift seems to diminish for increasing Mach number. For the  $10^\circ$  flap, the oscillatory blowing demonstrates a uniform increase in lift for all  $AOA$ , including those where the airfoil is technically not stalled. This is attributed to separation at the flap hinge which is reattached due to the forcing.

The pressure distribution around the airfoil clearly shows the effect of oscillatory blowing on a stalled airfoil. In Figure 2.11 are the forced and unforced pressure coefficients,  $C_p$ , for the airfoil at  $M = 0.18$  and  $0.32$ . The airfoil was initially stalled in the unforced case. In both of these plots in Figure 2.11, the application of oscillatory blowing from the leading edge results in the re-establishment of the high suction peak, good pressure recovery along the airfoil, and a trailing edge pressure that more closely matches the Kutta condition. The end result of these changes in pressure distributions is that the lift coefficient is increased by about 80% over the stalled airfoil lift coefficient.

At the highest Mach number,  $M = 0.41$ , the pressure coefficient distribution and the lift coefficient were measured for  $0^\circ$  and  $10^\circ$  flap angle with and without 840 Hz leading

edge forcing. These data are shown in Figure 2.12 and seem to indicate a partial reattachment of the flow due to the oscillatory blowing and a 10 to 50% increase in lift over the baseline stalled airfoil. Additionally, the  $-C_{p_{max}}$  of nearly 5.0 after the application of forcing indicates that the flow is supercritical over part of the airfoil, whereas it was not before the application of oscillatory blowing. This demonstrates that the oscillatory blowing technique has the potential to control separation even under supersonic flow conditions.

Figure 2.13 (left) shows examples of several experiments that were performed using two different blowing frequencies (270Hz and 840Hz) and two flap angles ( $\delta_f=0^\circ$  and  $10^\circ$ ) with a constant blowing momentum coefficient of  $C_\mu=(0.02;0.02)\%$ . It can be seen when forcing was applied from the leading edge, the oscillatory blowing gives a more prominent improvement in lift increment ( $\Delta C/C_l$ ) with  $\delta_f=0^\circ$  as compared to the  $\delta_f=10^\circ$ . This may be a result of the choice of the forcing location and suggests a possible modification to the experiment. Since separation occurs at the leading edge for  $\delta_f=0^\circ$  while separation can occur from both the leading edge and the flap hinge when  $\delta_f=10^\circ$  at the higher Mach numbers, one possible enhancement to this experiment could be to apply blowing selectively from either the leading edge or flap slots or both simultaneously. Additionally, it can be seen that the 840 Hz forcing is apparently more effective at controlling separation than the 270 Hz blowing and suggests that the enhancement due to blowing is frequency dependent.

Figure 2.13 (right) demonstrates the effect of leading edge smoothness on the ability of the forcing technique to improve lift. Plotted in this figure are two different baseline conditions, one with the leading edge forcing slot covered with tape to smooth the leading edge, and one with no tape. Comparison of the lift coefficients for the two baseline cases to the equivalent case with forcing shows that the condition of the leading edge strongly influences the measured increase in lift. It was seen that the improvement in lift could either be 12% or 50% depending on whether the unforced case had a taped or

untaped leading edge. Under flight conditions, the obvious comparison would be with the untaped leading edge, unless the leading edge was somehow mechanically smoothed when the blowing was not being applied.

Two sets of experiments were performed in an attempt to separate the compressibility effects from the  $C_\mu$  effects. The first was to simply plot the lift increment,  $\Delta C/C_l$ , as a function of both Mach number and the corresponding dimensionless forcing frequency,  $F^+$ . Figure 2.14 (top) indicates that there is sensitivity to the forcing frequency at the higher Mach numbers, which is similar in both magnitude and  $F^+$  to results previously published by Seifert and Wygnanski for the lower Mach numbers. Although a noticeable decrease in  $C_l$  is seen for  $M>0.3$ , there still remains some uncertainty about how much of the decrease in  $\Delta C_l$  can be attributed to  $F^+$  effects,  $C_\mu$  effects, or compressibility effects.

The second experiment compared the effect of oscillatory blowing under similar stall conditions over the range  $0.17 < M < 0.41$  where the initial “depth into stall” was kept constant at each Mach number before the application of oscillatory blowing. In Figure 2.14 (bottom), the “baseline”  $C_l$  was maintained constant over the full range of Mach numbers by varying the post-stall *AOA* for each Mach number until  $C_l$  was the same for each velocity. Then, the oscillatory blowing was applied at 270Hz and 840Hz at a constant blowing momentum coefficient of  $C_\mu=(0.02;0.02)\%$ . As shown in Figure 2.14 (bottom), this resulted in producing a nearly constant increase in  $C_l$  for the 270Hz forcing and a  $F^+$  dependent increase in  $C_l$  for the 840Hz case. The location of the peak  $C_l$  at  $F^+=2.9$  seems to agree with some of the previous results of Wygnanski and Seifert. It is postulated that this peak does not appear in the 270Hz measurements because the Mach number corresponding to  $F^+=2.9$  is about 3 times lower than that of the 840Hz measurements, and it was not possible to obtain reliable data at low velocities.

Finally the effect of hysteresis was investigated. Figure 2.15 shows that the improvement in lift is independent of the manner in which the forcing is applied. In this

figure, the square symbols represent the pressure distribution when the *AOA* is set to a low, unstalled baseline angle before turning the forcing on and moving the airfoil to the previously stalled *AOA*. The diamond symbols represent the pressure when the forcing is turned on suddenly while the airfoil is under a stalled condition. It is clear that pressure distribution is nearly identical for these two methods of applying the forcing.

## 2.8 Conclusions and Recommendations

These measurements have given a possible explanation for earlier conclusions and concerns about the apparent lack of effectiveness of separation-control schemes in the compressible regime ( $M>0.3$ ). It is encouraging that lift-enhancement was observed over the entire range  $0.1 < M < 0.4$ , even with the small amount of unsteady blowing applied in these experiments. Additionally, the observation that supercritical flow was achieved due to the application of the oscillatory blowing shows that the technique can be extended successfully to even higher Mach numbers. The fact the hysteresis appears not to be an important factor in oscillatory forcing shows promise that the technique can be used in maneuvering high-speed aircraft.

The obvious extension of this work would be to perform experiments with a controlled matrix of parameters including the variation in the forcing frequency, Mach number, and the blowing momentum coefficients. However, due to limitations of the current apparatus, it was not possible to vary the frequency of the oscillations and still maintain a constant amplitude of the blowing pulses. It was also observed that above a momentum coefficient of  $C_\mu=(0.02;0.02)\%$  at the highest Mach number, the oscillations would saturate in amplitude and soon be dominated by the mean jet flow, thus the apparatus was unable to produce fluctuating  $C_\mu$  higher than 0.02%.

This work could be extended by redesigning the oscillation generator to provide a greater flexibility in the selection of  $F^*$  and  $C_\mu$  thus allowing for a complete parametric

study of the current technique. Also, with a working knowledge of the 2-D static separation control by oscillatory blowing, the technique could be extended to 3-D swept wings or used to control dynamic stall. In particular, the effects of oscillatory blowing in an unsteady flow would have implications in the design of helicopter blades as well as highly maneuverable aircraft where the control of lift and roll moment could be assisted or performed entirely by the selective application of pulsed blowing through the wing surface.

## 2.9 References

Carr, L.W. and Chandrasekhara, M.S., "An Assessment of the Impact of Compressibility on Dynamic Stall," AIAA-95-0779, 33rd Aerospace Sciences Meeting, Reno, NV, 1995.

Gault, D.E., "A Correlation of Low-Speed, Airfoil-Section Stalling Characteristics With Reynolds Number and Airfoil Geometry," NACA TN 3963, March 1957, as cited by Carr, L.W. and Chandrasekhara, M.S., "An Assessment of the Impact of Compressibility on Dynamic Stall," AIAA-95-0779, 33rd Aerospace Sciences Meeting, Reno, NV, 1995.

Mazanec, M.J., "Design of Research Equipment for Use in the National Diagnostic Facility," M.S. Thesis, Illinois Institute of Technology, May 1996.

McCroskey, W.J., McAlister, K.W., Carr, L.W., Pucci, S.L., Lambert, O., and Indergand, R.F., "Dynamic Stall on Advanced Airfoil Sections," Journal of the American Helicopter Society, July 1981, p.40, as cited by Carr, L.W. and Chandrasekhara, M.S., "An Assessment of the Impact of Compressibility on Dynamic Stall," AIAA-95-0779, 33rd Aerospace Sciences Meeting, Reno, NV, 1995.

Peterson, B.A., "Design of Experimental Equipment for Use in the National Diagnostic Facility," M.S. Thesis, Illinois Institute of Technology, December 1995.

Seifert, A., Bachar, T., Koss, D., Shepshelovich, M. and Wygnanski, I., "Oscillatory Blowing: A Tool to Delay Boundary-Layer Separation," AIAA Journal, Vol. 31, No. 11, p. 2052, 1993.

Wygnanski, I. and Seifert, A., "The Control of Separation by Periodic Oscillations," AIAA-94-2608, 18th AIAA Aerospace Ground Testing Conference, Colorado Springs, CO, 1994.

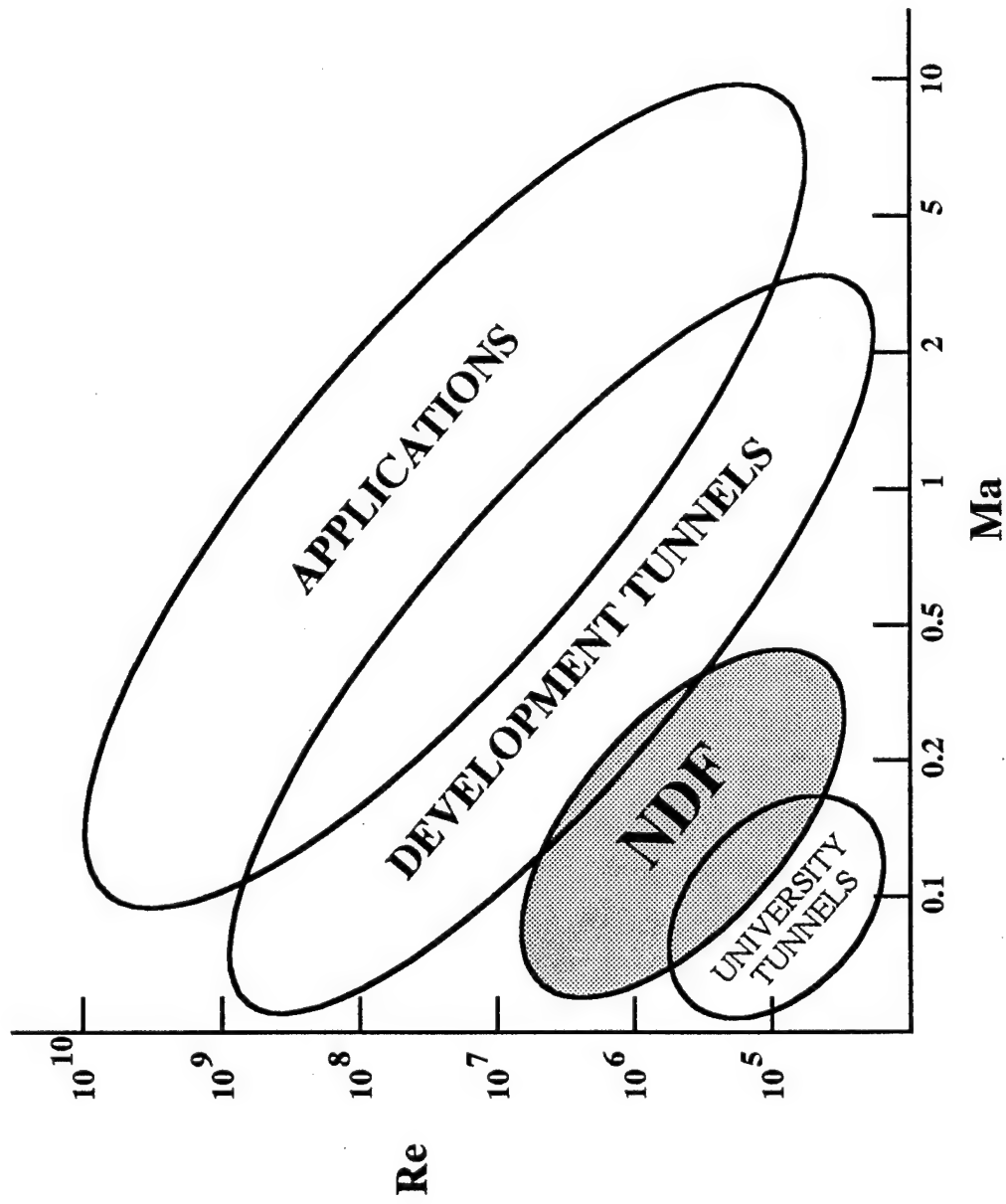


Figure 1.1. Operational Range of the NDF Compared to Current Needs and Resources

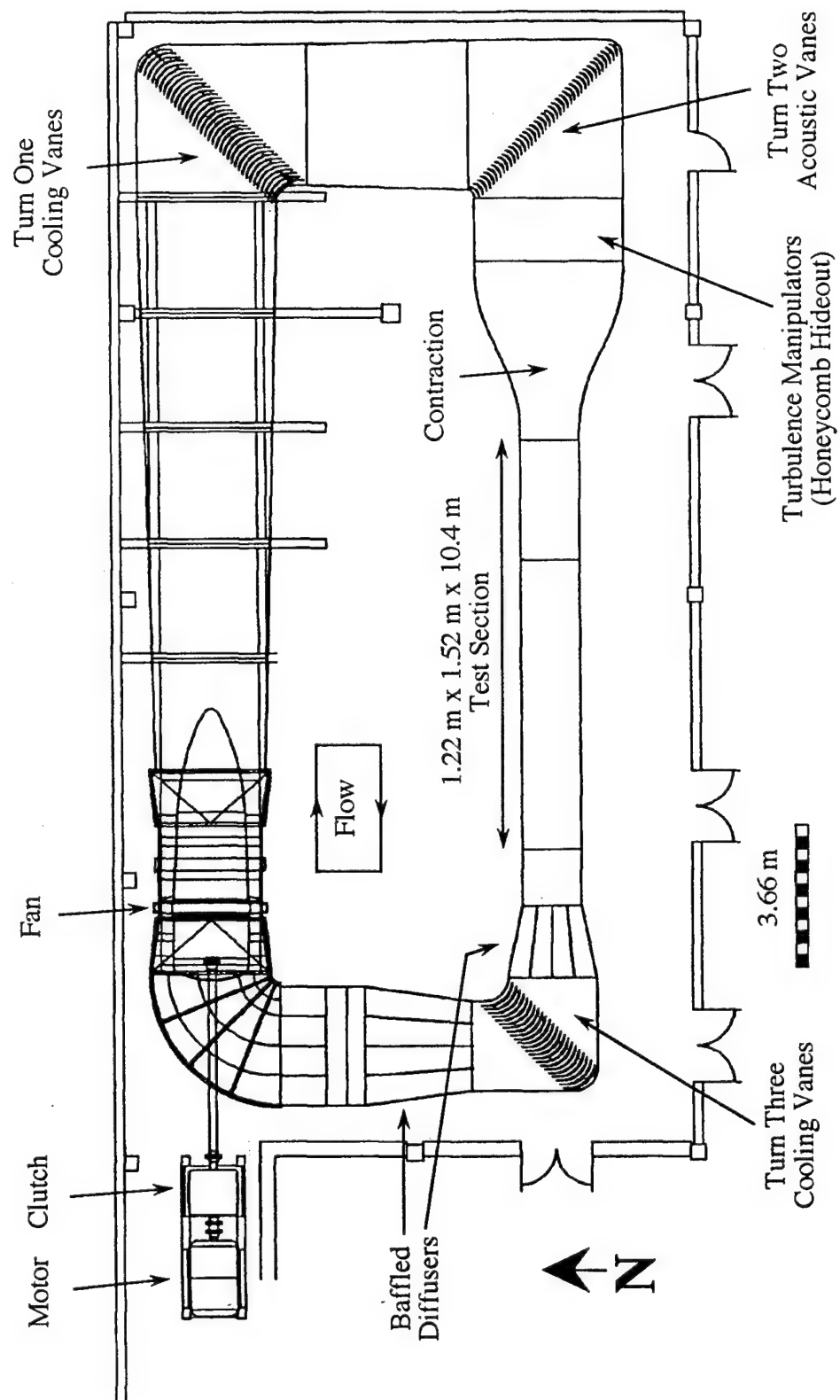


Figure 1.2. Plan View of the National Diagnostic Facility

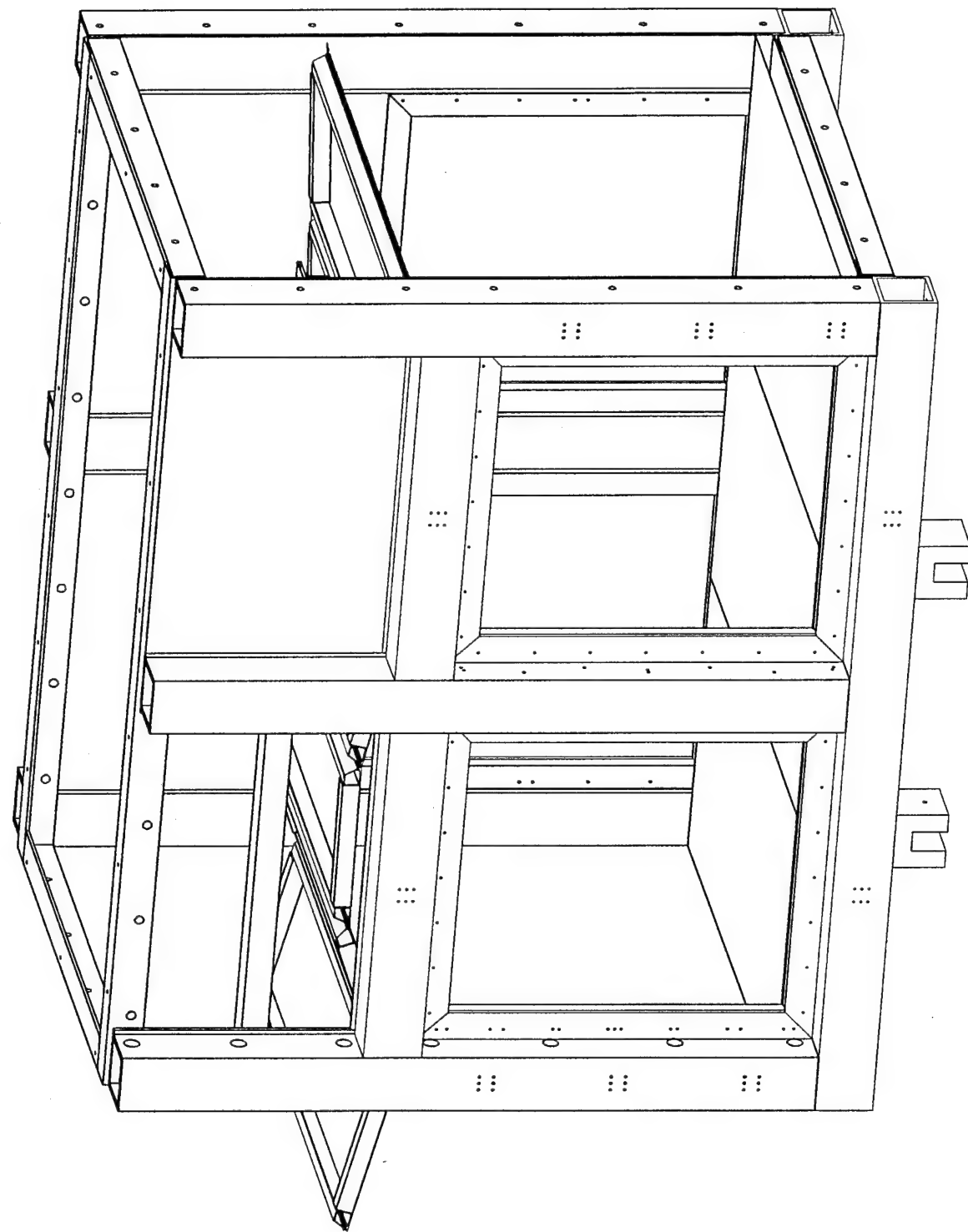


Figure 1.3. NDF Test Section Module (Typical of Four)

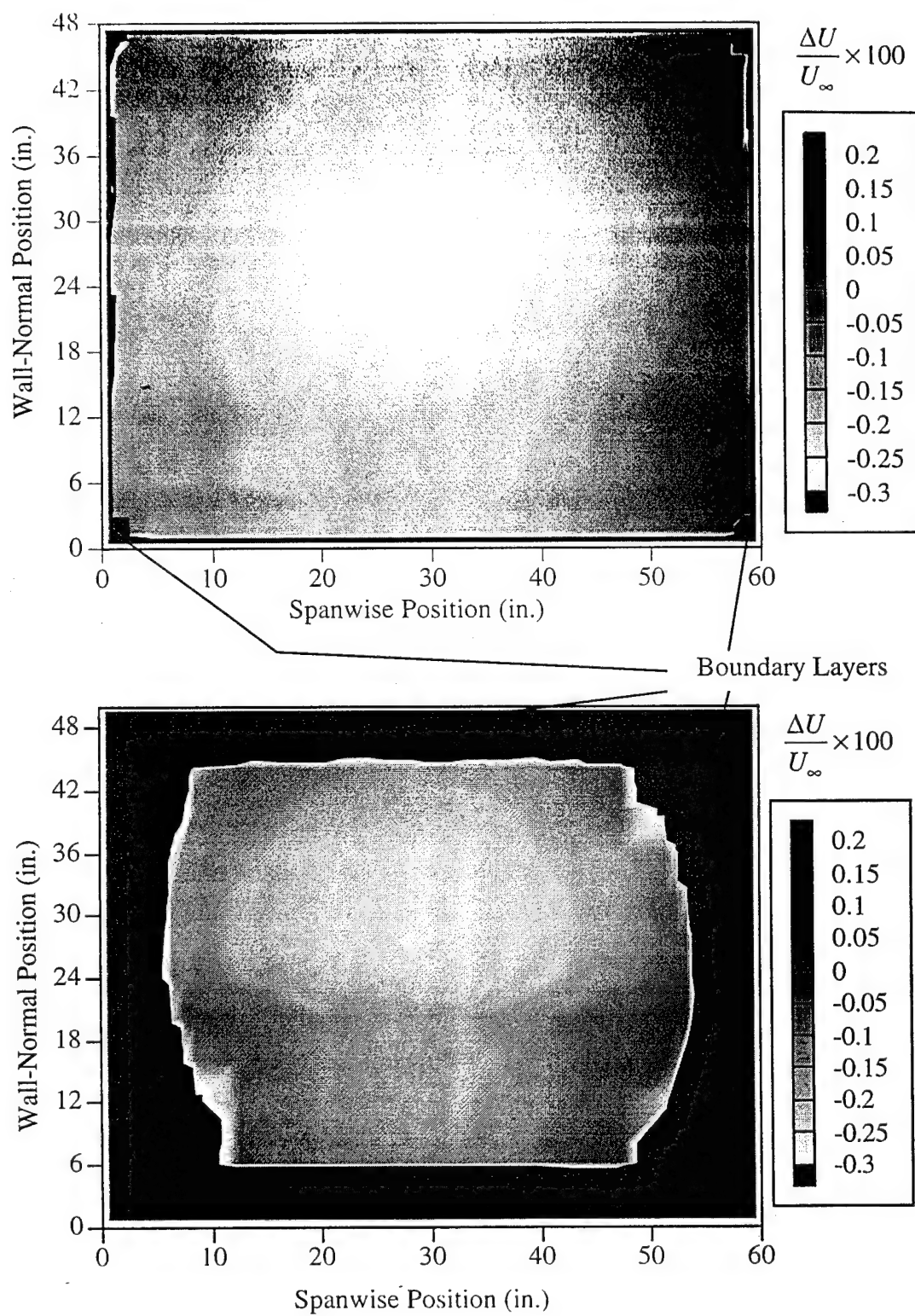


Figure 1.4. Filled Contour Plot of the Mean Velocity Uniformity of the NDF Test Section at 25 cm (top) and 890 cm (bottom) Downstream of the Contraction Exit

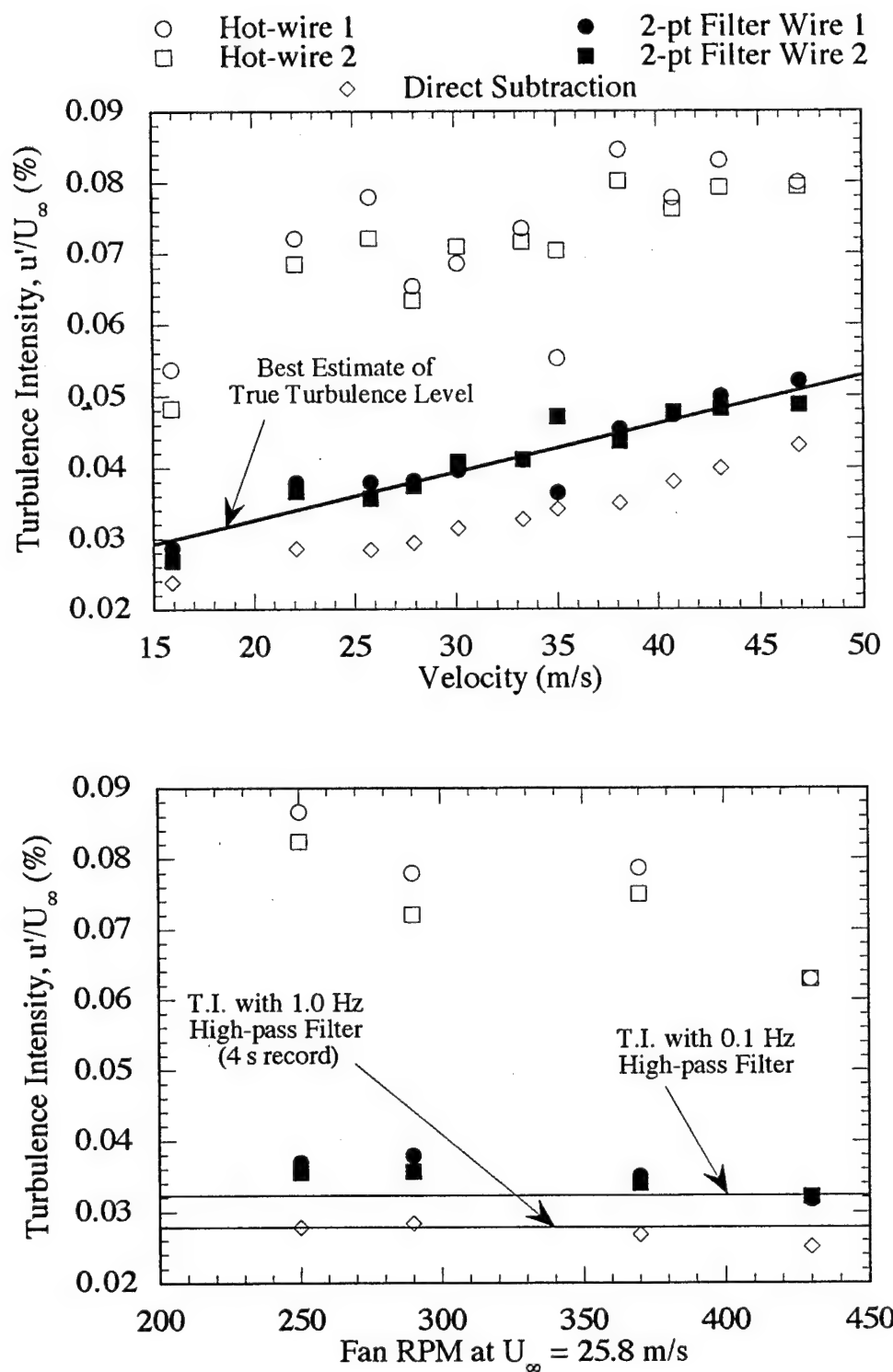


Figure 1.5. Measured Turbulence Levels at 79 cm Downstream of the Contraction Exit in the NDF (top) and the Effect of High-Pass Filtering the Hot-Wire Signal (bottom)

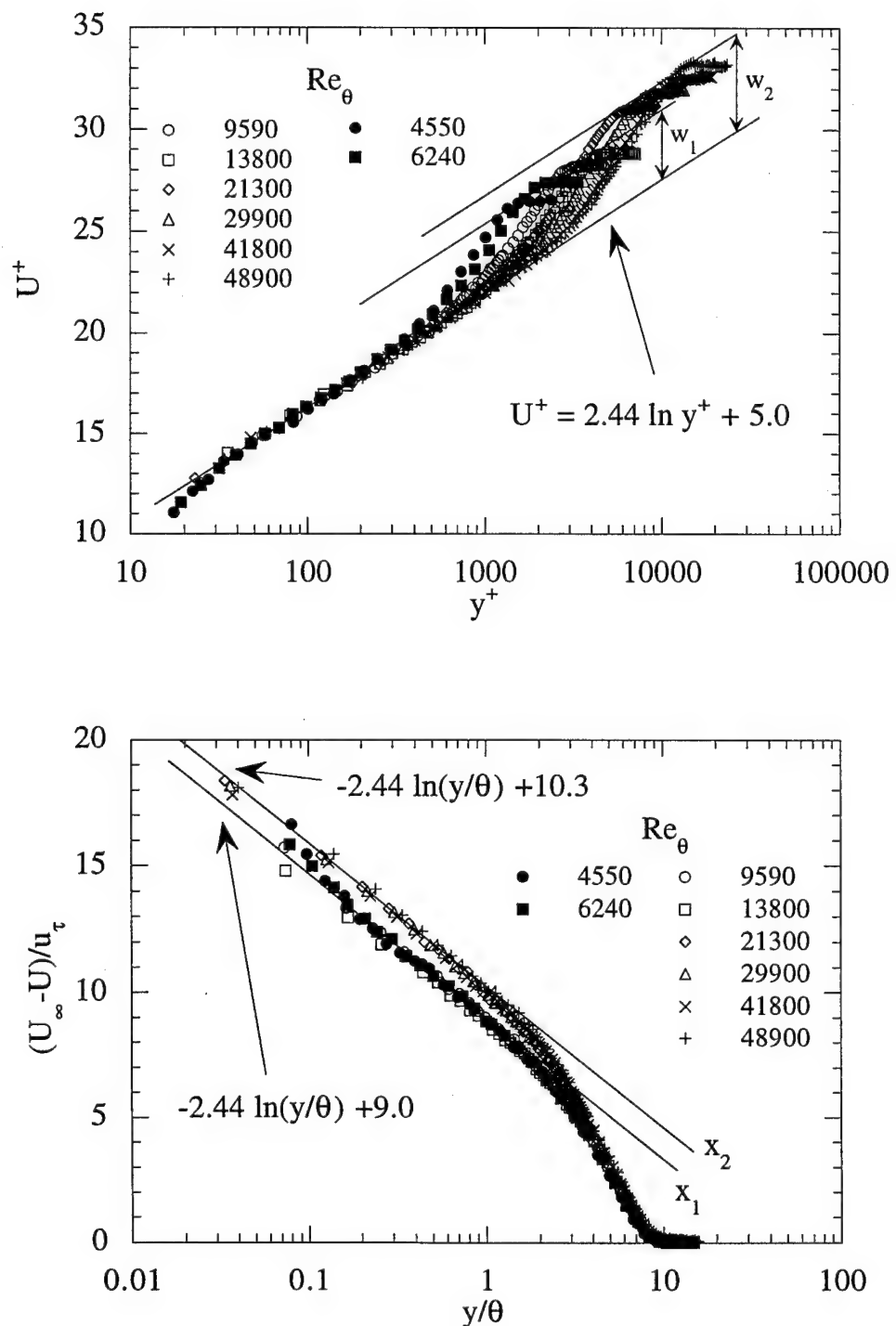


Figure 1.6. NDF Floor Boundary Layer Wall-Scaling (top) and Outer-Scaling (bottom) of the Streamwise Mean Velocity Profiles. Open Symbols are NDF Data and Closed Symbols are from Naguib (1992)

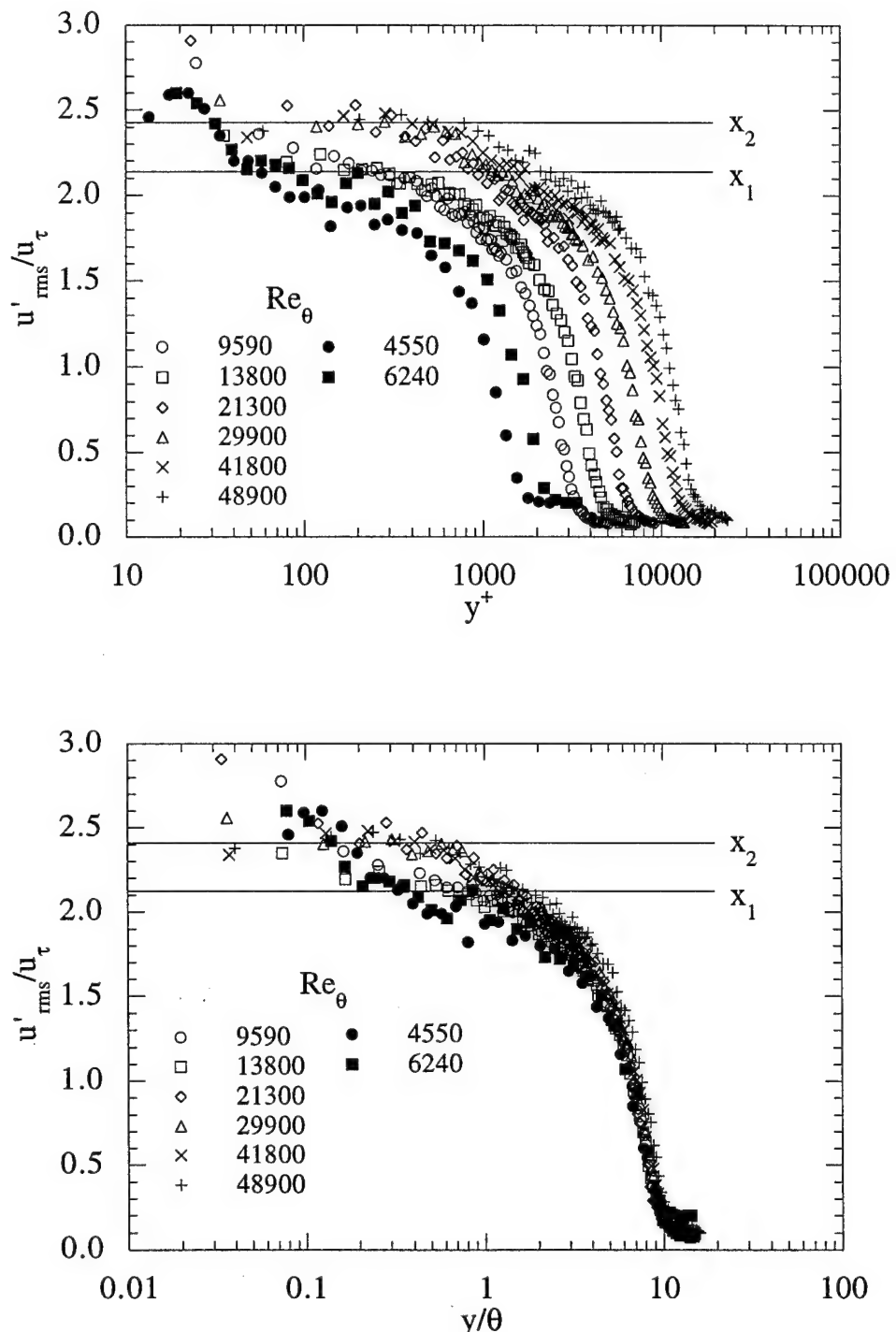


Figure 1.7. NDF Floor Boundary Layer Wall-Scaling (top) and Outer-Scaling (bottom) of the Streamwise RMS Velocity Profiles. Open Symbols are NDF Data and Closed Symbols are from Naguib (1992)

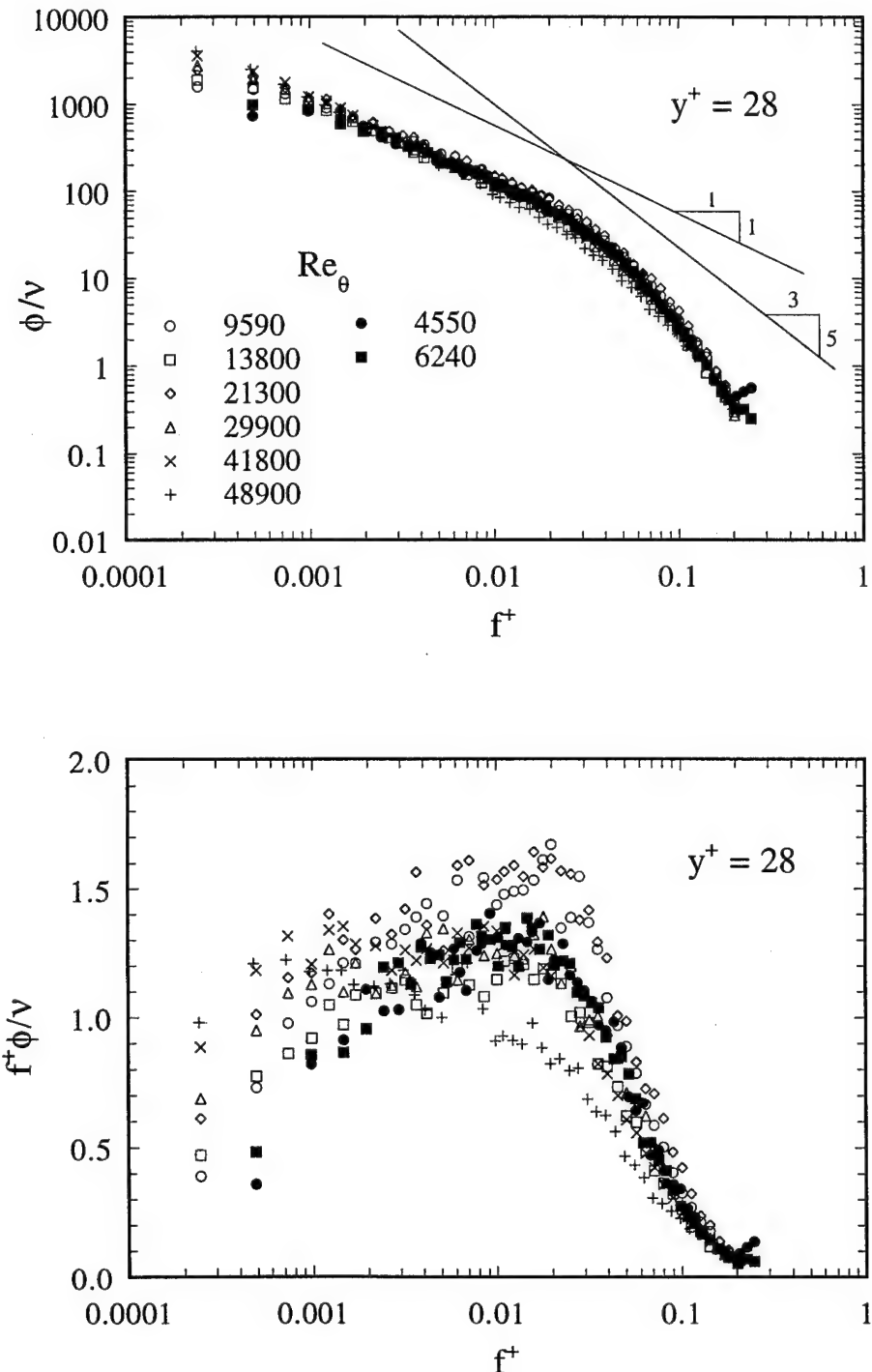


Figure 1.8. NDF Floor Boundary Layer Wall-Scaling Characteristics of the Streamwise Velocity Spectra in the Buffer region at  $y^+=28$  Using Log-Log (top) and Semi-Log (bottom) coordinates. Closed Symbols from Naguib (1992)

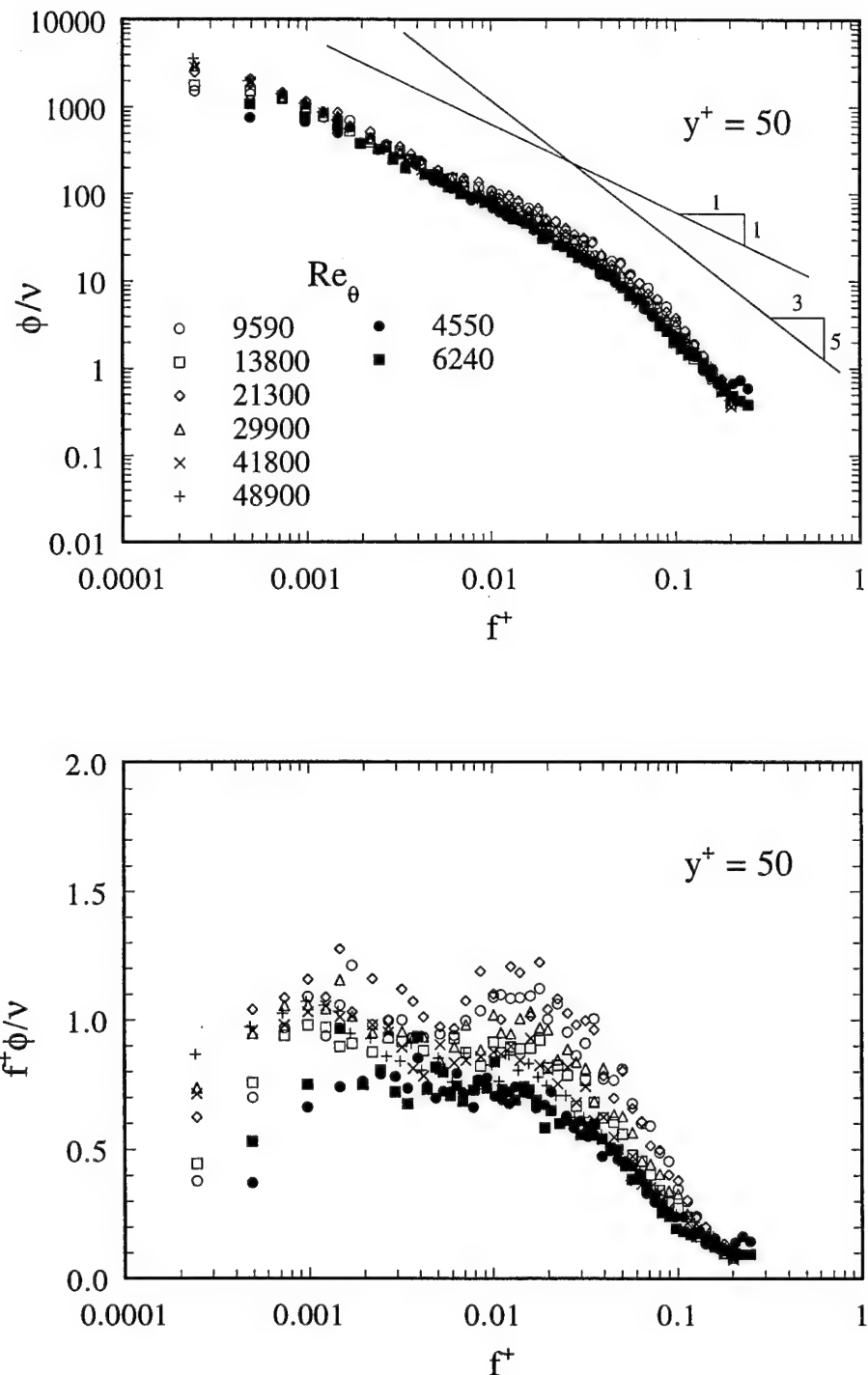


Figure 1.9. NDF Floor Boundary Layer Wall-Scaling Characteristics of the Streamwise Velocity Spectra in the Buffer region at  $y^+ = 50$  Using Log-Log (top) and Semi-Log (bottom) coordinates. Closed Symbols from Naguib (1992)

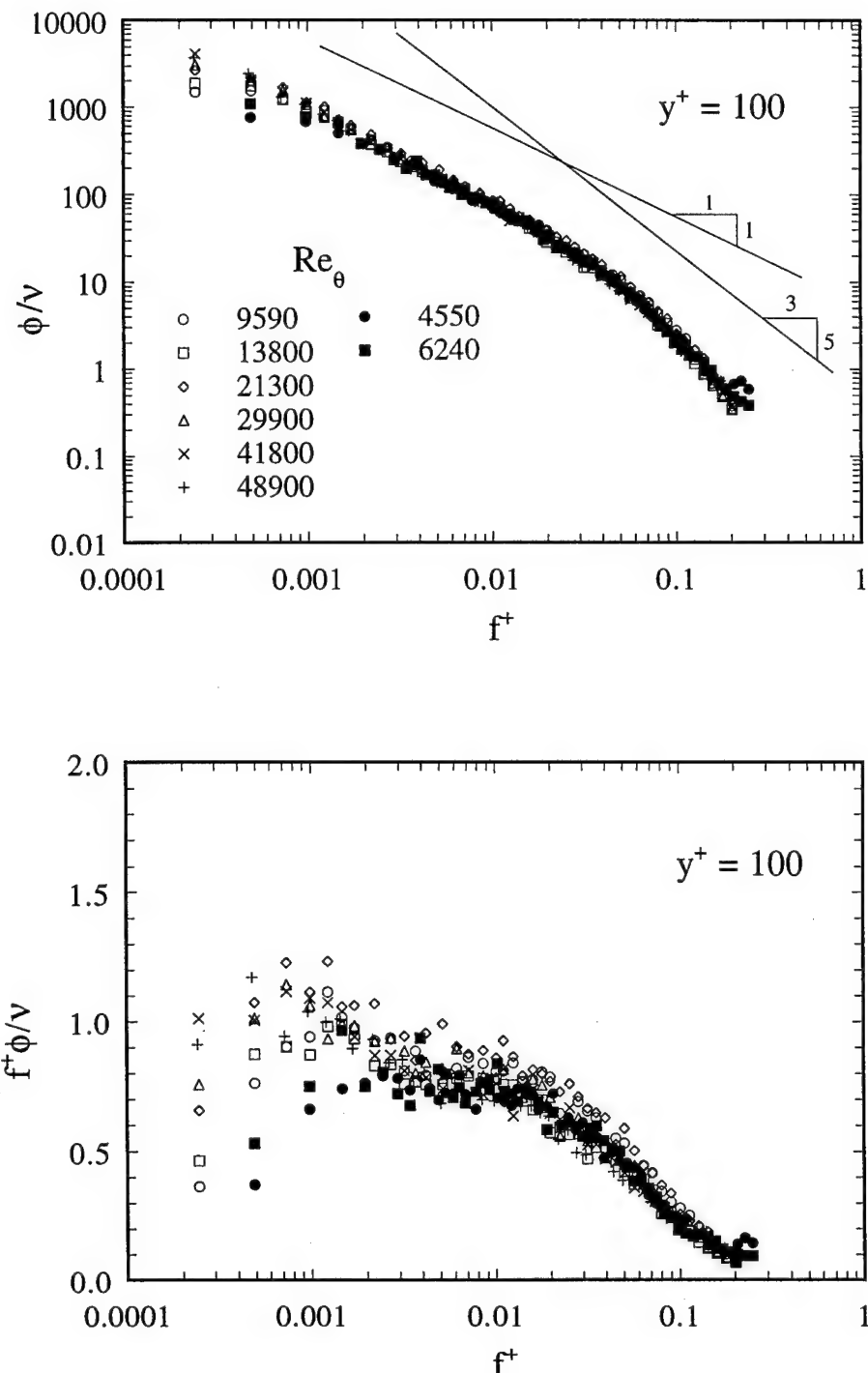


Figure 1.10. NDF Floor Boundary Layer Wall-Scaling Characteristics of the Streamwise Velocity Spectra in the Logarithmic region at  $y^+ = 100$  Using Log-Log (top) and Semi-Log (bottom) coordinates. Closed Symbols from Naguib (1992)

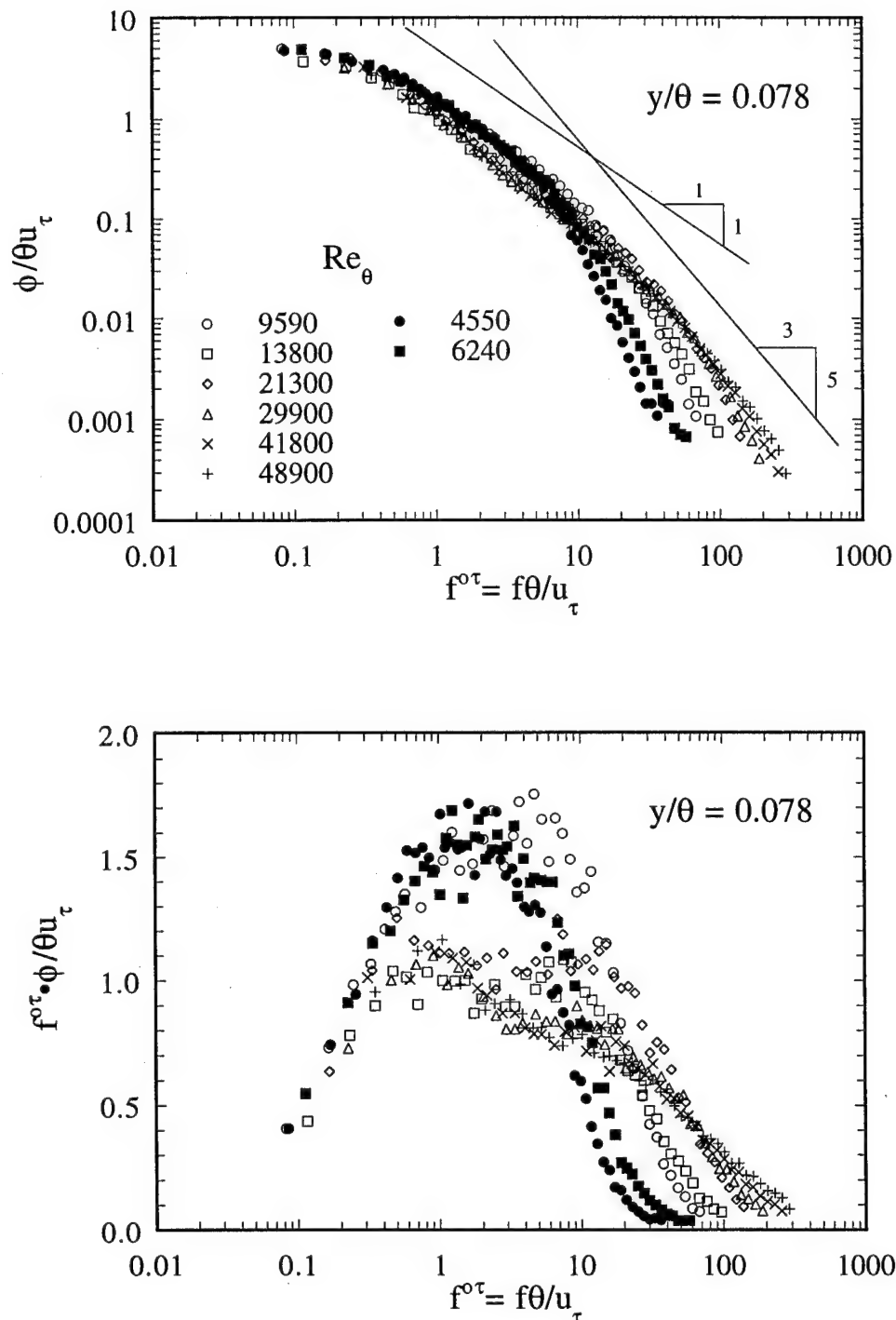


Figure 1.11. NDF Floor Boundary Layer Outer-Scaling Characteristics of the Streamwise Velocity Spectra in the Buffer region at  $y/\theta=0.078$  Using Log-Log (top) and Semi-Log (bottom) coordinates. Closed Symbols from Naguib (1992)

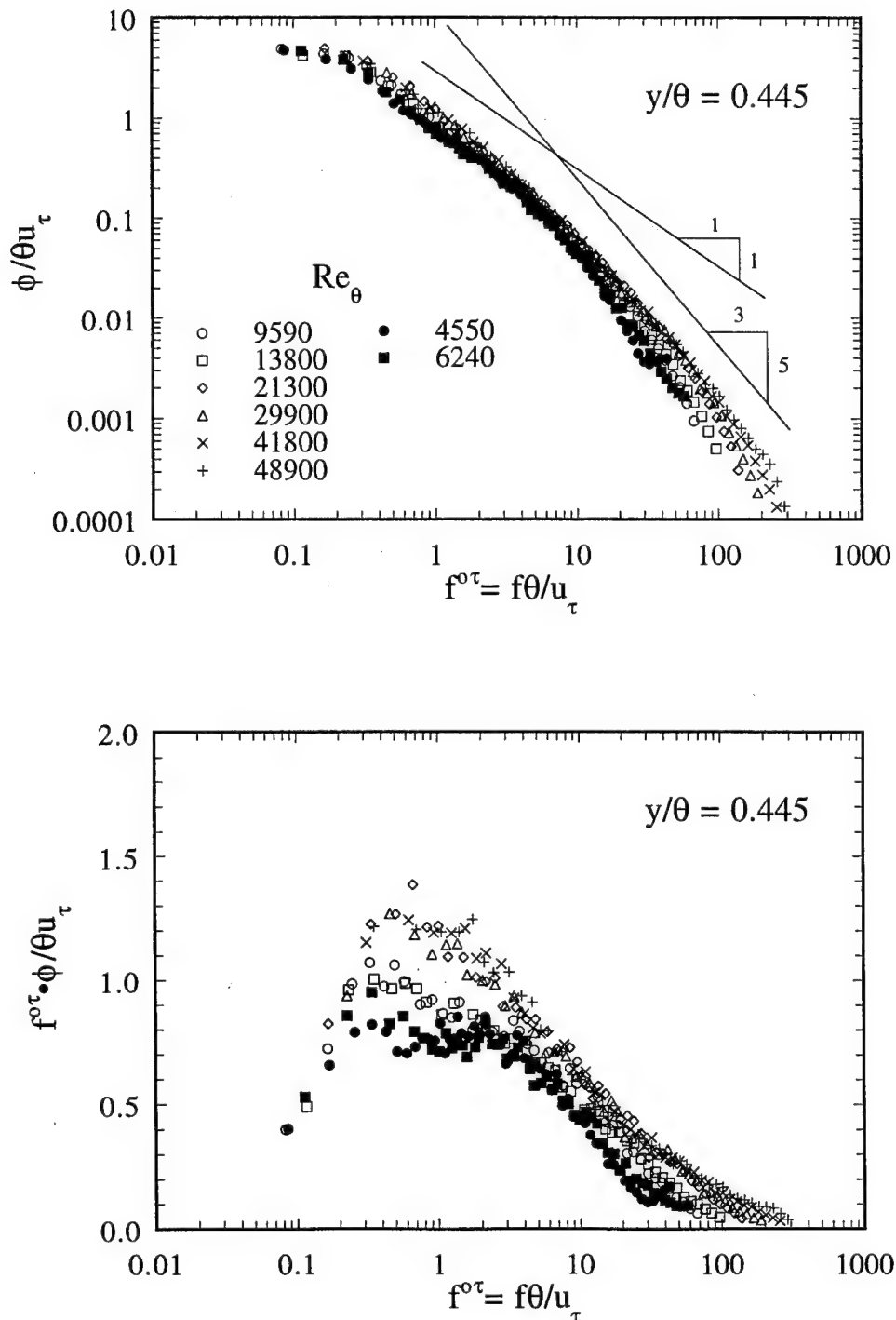


Figure 1.12. NDF Floor Boundary Layer Outer-Scaling Characteristics of the Streamwise Velocity Spectra in the Logarithmic region at  $y/\theta=0.445$  Using Log-Log (top) and Semi-Log (bottom) coordinates. Closed Symbols from Naguib (1992)

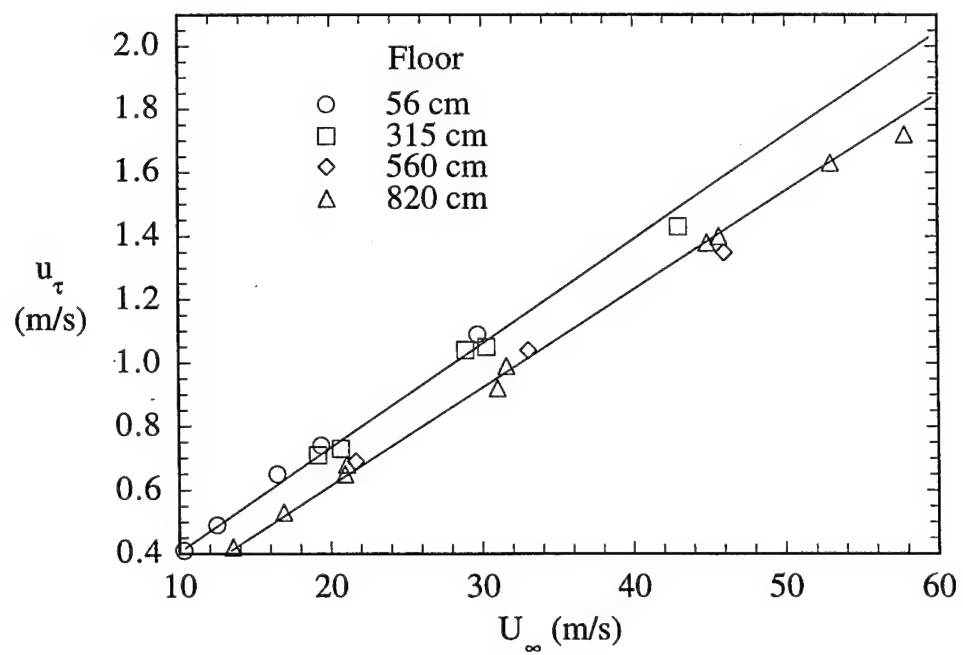
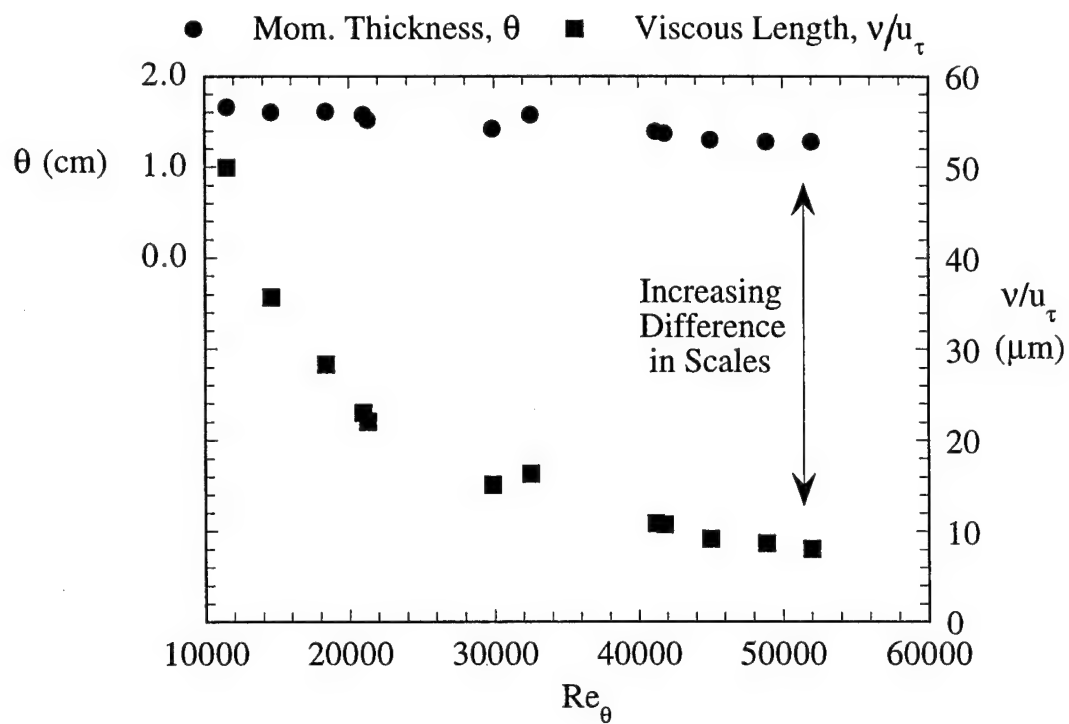


Figure 1.14. Increasing Disparity Between Inner and Outer Scales for the NDF Floor Boundary Layer (top) and  $Re_x$  Dependence of Friction Velocity (bottom)

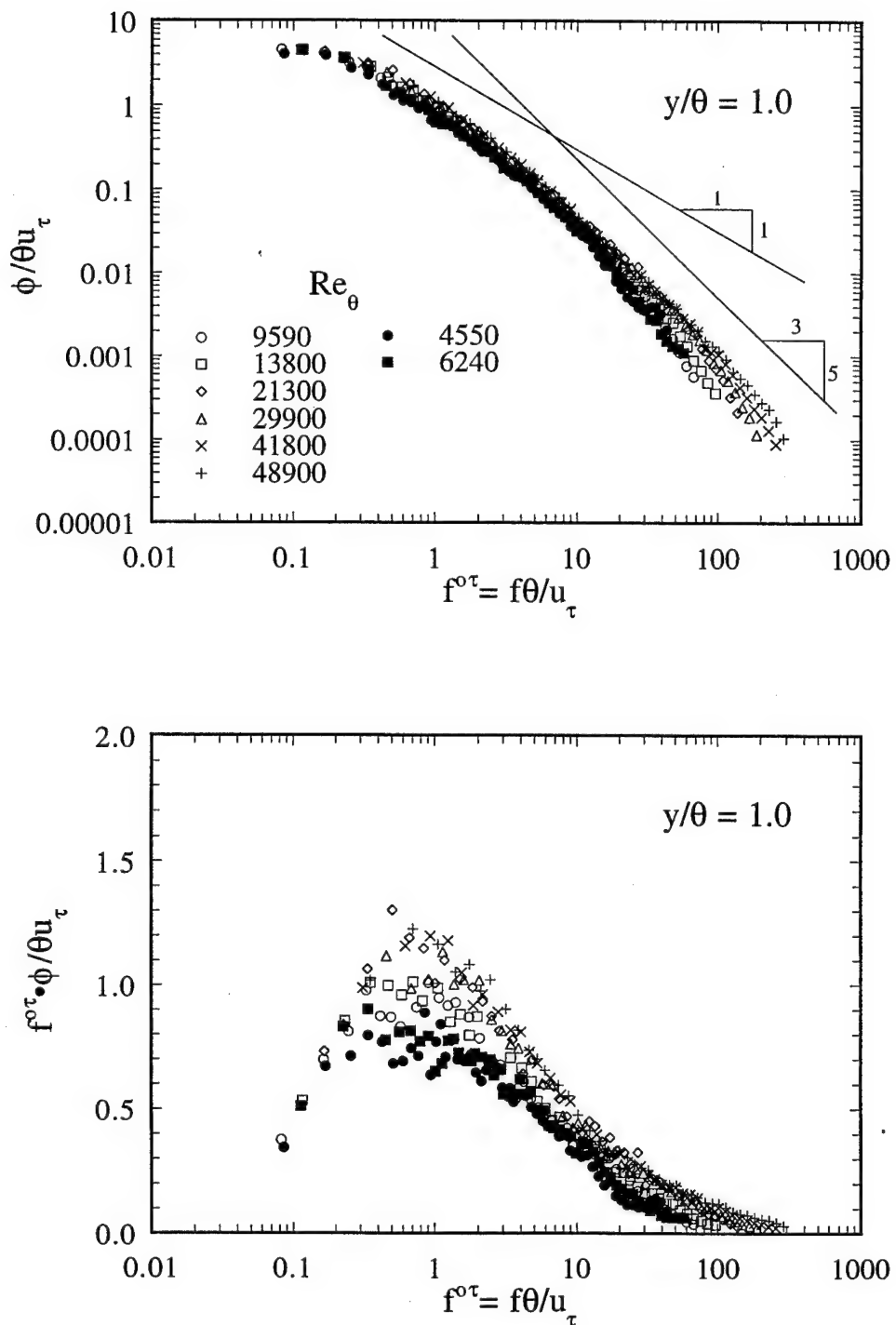


Figure 1.13. NDF Floor Boundary Layer Outer-Scaling Characteristics of the Streamwise Velocity Spectra in the Logarithmic region at  $y/\theta=1.0$  Using Log-Log (top) and Semi-Log (bottom) coordinates. Closed Symbols from Naguib (1992)

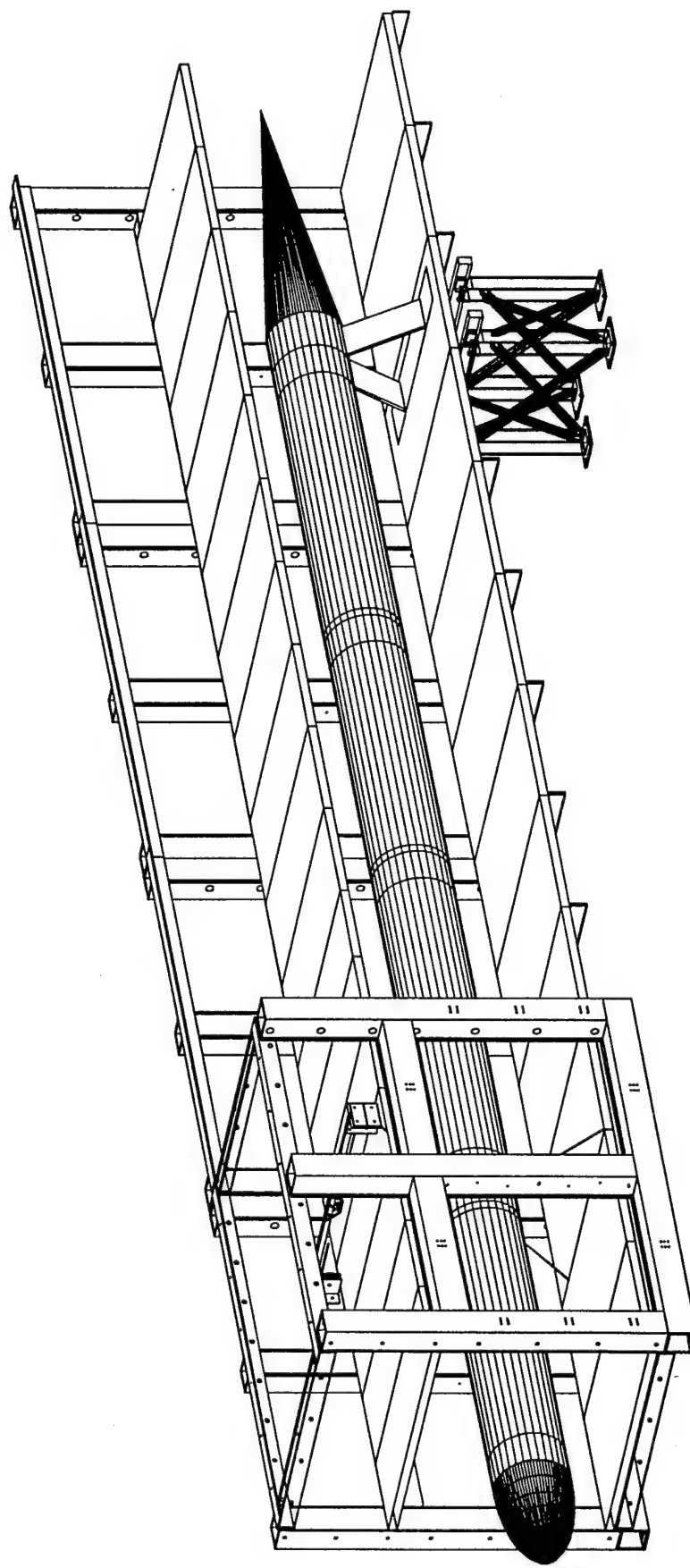


Figure 1.15. Drawing of 18-Inch Diameter Cylinder Model Mounted in the NDF Test Section

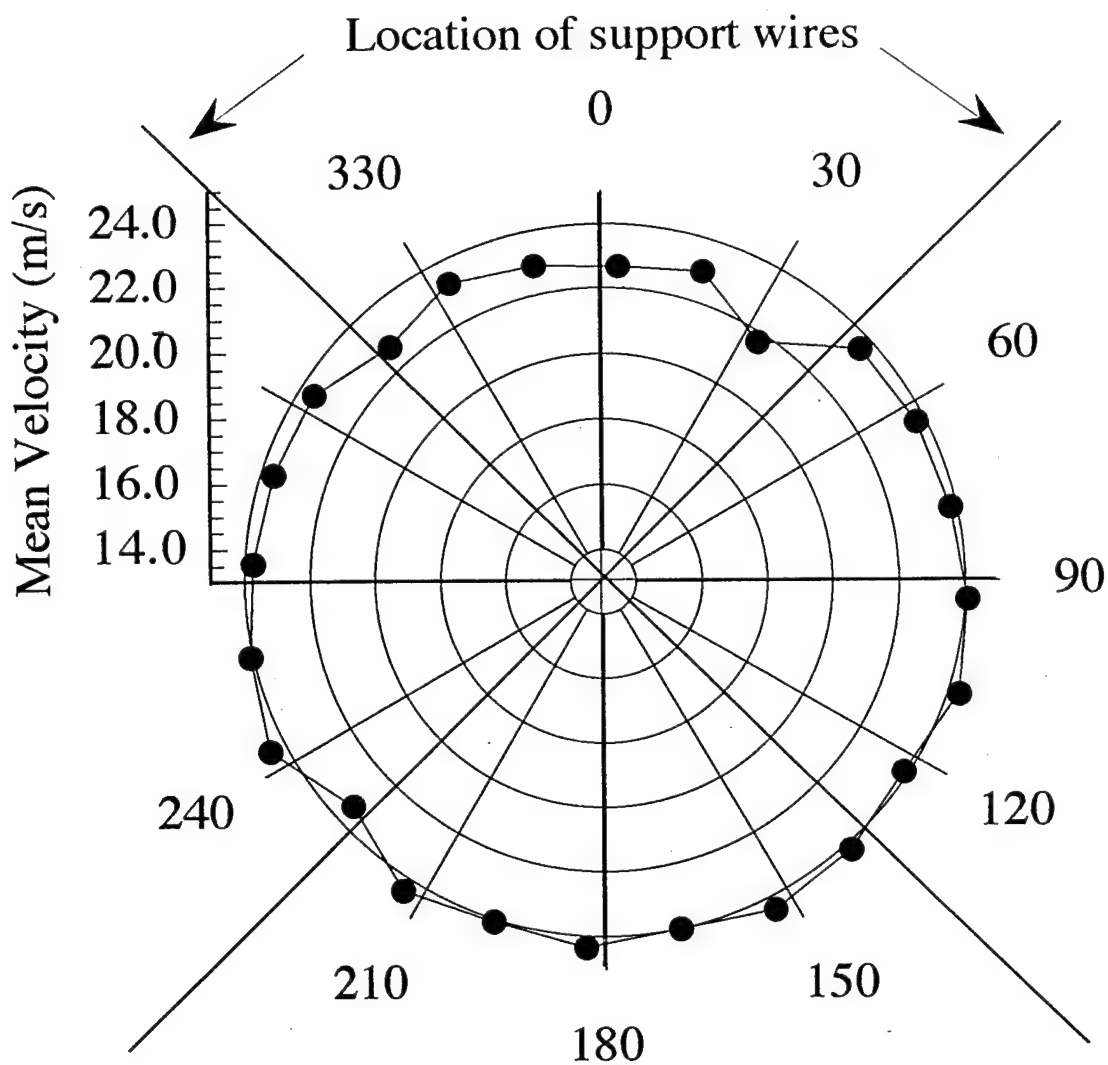


Figure 1.16. Mean Velocity Uniformity at 7 m Downstream From Contraction Exit and 3 cm from Cylinder Surface

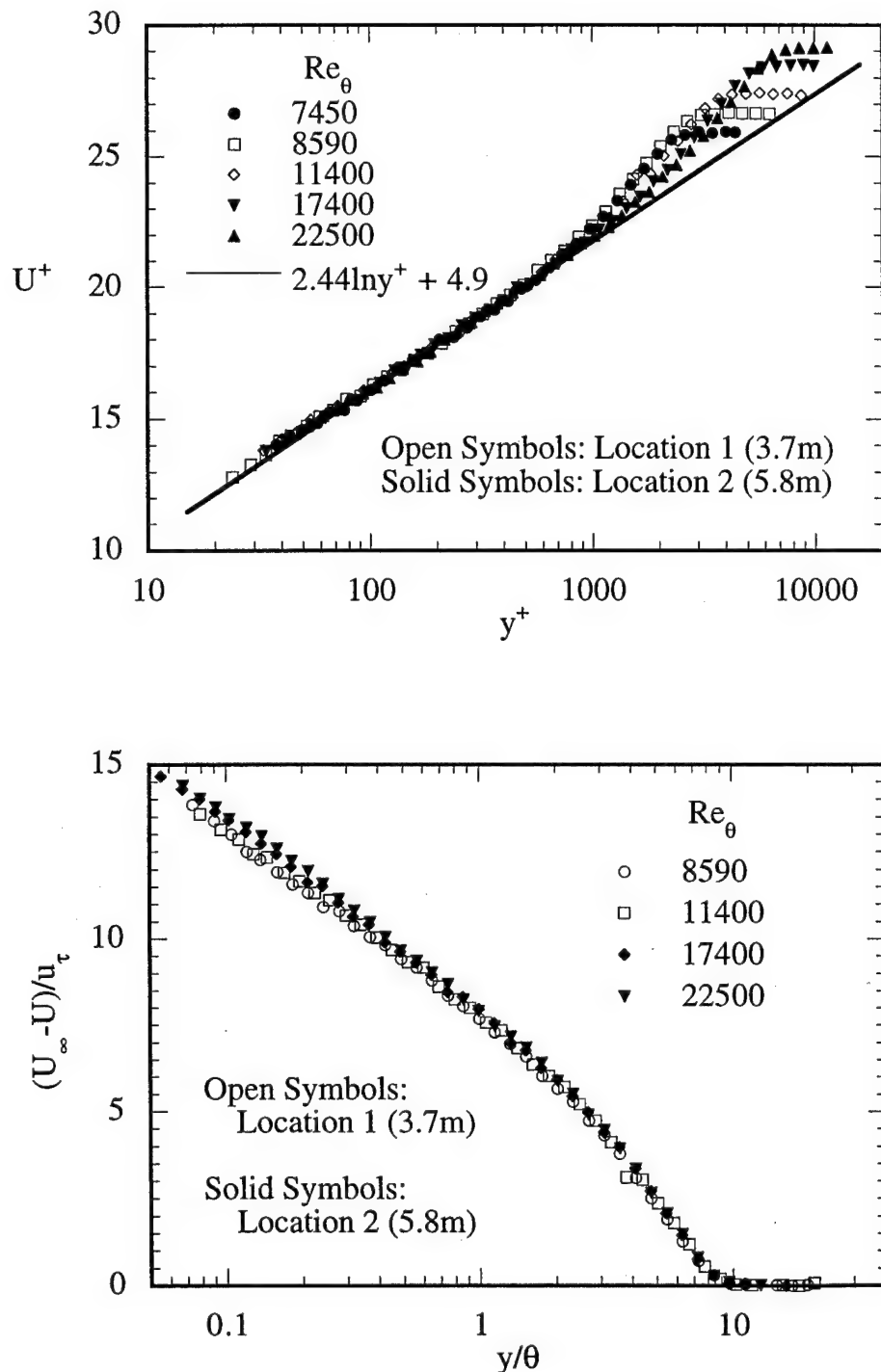


Figure 1.17. Cylinder Model Boundary Layer Wall-Scaling (top) and Outer-Scaling (bottom) of the Streamwise Mean Velocity Profiles

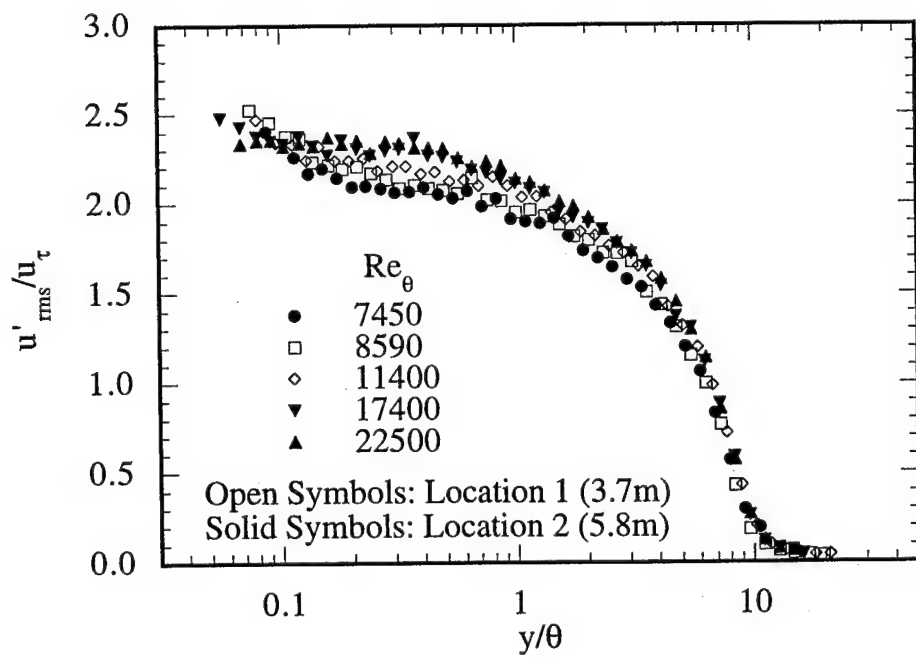
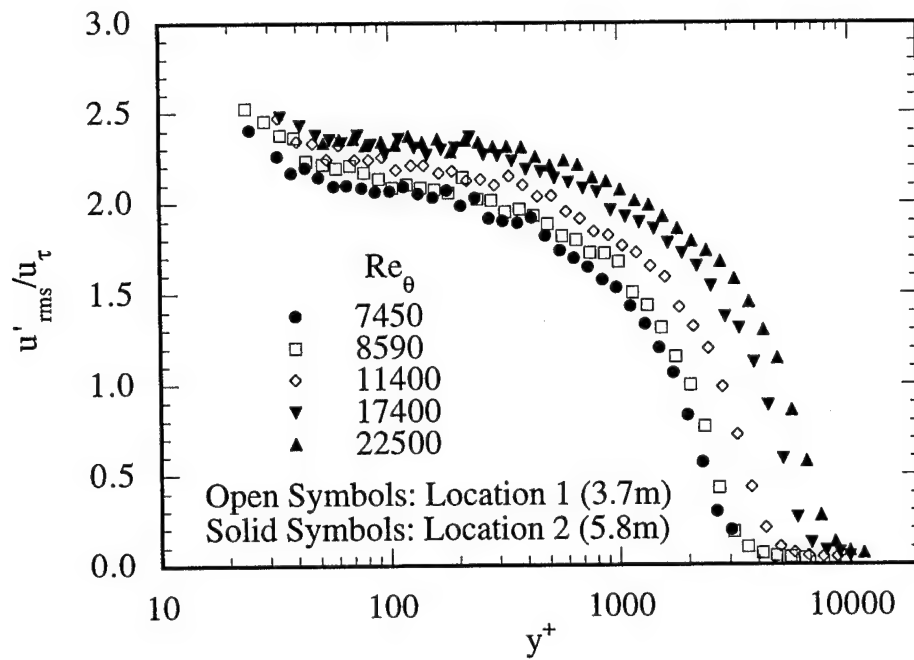


Figure 1.18. Cylinder Model Boundary Layer Wall-Scaling (top) and Outer-Scaling (bottom) of the Streamwise RMS Velocity Profiles

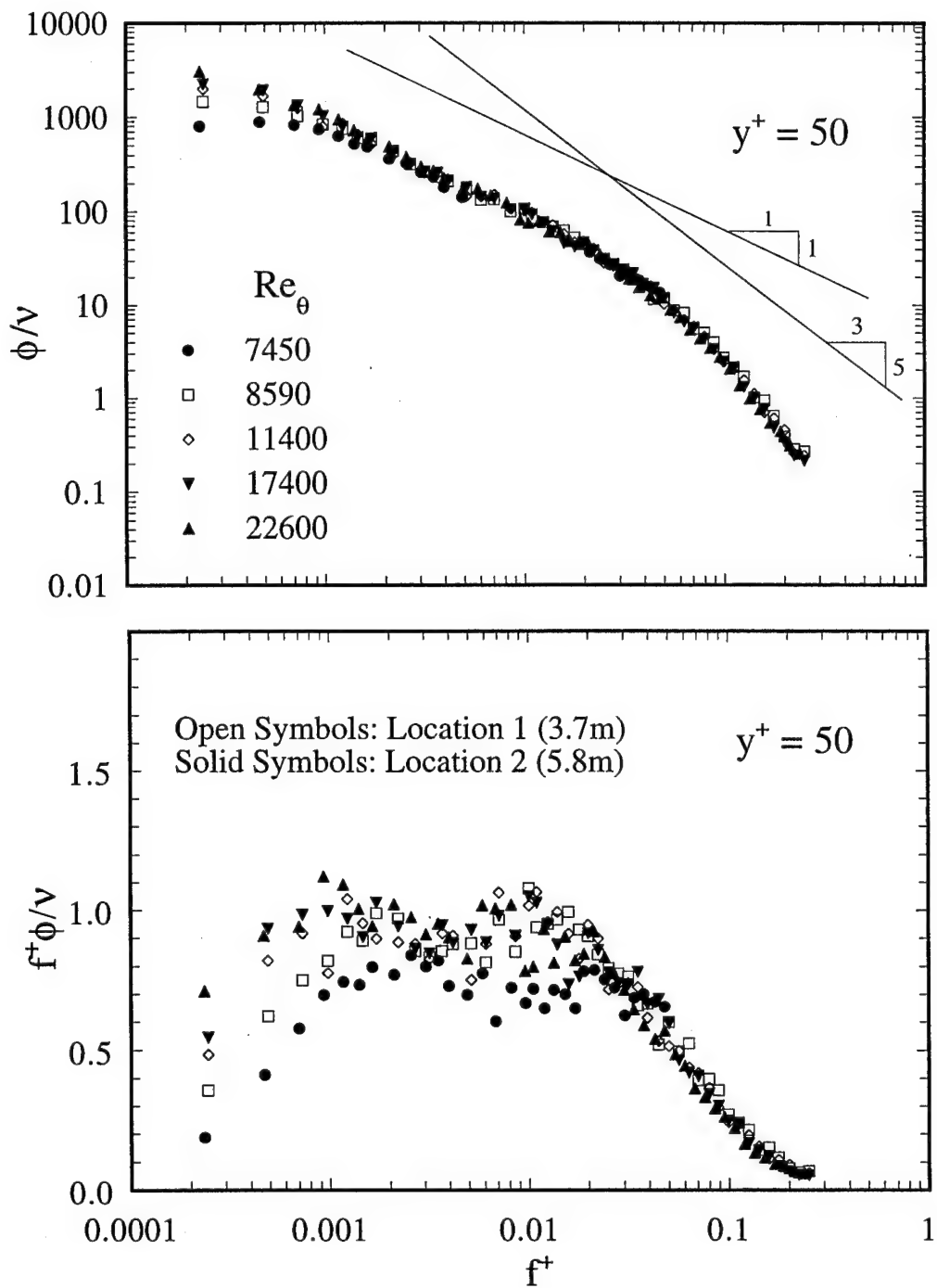


Figure 1.19. Cylinder Model Boundary Layer Wall-Scaling Characteristics of the Streamwise Velocity Spectra in the Buffer region at  $y^+=50$  Using Log-Log (top) and Semi-Log (bottom) coordinates

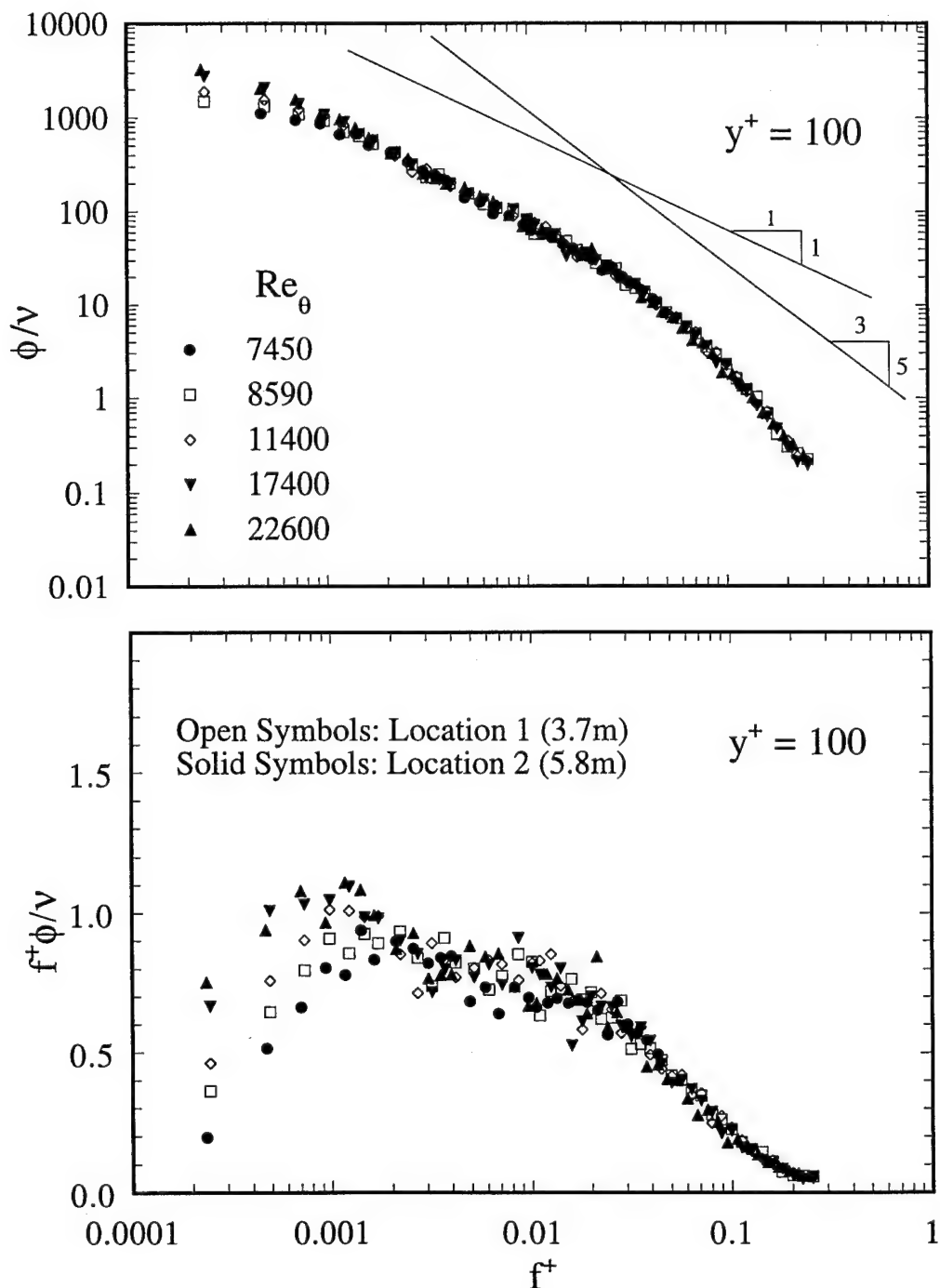


Figure 1.20. Cylinder Model Boundary Layer Wall-Scaling Characteristics of the Streamwise Velocity Spectra in the Logarithmic region at  $y^+ = 100$  Using Log-Log (top) and Semi-Log (bottom) coordinates

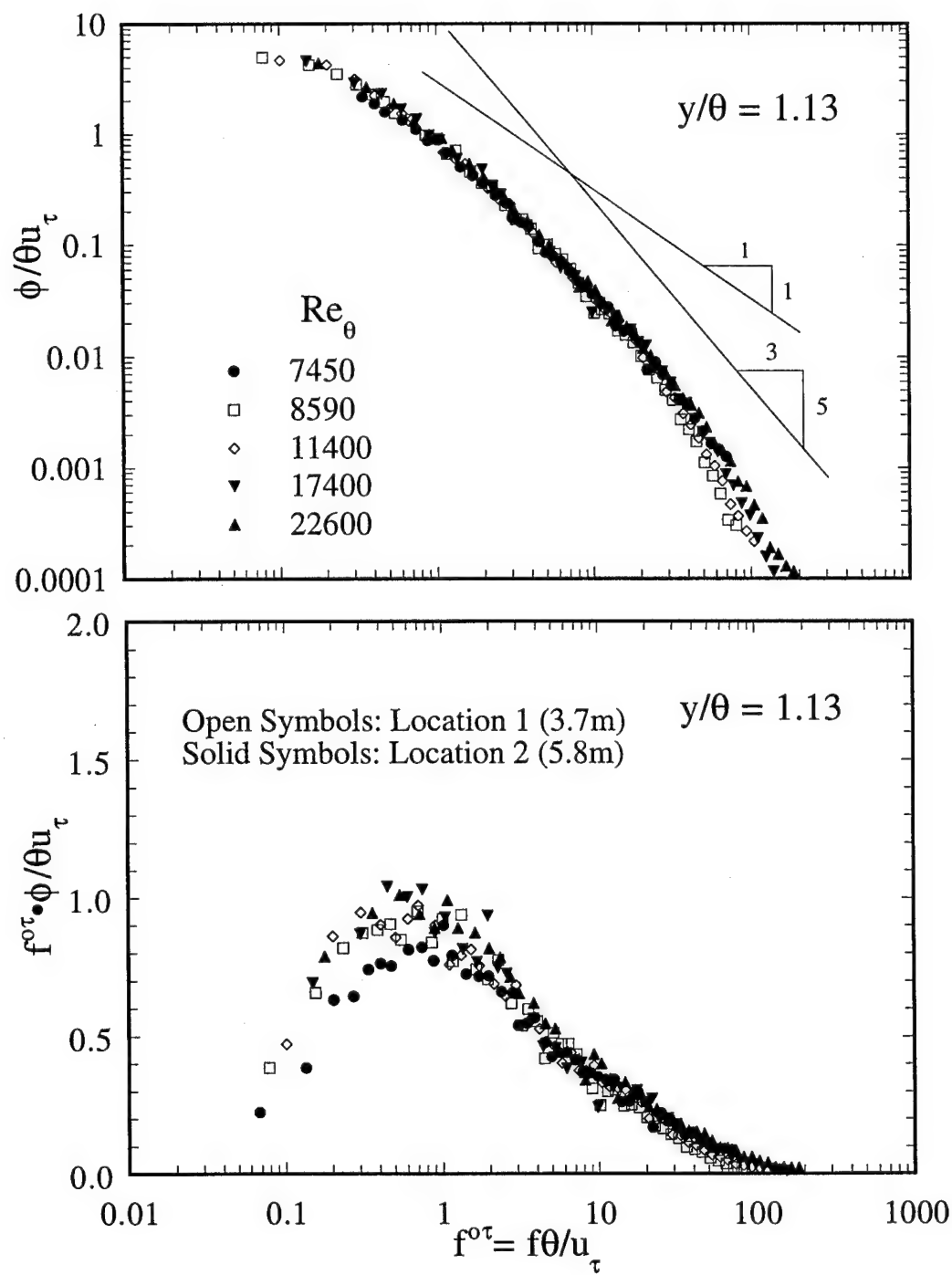


Figure 1.21. Cylinder Model Boundary Layer Outer-Scaling Characteristics of the Streamwise Velocity Spectra in the Logarithmic region at  $y/\theta=1.13$  Using Log-Log (top) and Semi-Log (bottom) coordinates

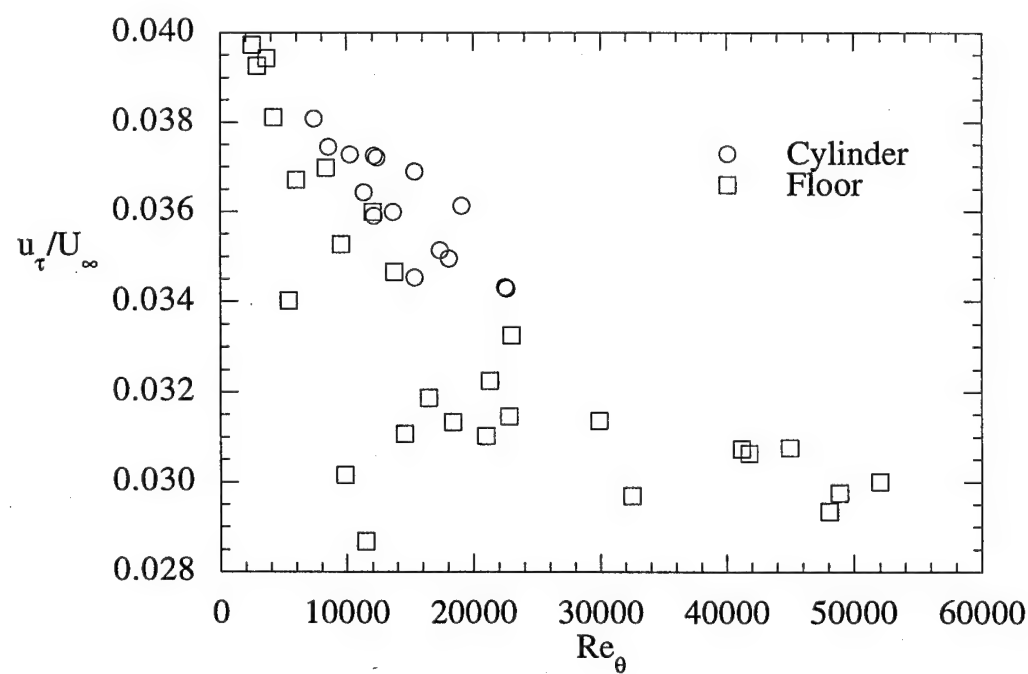
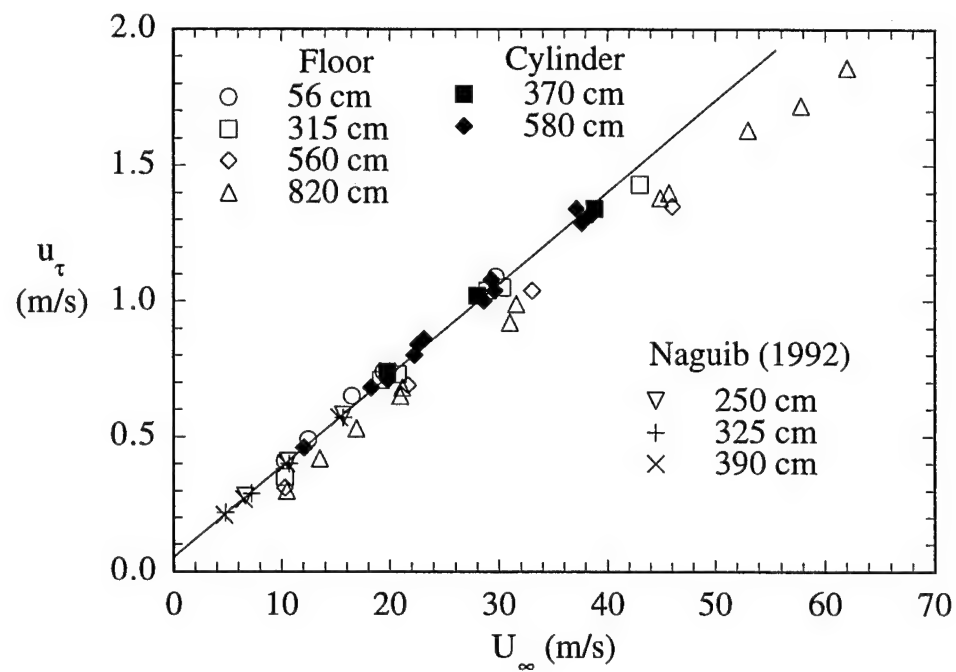


Figure 1.22. Comparison of  $Re_x$  Dependence of Friction Velocity (top) and Reynolds Number Trends in the Ratio  $u_\tau/U_\infty$  (bottom)

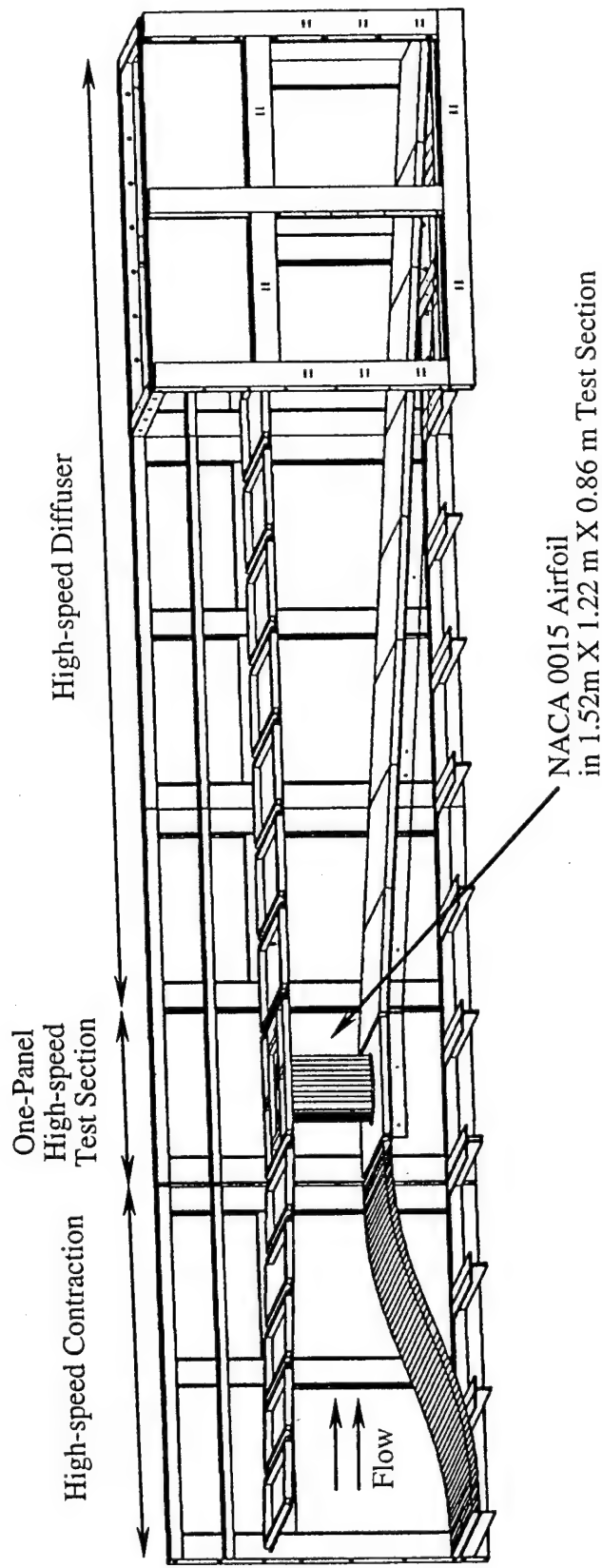


Figure 2.1. Drawing of the One-Panel High-Speed NDF Test Section Showing Modifications to the Original 1.52 m x 1.23 m x 10.4 m Test Section to Accommodate the 0.61 m Tall NACA 0015 Airfoil

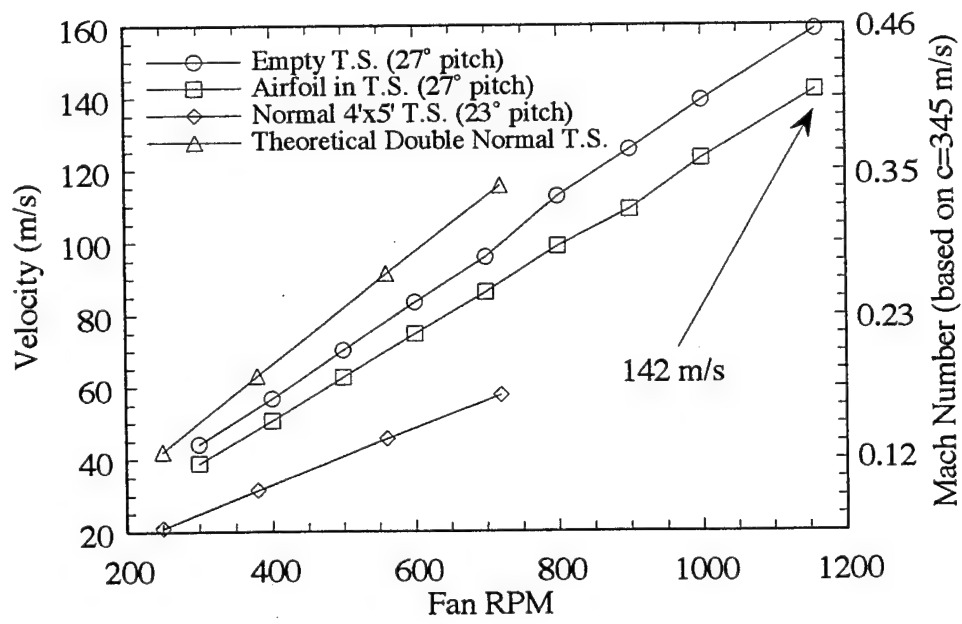
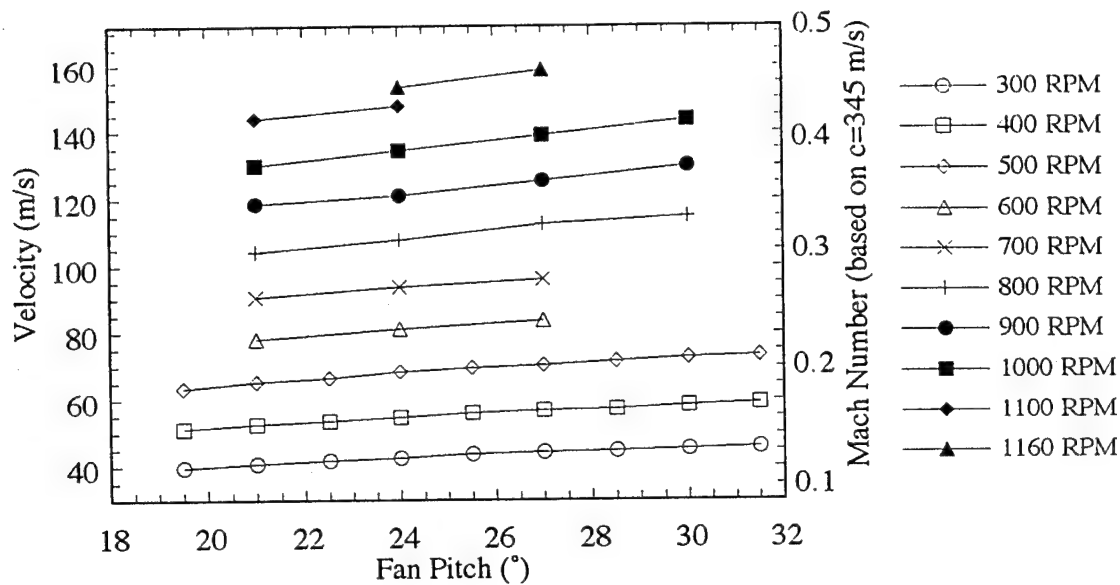


Figure 2.2. Free-Stream Velocity in the Empty One-Panel High-Speed Test Section for Various Fan Pitch Angles and Fan RPM (top) and Free-Stream Velocity in the Empty One-Panel High-Speed Test Section with and without the NACA 0015 Airfoil Installed (bottom)

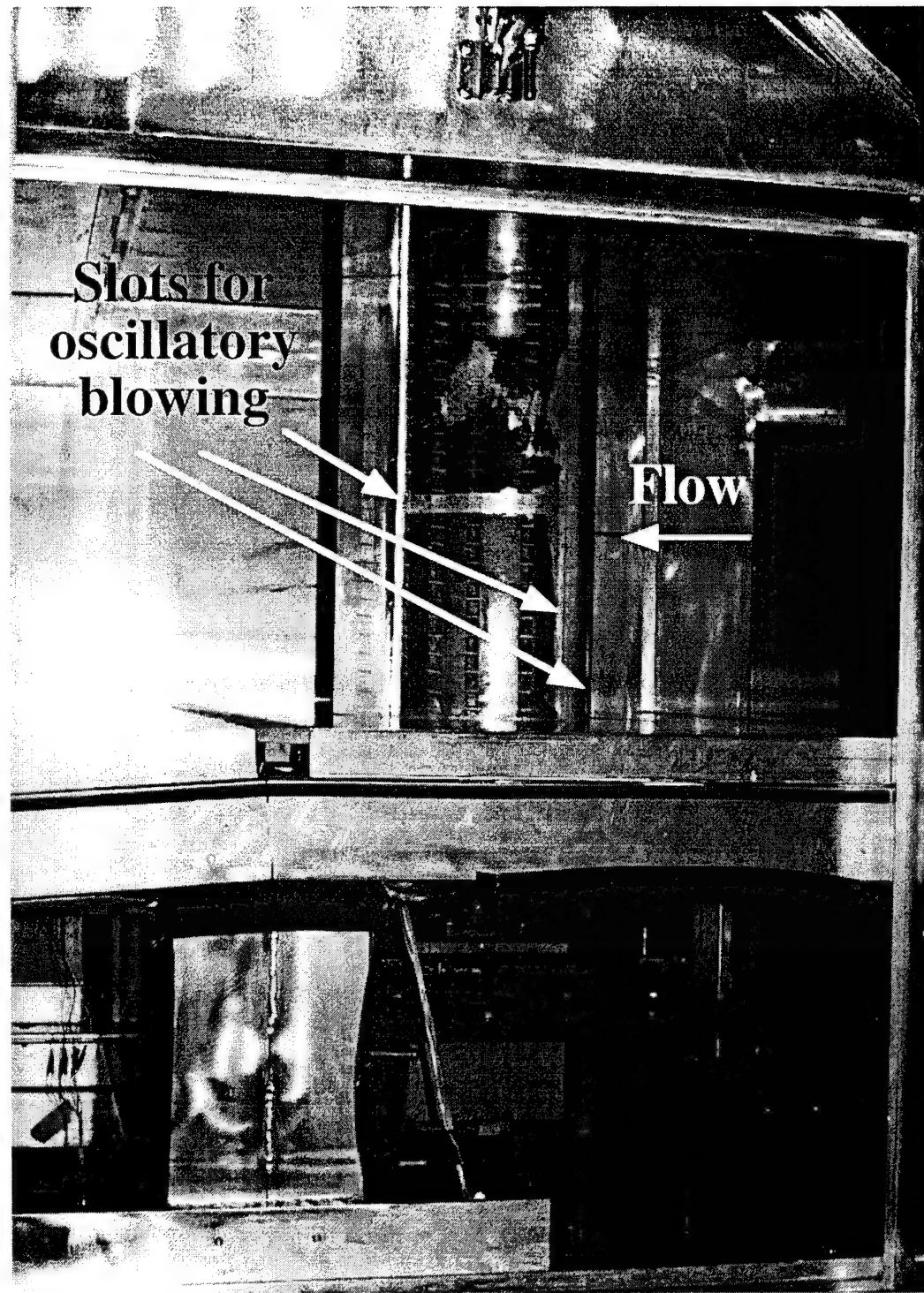


Figure 2.3. Photograph of the NACA 0015 Airfoil Mounted in the NDF High-Speed Test Section

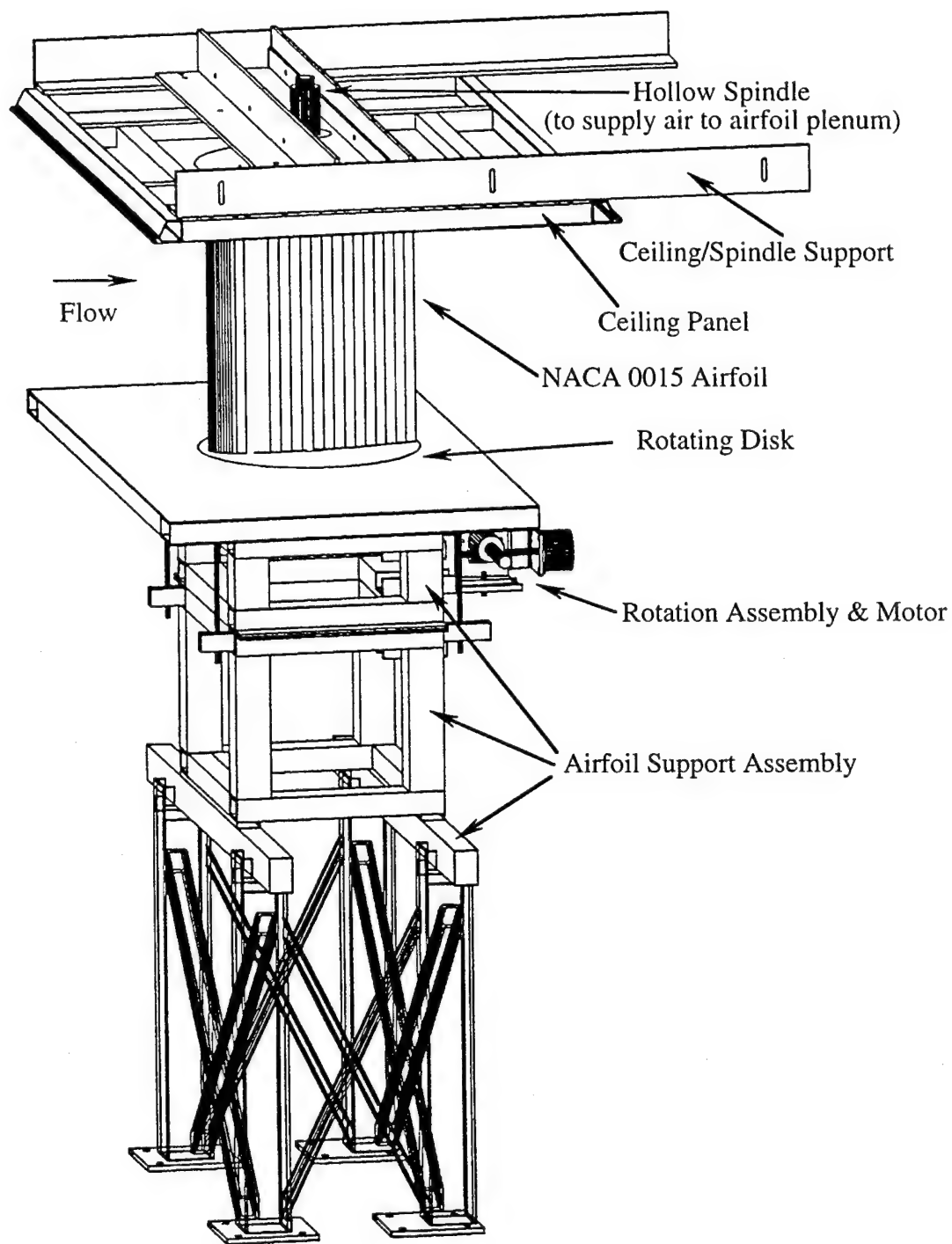


Figure 2.4. Drawing of the NACA 0015 Airfoil Mounting/Rotation Assembly

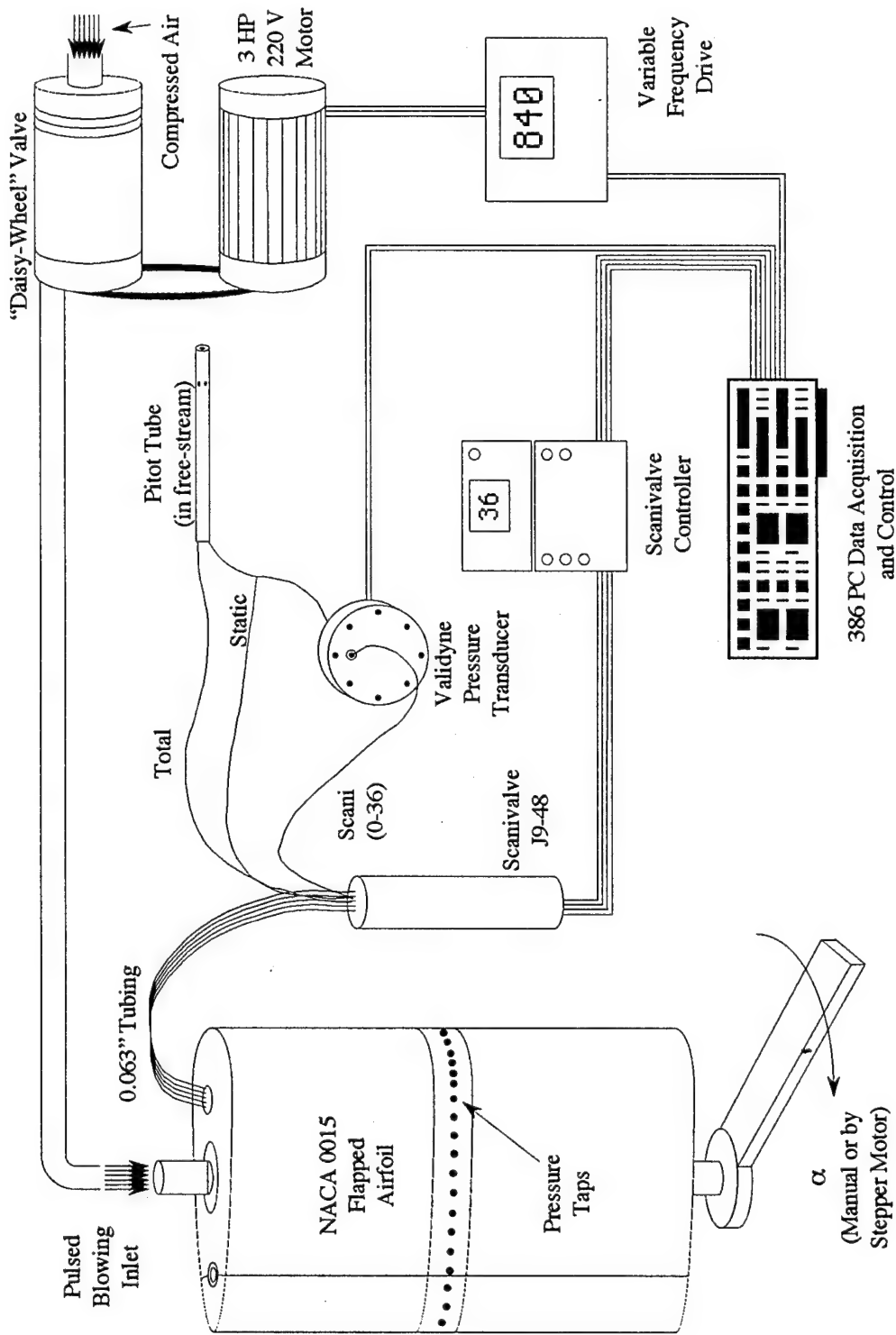


Figure 2.5. Schematic Drawing of the Oscillatory Blowing Experimental Equipment

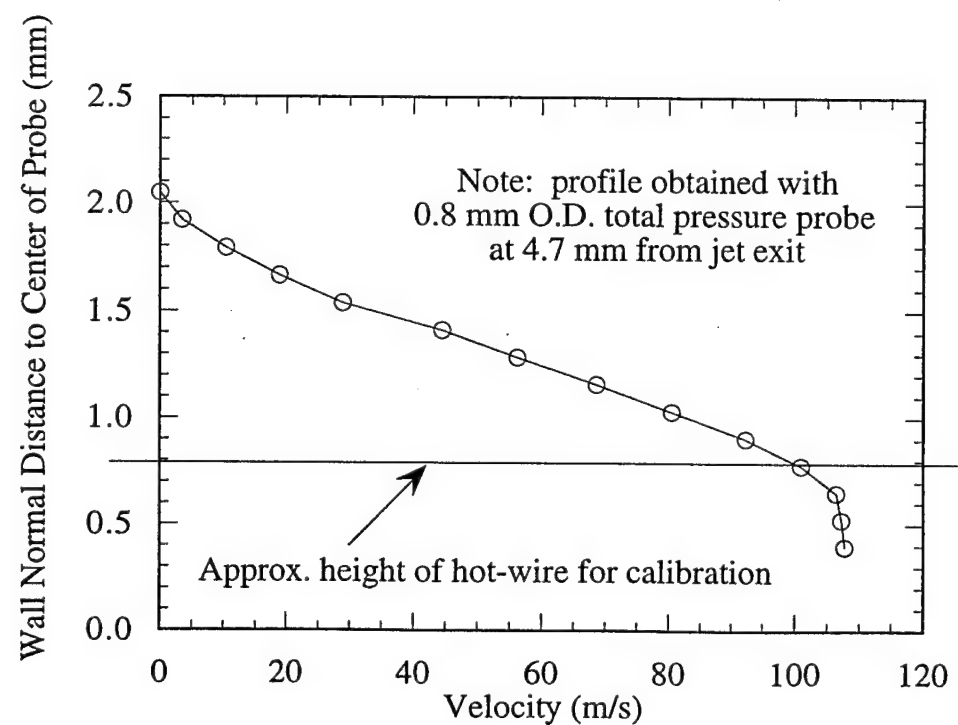
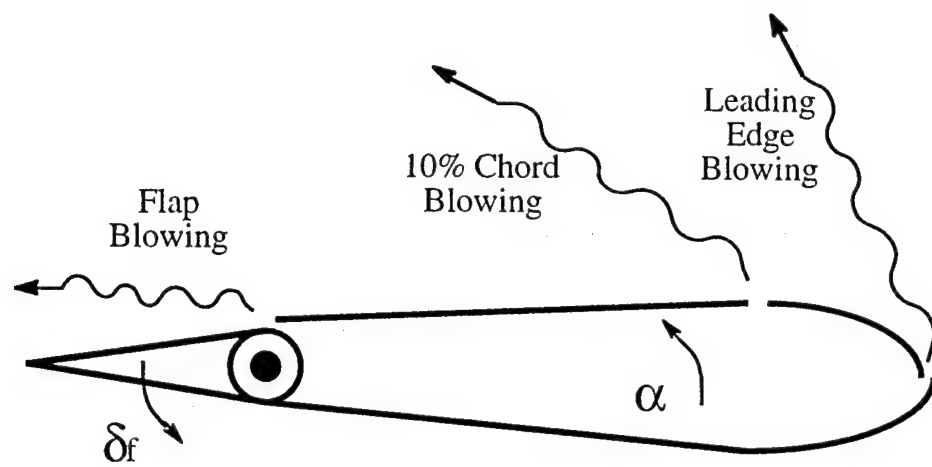


Figure 2.6. Location of the Oscillatory Wall Jets on the NACA 0015 Airfoil (top) and Velocity Profile of Leading Edge Wall Jet Showing Location of Hot-Wire Probe for RMS Amplitude Calibration (bottom)

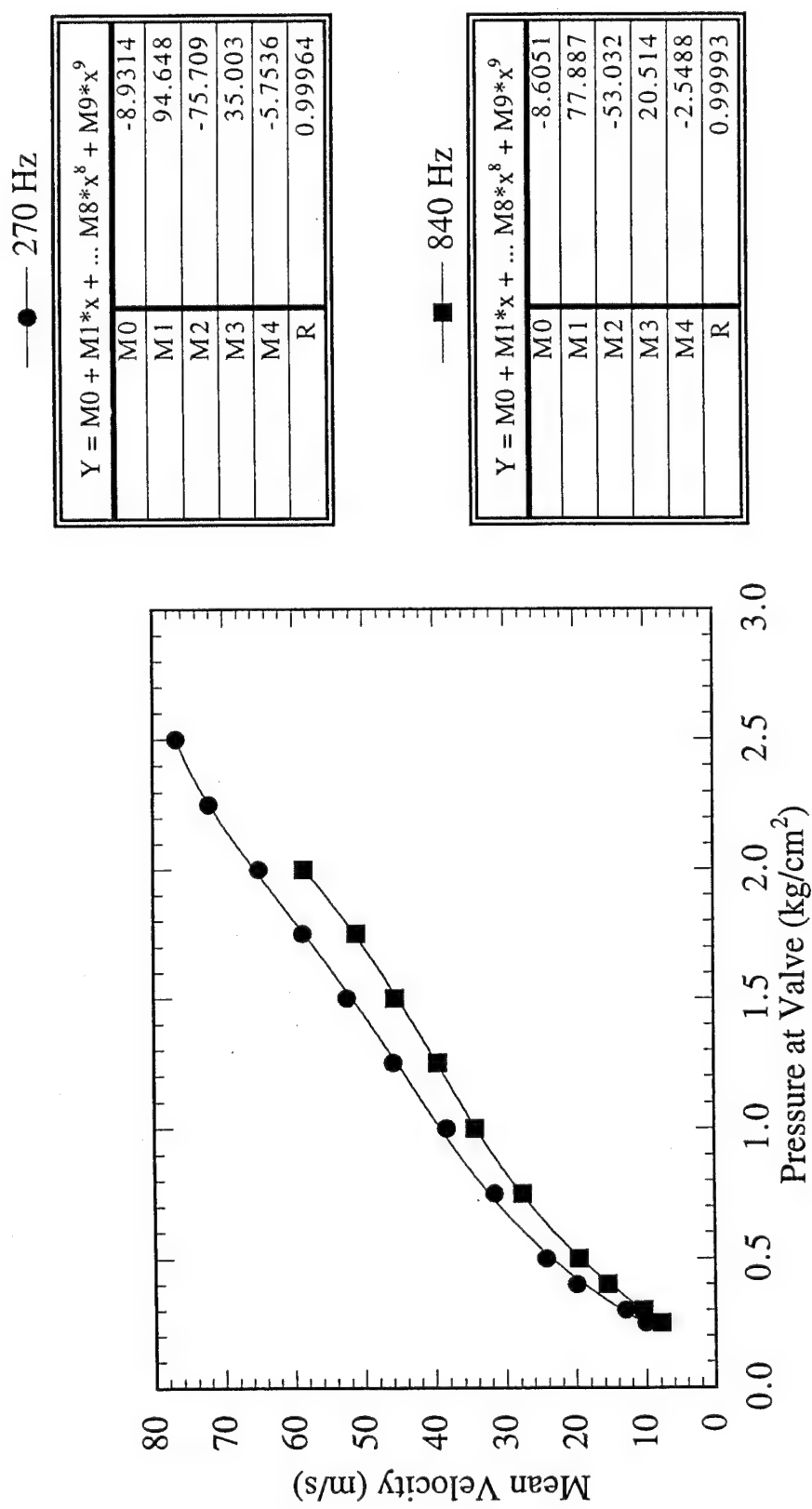


Figure 2.7. Mean Velocity Calibration of the Leading Edge Wall Jet as a Function of Gauge Pressure Read at the Inlet to the Rotating Valve for Two Different Oscillation Frequencies

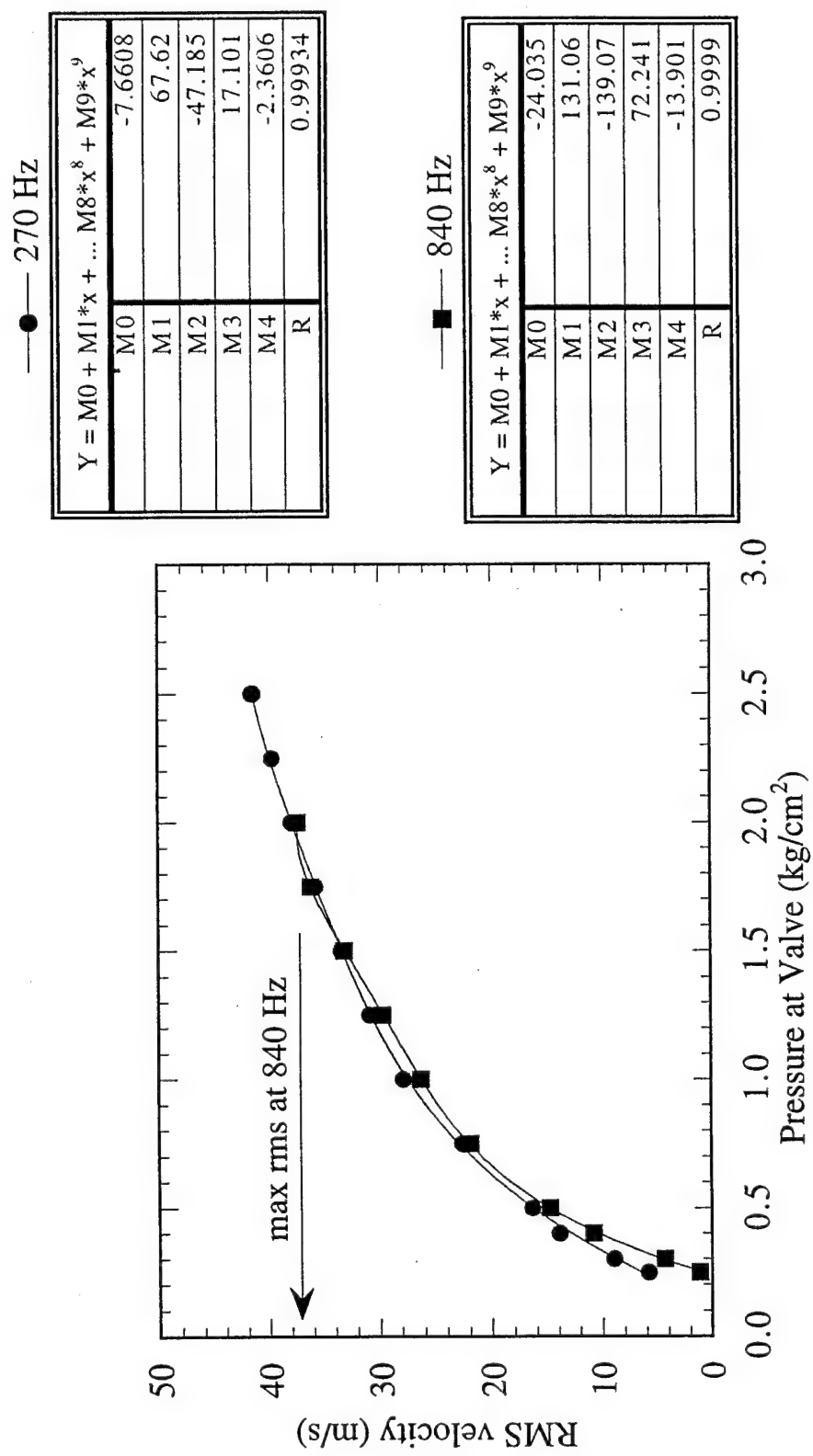


Figure 2.8. RMS Velocity Calibration of the Leading Edge Wall Jet as a Function of Gauge Pressure Read at the Inlet to the Rotating Valve for Two Different Oscillation Frequencies

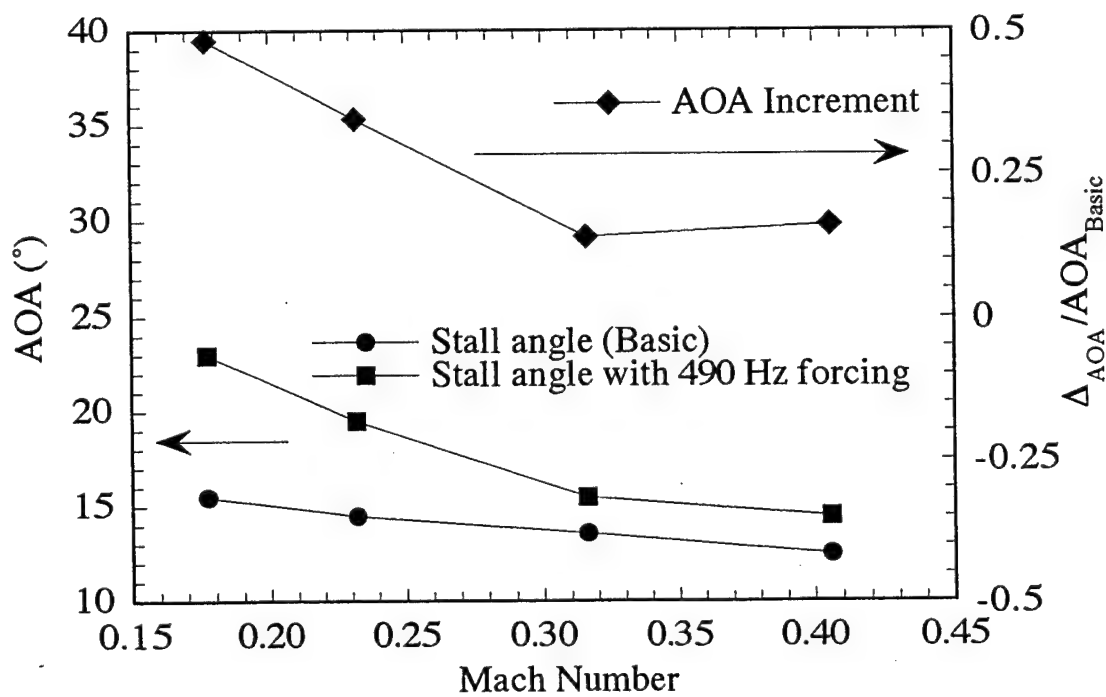
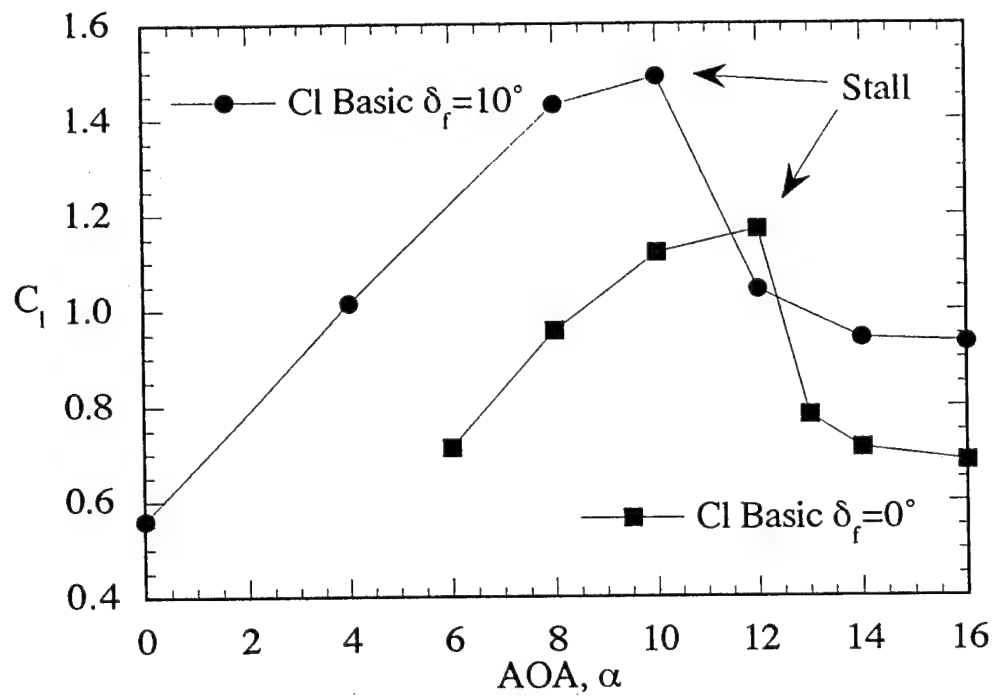


Figure 2.9. Coefficient of Lift,  $C_l$ , as a Function of Static Angle of Attack for Flap Angles of  $\delta_f = 0^\circ$  and  $10^\circ$  (top) and Improvement in Stall AOA Due to Oscillatory Blowing at  $C_\mu = (0.01; 0.01)\%$  (bottom)

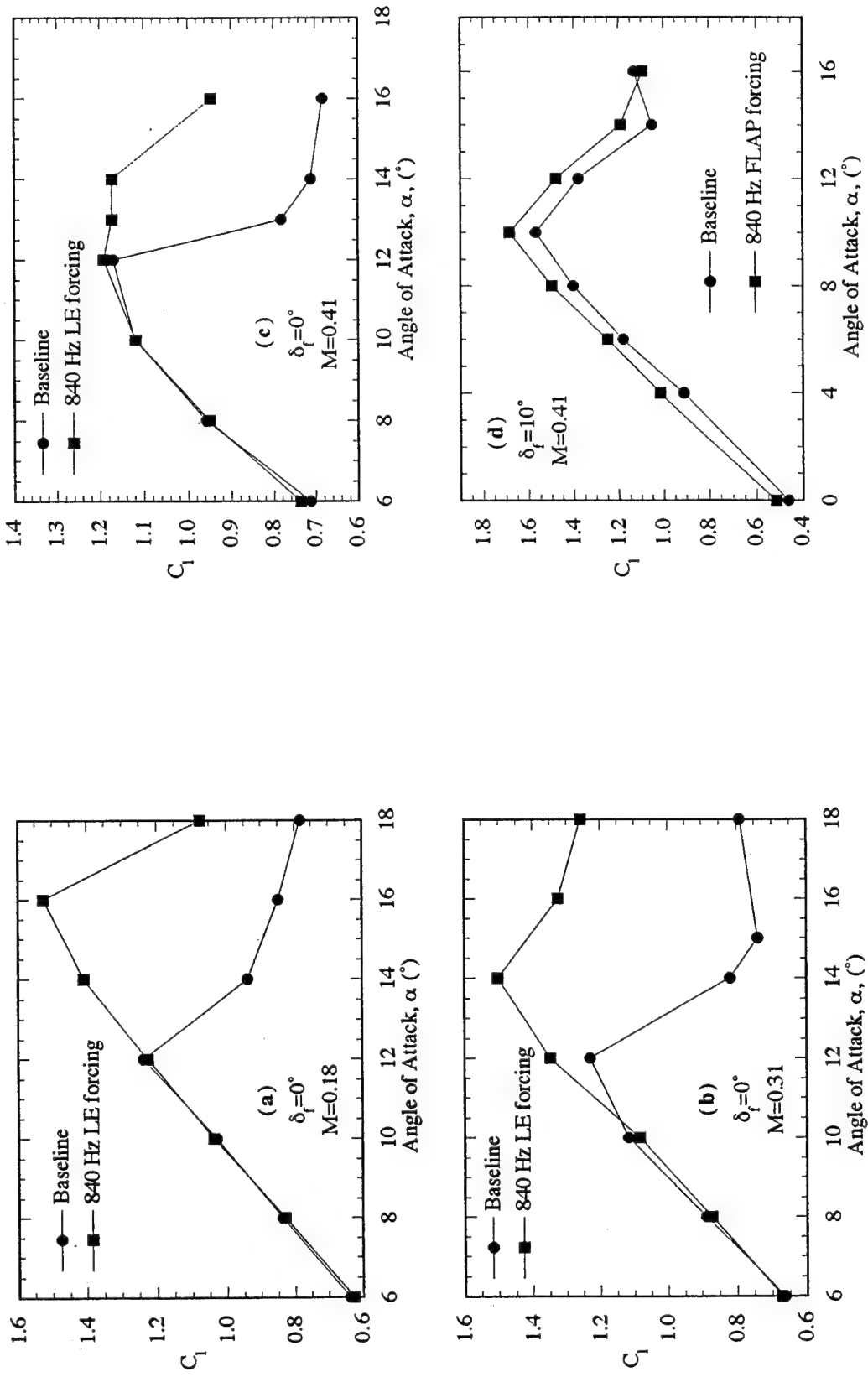


Figure 2.10. Improvement in  $C_l$  as a Function of Angle of Attack Due to 840 Hz Oscillatory Blowing at  $C_\mu=(0.02;0.02)\%$ . Parts a, b, and c:  $\Delta_f=0^\circ$  L.E. Blowing at  $M=0.18, 0.31, 0.41$ . Part d:  $\Delta_f=10^\circ$  Flap Blowing at  $M=0.41$ . L.E. Untaped for Baseline

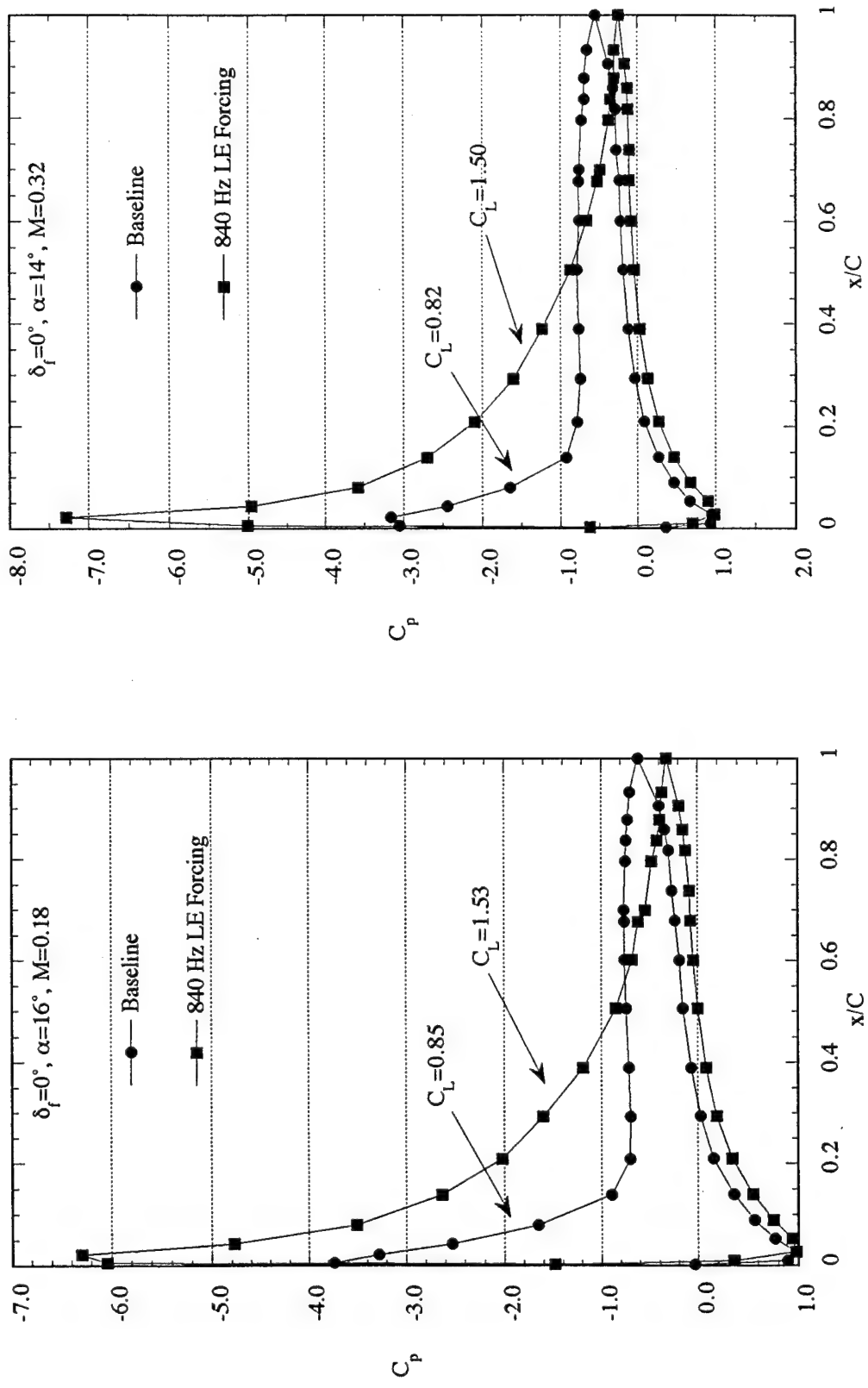


Figure 2.11. Effect of 840 Hz Oscillatory L.E. Blowing on  $C_p$  and  $C_l$  with  $C_\mu = (0.02; 0.02)\%$ . Left:  $\delta_f = 0^\circ$ ,  $\alpha = 16^\circ$ ,  $M = 0.18$ . Right:  $\delta_f = 0^\circ$ ,  $\alpha = 14^\circ$ ,  $M = 0.32$ . L.E. Untaped for Baseline

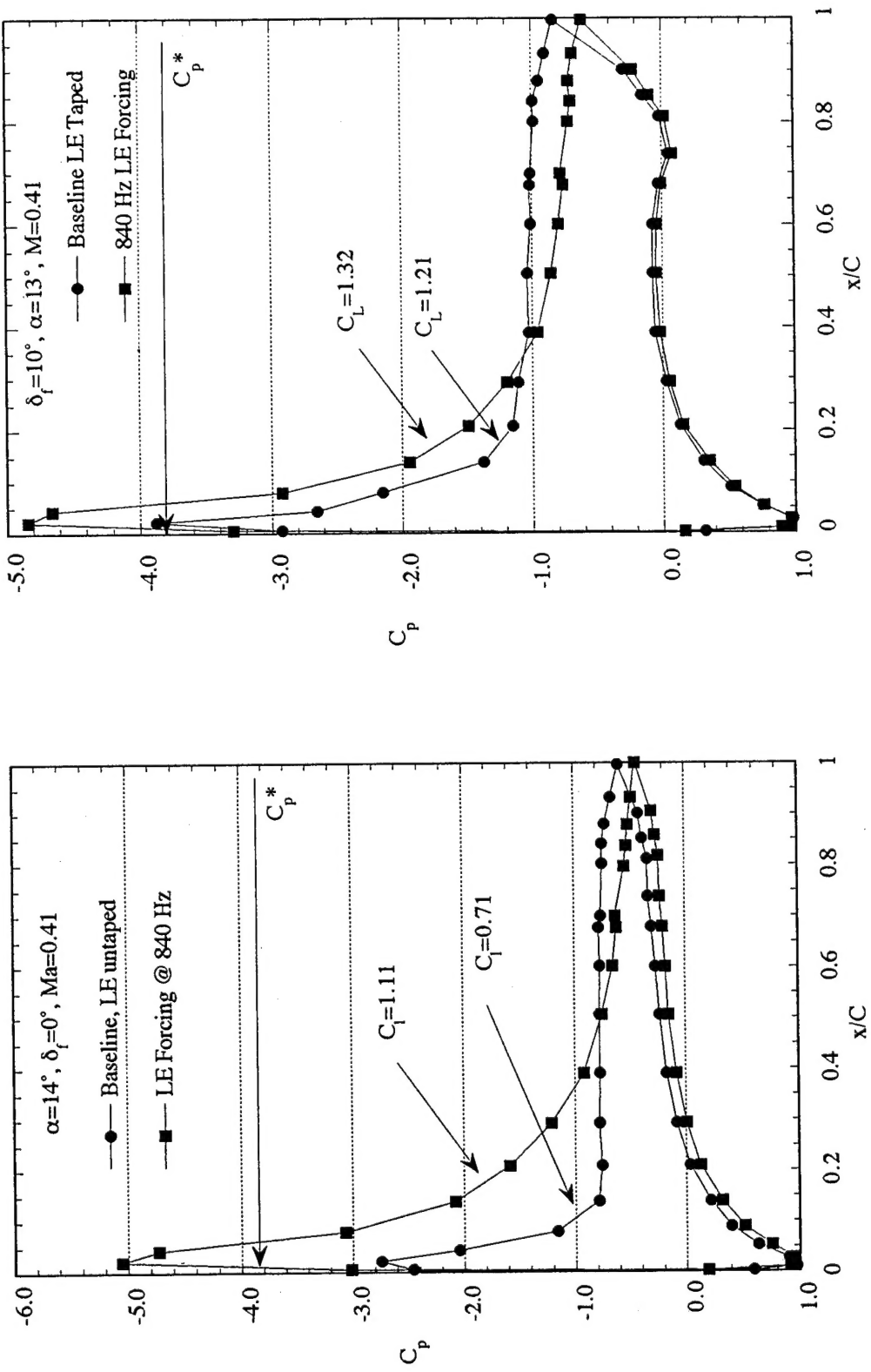


Figure 2.12. Effect of 840 Hz Oscillatory L.E. Blowing on  $C_p$  and  $C_l$  with  $C_\mu = (0.02; 0.02)\%$ . Left:  $\delta_f = 0^\circ$ ,  $\alpha = 16^\circ$ ,  $M = 0.41$ , L.E. Untaped for Baseline. Right:  $\delta_f = 10^\circ$ ,  $\alpha = 14^\circ$ ,  $M = 0.41$ , L.E. Taped for Baseline

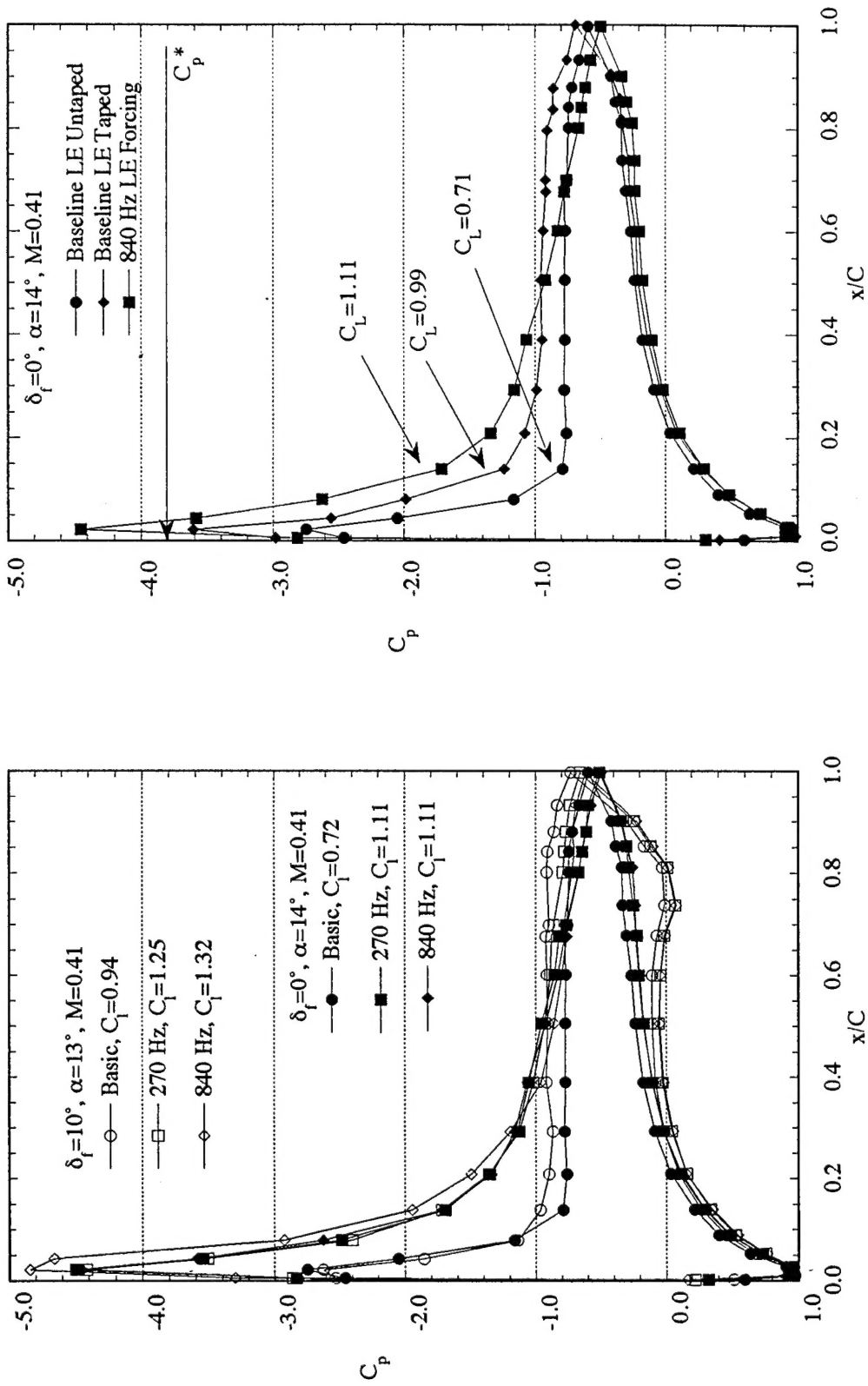


Figure 2.13. Left: Comparison of  $C_p$  with and without L.E. Blowing for 270 and 840 Hz Forcing Frequencies at  $C_u=(0.02;0.02)\%$  for both  $\delta_f=0^\circ$  and  $10^\circ$ . Right: Effect of Tape over the Leading Edge Slot on the Potential for Lift Enhancement Due to Blowing at  $\delta_f=0^\circ$ ,  $\alpha=14^\circ$ ,  $M=0.41$

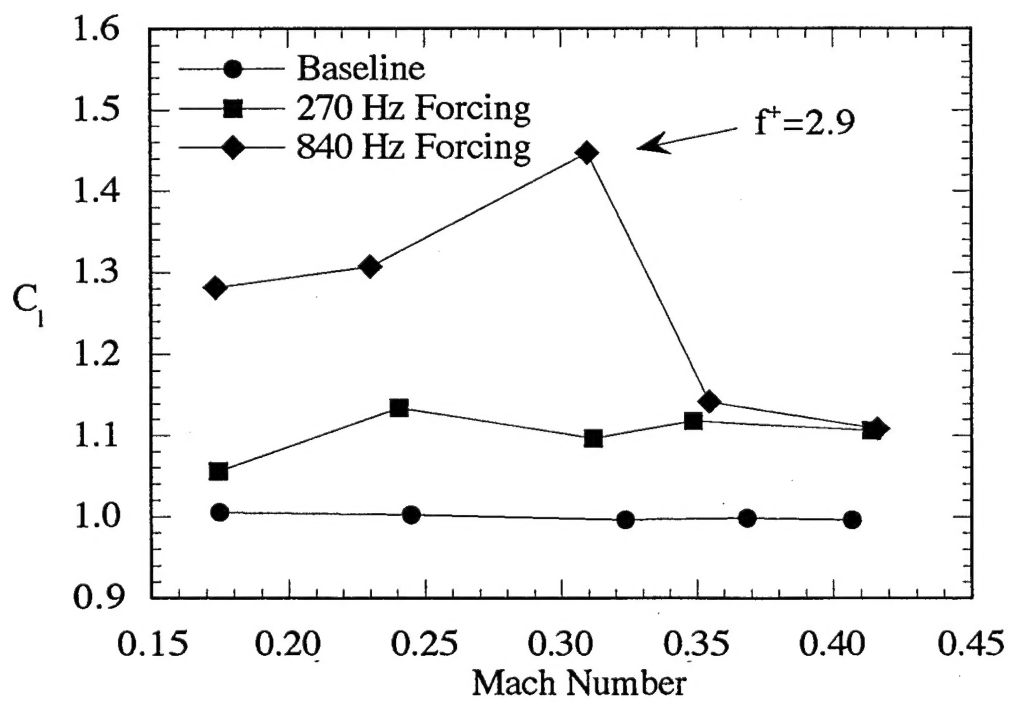
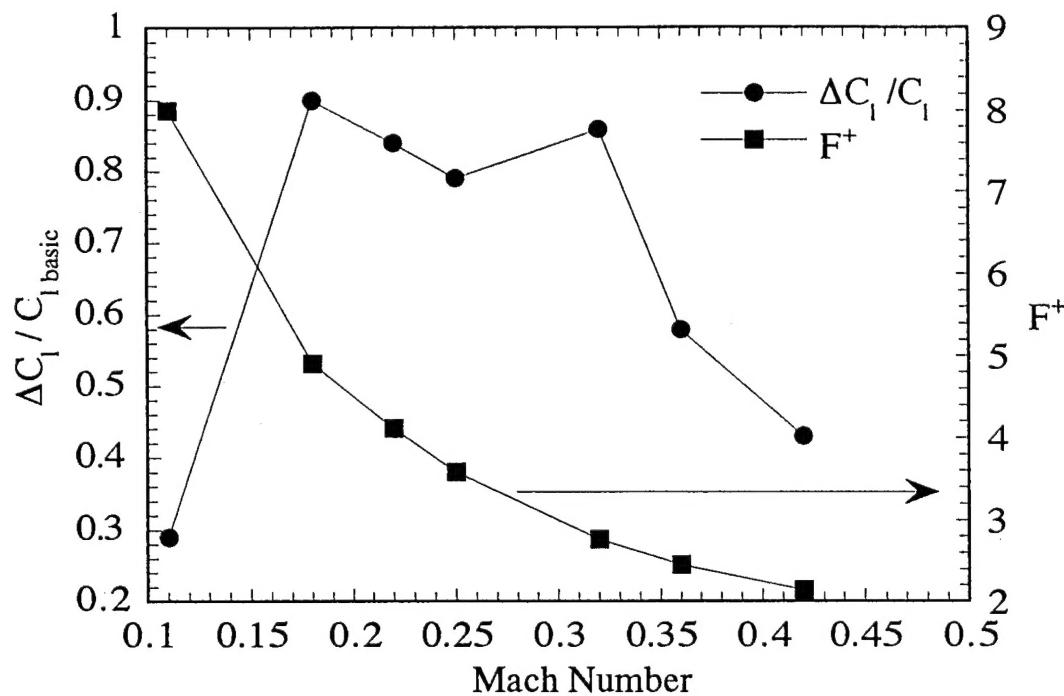


Figure 2.14.  $C_1$  Improvement and Corresponding Dimensionless Forcing Frequency Due to 840 Hz L.E. Forcing at  $\delta_r=0^\circ$ ,  $\alpha=16^\circ$ , and  $C_\mu=(0.02;0.02)\%$  (top) and  $C_1$  Improvement for 270 and 840 Hz at  $\delta_r=0^\circ$  and  $C_\mu=(0.02;0.02)\%$ . with a Constant Baseline  $C_1$  (bottom)

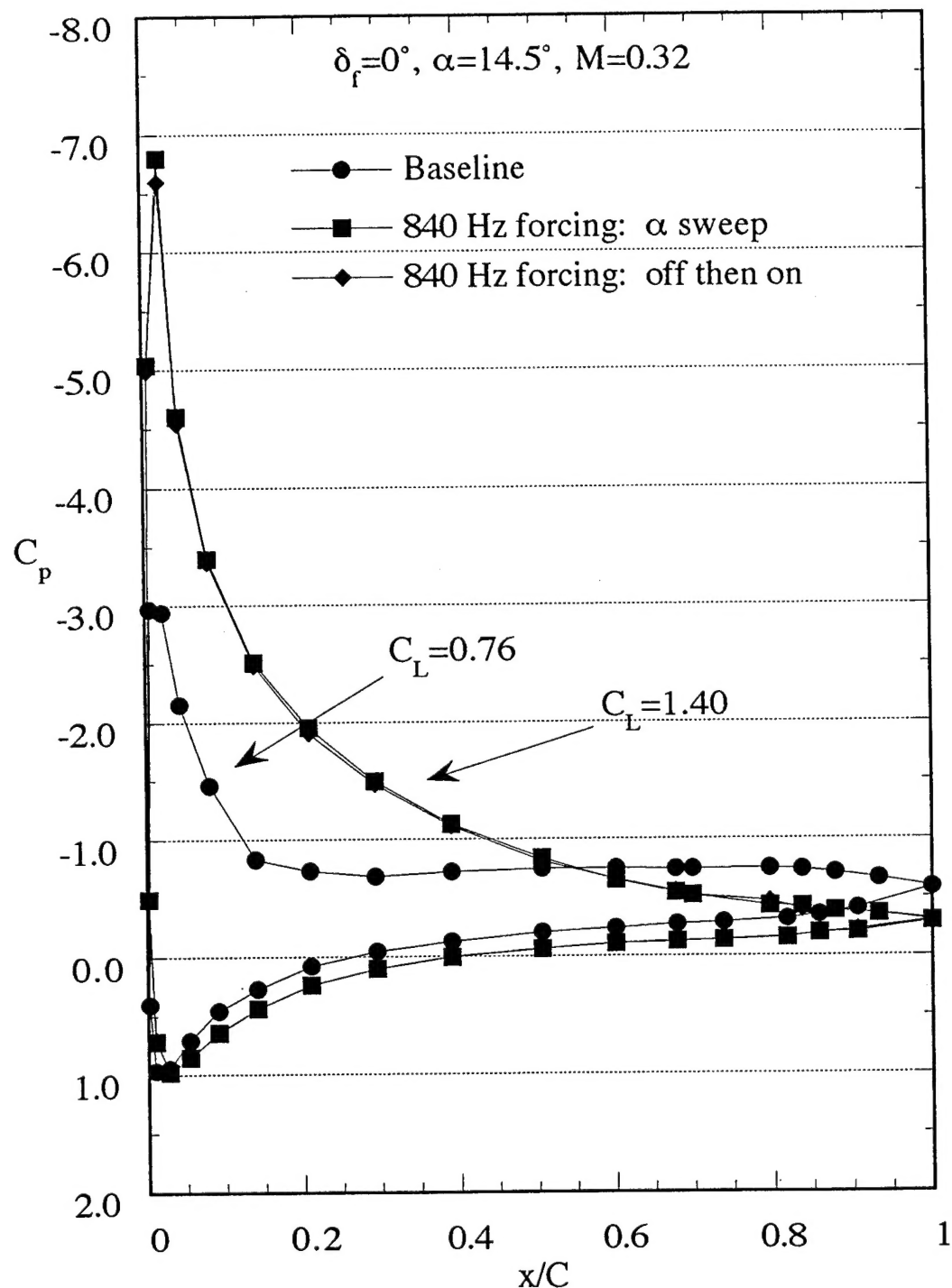


Figure 2.15. Hysteresis Effects of L.E. Oscillatory Blowing at 840 Hz for  $\delta_f=0^\circ$ ,  $\alpha=14.5^\circ$ ,  $M=0.32$ ,  $C_\mu=(0.02;0.02)\%$